2012-07-11

Under-land Convection in a PEM Fuel Cell

Hidetaka Taira
University of Miami, htaira3@gmail.com

UNIVERSITY OF MIAMI

UNDER-LAND CONVECTION IN A PEM FUEL CELL

By

Hidetaka Taira

A DISSERTATION

Submitted to the Faculty
of the University of Miami
in partial fulfillment of the requirements for
the degree of Doctor of Philosophy

Coral Gables, Florida

August 2012

UNIVERSITY OF MIAMI

A dissertation submitted in partial fulfillment of
the requirements for the degree of
Doctor of Philosophy

UNDER-LAND CONVECTION IN A PEM FUEL CELL

Hidetaka Taira

Approved:

_____ Hongtan Liu, Ph.D. Professor of Mechanical and Aerospace Engineering	_____ M. Brian Blake, Ph.D. Dean of the Graduate School
_____ Xiangyang Zhou, Ph.D. Associate Professor of mechanical and Aerospace Engineering	_____ Na Li, Ph.D. Assistant Professor of Mechanical and Aerospace Engineering
_____ Andrew Higier, Ph.D. Research Scientist Florida International University	

TAIRA HIDETAKA (Ph.D., Mechanical Engineering)
Under-land Convection in a PEM Fuel Cell (August 2012)

Abstract of a dissertation at the University of Miami.

Dissertation supervised by Professor Hongtan Liu.
No. of pages in text. (116)

When reactant gases flow in a serpentine flow field in a proton exchange membrane (PEM) fuel cell, a pressure difference occurs between the neighboring channels and it induces under-land convection (cross-flow) from the higher pressure channel to the lower one through the gas diffusion layer (GDL).

Although this cross-flow is believed to enhance fuel cell performances, up to now, no direct experiments have been conducted to measure the amount of cross-flow and its true effects on fuel cell performances. In this work, a unique experimental fixture is developed and the effective permeability and the cross-flow are measured directly in an actual fuel cell. The non-Darcy effect is also investigated and effects of the land width and the operational condition are evaluated. The cross-flow is measured with varying the valve closure and then, the cross-flowrate is obtained as a function of the pressure difference at different operational conditions. The cross-flowrate is expressed as a function of two dimensionless parameters by dimensional analysis and this correlation agrees well with the experimental data for different operational conditions and different inlet flowrates. The current density and the power density are evaluated with varying the pressure difference between the adjacent channels. It is revealed that a small increase in

the pressure difference between the adjacent channels is more efficient to enhance the current density than a large pressure increment. The net power density is introduced in order to evaluate the pumping power effect and the results show that the fuel cell performance increases significantly from the zero to low closure conditions. Finally, it is found that an additional small increase in the pressure difference can increase the net power output of a fuel cell and excessive stoichiometry decreases the net power output of a fuel cell.

A three-dimensional PEM fuel cell model is also developed and the flow fields, the oxygen distribution and the local current density distribution around the land area are studied. The results show that the cross-flow gradually decreases along the channel direction and it exists mainly under the land area. The oxygen concentration in the channel is affected by the secondary flow which is induced by the U-bend if the channel length is short. The modeling results also show that the cross-flow has a significant effect on the local current density distribution under the land area: the local current density under the land area decreases along the channel and the difference between the upstream and the downstream increases with the decrease of the cell voltage.

To Saori and Momone

ACKNOWLEDGMENT

First of all, I want to say that I really appreciate my advisor and Ph.D. committee chairperson, Dr. Hongtan Liu. When I asked him if I could study under his mentorship, he kindly accepted me as his Ph.D. student without any hesitation. He taught me about not only the necessary attitude researchers must have about their scientific inquiries, but also the necessity of pursuing the fundamental understanding behind the physical phenomena. He pushed me to advance further investigation of my subject matter; I could not have accomplished my Ph.D. work without his advice. In addition, he always supported me in both academic and family affairs and it was very helpful for my family.

I also would like to thank all of my Ph.D. committee members, Dr. Xiangyang Zhou, Dr. Na Li and Dr. Andrew Higier for evaluating my Ph.D. work and providing valuable suggestions. I realized the necessity of deepening my academic knowledge more because of their inputs.

I thank the Department of Mechanical and Aerospace Engineering of the University of Miami for their support.

I thank the Ministry of Defense of Japan for giving permission of overseas study for three years and the financial support during that time. I will utilize the knowledge that I obtained during the Ph.D. study for my research jobs there.

I thank my great colleagues, Mr. Saif Matar, Mr. Shan Jia and Mr. Son Luo. The discussion with them was very helpful in advancing my work. In addition, we had many good conversations about academic and non-academic topics.

Finally, I would like to thank all of my family who have supported me during my three years stay here, especially, my wife, Saori and my daughter, Momone. They cheered me up when I came back from the school and without their dedication and cute smiles, none of this work would have been accomplished.

TABLE OF CONTENTS

Page

LIST OF FIGURES

LIST OF TABLES

LIST OF NOMENCLATURE

ai_o^{ref}	reference exchange current density times area at cathode (A m^{-3})
c	mole concentration (mol m^{-3})
D	channel depth (m)
D_{eff}	effective diffusivity (m^2 s^{-1})
E_o	open circuit potential (V)
F	Faraday constant (96,487 C mol^{-1})
j	current density (A m^{-2})
k_p	permeability of the porous material (m^2)
L	channel length (m)
p	pressure (pa)
Q	flow rate (m^3 s^{-1})
$r^{(2)}$	coefficient in the momentum equation
R	universal gas constant (8,314 J mol^{-1} K^{-1})
T	temperature (K)
$\boldsymbol{V}$	velocity vector (m s^{-1})
W	channel width (m)
X_{O_2}	oxygen mole fraction
x	x direction coordinate (m)
y	y direction coordinate (m)
z	Z direction coordinate (m)

Greek symbols

α_a	anodic transfer coefficient
α_c	cathodic transfer coefficient
δ	GDL thickness (m)
ε	porosity
Φ	potential (V)
η	overpotential (V)

μ	viscosity (Pa s)
ρ	density (kg m^{-3})
σ	ionic conductivity, electrical conductivity (S m^{-1})

Subscripts and Superscripts

cross	cross-flow
in	inlet flow
m	membrane
ref	reference
s	Solid

CHAPTER 1

INTRODUCTION

1.1 An introduction to fuel cells

Since there has been a great increase in world population, our energy consumption is expected to keep increasing in the future as shown in Fig. 1.1. In addition, Fig. 1.2 indicates that a large part of the primary energy sources depends on oil and coal although the use of alternative energy sources will increase in the future; thus, it can be said that our daily energy consumption continues to rely on the use of fossil fuels. However, since the combustion of these fossil fuels causes severe air pollution and green gas effects to our environment, there has been an urgent need to develop environmentally friendly energy sources for a sustainable society.

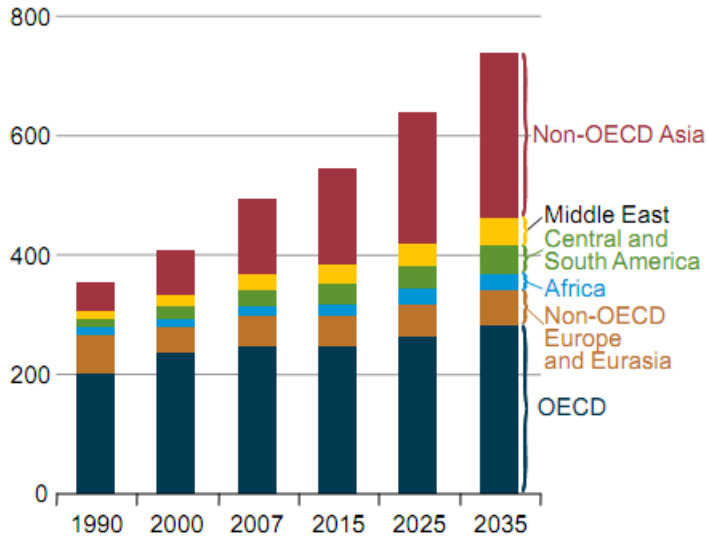

Fig. 1.1 World energy consumption by region, 1990-2035 (quadrillion Btu per year) (U.S. Energy Information Administration 2011)

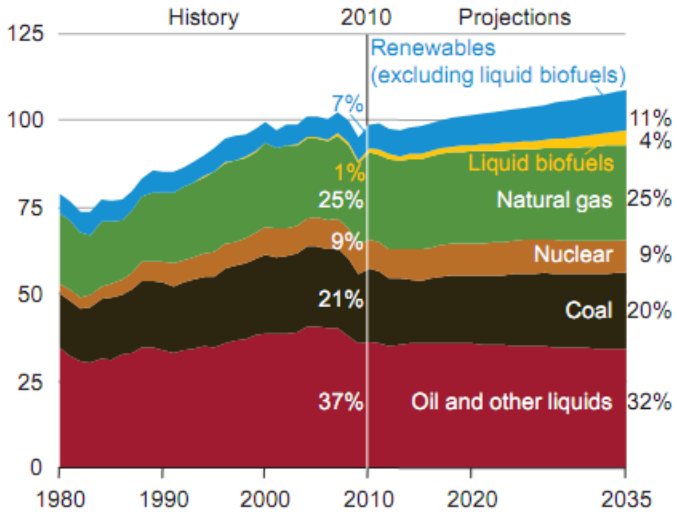

Fig. 1.2 U.S. primary energy consumption by fuel, 1980-2035 (quadrillion Btu per year) (U.S. Energy Information Administration 2012)

A large number of renewable energy technologies have been studied and developed. These alternative energy includes solar, wind, hydroelectric power, bioenergy, geothermal energy and many other sources (Spiegel 2007). Although each energy source has its advantage and disadvantage, most of these sources cannot be used directly for transport or portable applications for our daily life. Generally, electrical energy can be obtained from batteries, internal combustion (IC) engines with electrical generators and fuel cells for these purposes. Fig. 1.3(a) schematically shows how to generate electricity from these devices. Fuel cells and batteries can directly produce electricity from chemical energy. However, IC engines have to convert chemical energy into heat energy at first. Then, heat energy is transformed into mechanical energy and finally mechanical energy is converted into electricity. Thus, the theoretical efficiency of batteries and fuel cells is higher than that of IC engines. Fig. 1.3(b) shows the relationship between the power and the capacity for these energy sources. Since batteries usually work as the storage and the source of energy, their power and capacity are interconnected with each other. For fuel

cells and IC engines, however, their power is related to their own size and the capacity is determined by the fuel tank size; thus, the flexibility of fuel cells and IC engines is higher than that of batteries.

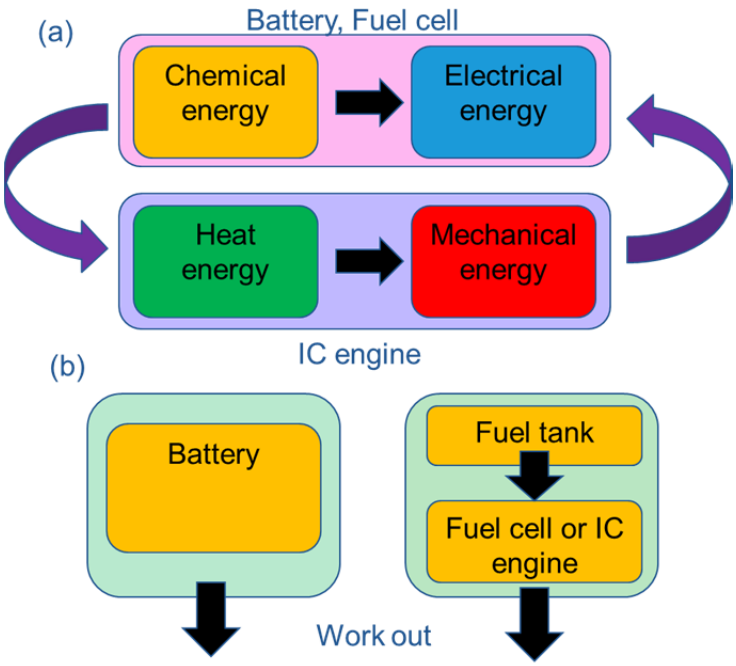

Fig. 1.3 Schematic comparison of fuel cell, battery and internal combustion engine (O'Hayre et al 2009)

Although fuel cells are one of the historically old energy technologies, there is an advantage of low or zero emission performance for them; thus, fuel cells are regarded as one of the most promising energy devices for the future. The first fuel cell prototype was developed and demonstrated more than 150 years ago by William Grove in 1839. As shown in Fig. 1.4, he submerged platinum electrodes in the electrolyte solution and water was being electrolyzed into hydrogen and oxygen by passing an electric current through it. Then, the power supply was replaced with an ammeter and a small electric current was observed. In this experiment, it is shown that the electrolysis is being reversed and the

current is generated due to the recombination of hydrogen and oxygen (Larminie and Dicks 2003).

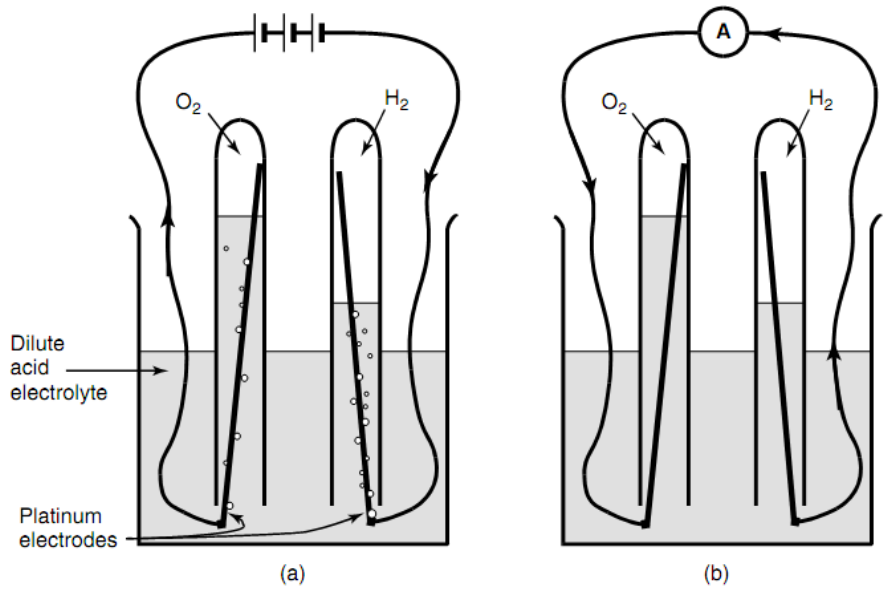

Fig. 1.4 First fuel cell demonstration by William Grove (Larminie and Dicks 2003)

1.2 Advantages and disadvantages of fuel cells

Since fuel cells directly generate electricity from chemical energy, they are more efficient than IC engines. Another remarkable point is that the power and the capacity of fuel cells are independent of each other and large systems can be as efficient as small ones whereas the performance of batteries is scale-dependent (O'Hayre et al 2009). This is very important in a case that large power systems are required. In addition, since components of fuel cells are simple and basically no moving parts exist inside the fuel cells, they are highly reliable and quiet systems. Furthermore, the by-product of a hydrogen fuel cell is only water and unfavorable emissions such as NO_x, and SO_x are

essentially zero. This is a significant advantage when fuel cells are used in transport purposes such as cars, because the reduction of these undesirable emissions is a strong demand. Although fuel cells have aforementioned advantages, there are some disadvantages and the most significant drawback is the cost. Since the current costs for automotive IC engines are about \$25 – \$35 kW^{-1} according to the U.S. Department of Energy (DOE) report, DOE is trying to reduce the cost of fuel cell systems for the transport application to \$30 kW^{-1} in order to be competitive with conventional technologies (U.S. Department of Energy 2011). Fig. 1.5 shows the FY 2011 Fuel cell R&D progress of the DOE program and it indicates that the fuel cell cost decreases every year and DOE expects to achieve its target of \$30 kW^{-1} in 2017, although further improvements of the fuel cell technology are required.

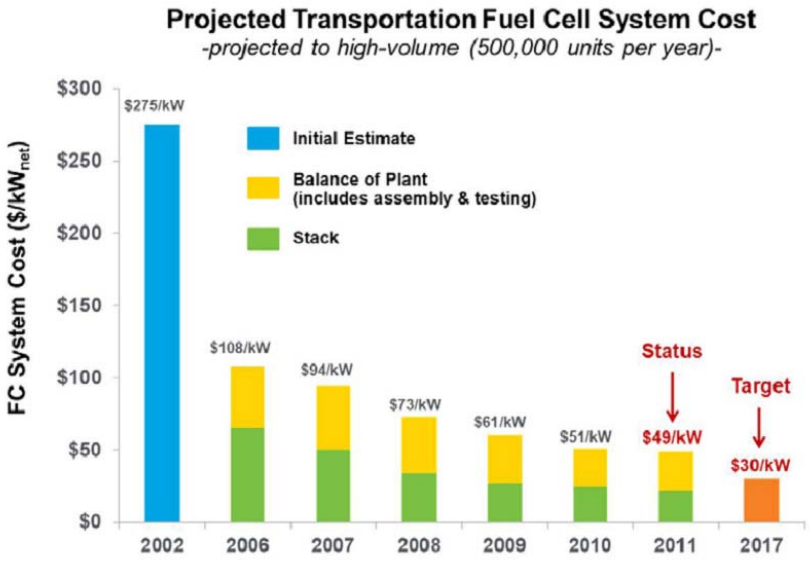

Fig. 1.5 Current modeled cost of an 80kW automotive fuel cell system (U.S. Department of Energy 2011)

1.3 Major fuel cell types and their applications

Although different types of fuel cells have been proposed, they can be categorized into five major types based on the electrolyte materials as shown in Table 1.1. Proton exchange membrane (PEM) fuel cells are promising candidates for the future energy system due to the advantages such as low operating temperature, high energy density, high efficiency and pollution-free characteristic when hydrogen is used as a fuel. The first PEM fuel cell was developed by General Electric in the early 1960s and NASA applied that technology to Project Gemini spacecraft (Spiegel 2007). Extensive fuel cell researches have been continued since that time and nowadays, the performance of current densities of 1.0 A cm^{-2} or more is achieved, while the use of platinum as a catalyst material is reduced by a factor of over 100 at the same time (Larminie and Dicks 2003). These improvements have led to huge reduction in cost per kilowatt of power ($ kW^{-1}) with much improved power density at the same time.

Table 1.1 Description of major fuel cell types (O'Hayre et al 2009)

Fuel cell	Proton Exchange Membrane (PEMFC)	Phosphoric Acid (PAFC)	Alkaline (AFC)	Molten Carbonate (MCFC)	Solid Oxide (SOFC)
Electrolyte	Polymer membrane	Liquid H3PO4	Liquid KOH	Molten carbonate	Ceramic
Charge carrier	H^+	H^+	OH^-	CO_2^{3-}	O_2^-
Operating temperature (°C)	80	200	60-220	650	600-1000
Catalyst	Pt	Pt	Pt	Nickel	Ceramic
Cell components	Carbon based	Carbon based	Carbon based	Stainless based	Ceramic based
Fuel compatibility	H_2, methanol	H_2	H_2	H_2, CH_4	H_2, CH_4, CO

The possibility of fuel cell applications expands when they are combined with vehicles, combined heat and power systems (CHP), mobile electronic equipment such as laptop/tablet computers and cellular phones. These areas will be the major areas of fuel cells applications in the future. In addition, fuel cells can be used as power systems from a few watts to megawatts by choosing suitable types of fuel cells as shown in Fig. 1.6. In this point, fuel cells are quite unique systems compared with other energy devices.

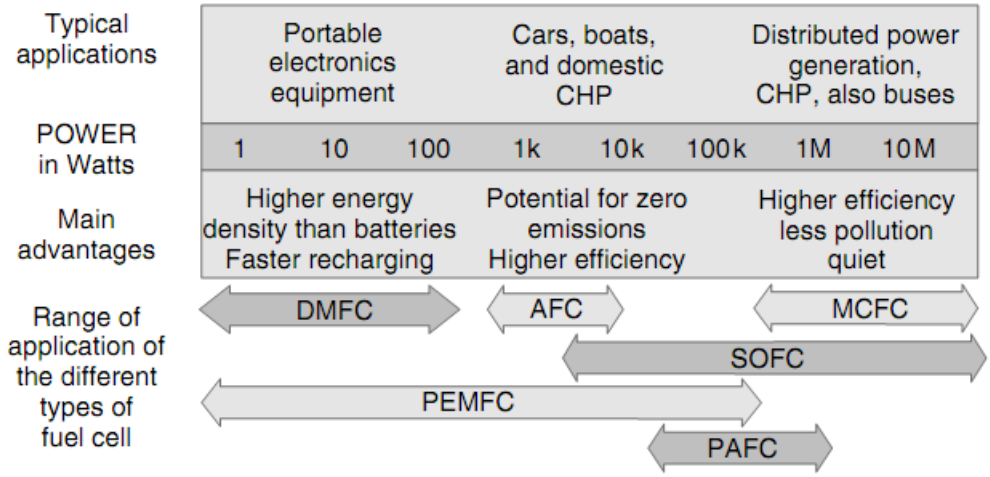

Fig. 1.6 Applications and advantages of different fuel cell types (Larminie and Dicks 2003)

1.4 Electrochemical reaction inside a PEM fuel cell

Fig. 1.7 shows a typical electrochemical reaction of a PEM fuel cell. A PEM fuel cell consists of an anode electrode where the hydrogen oxidation reaction is taking place, a cathode electrode where the oxygen reduction reaction is occurring, gas diffusion layers (GDLs), catalyst layers and a membrane electrolyte. The electrodes are porous materials in order to increase the reaction surface area and better reactants transport. Eq. (1.1)-(1.3) show the electrochemical reactions on the anode and cathode. A thin electrolyte spatially

separates the anode and cathode electrodes and it enables the electrochemical reactions at each side. Protons are generated at the anode side and transported from the anode to the cathode through the membrane electrolyte. At the same time, electrons are carried to the cathode through the external circuit. On the cathode side, oxygen reacts with protons and electrons. Finally, electricity, water and heat are generated. In addition, catalyst layers are applied both the anode and cathode sides in order to enhance the electrochemical reaction there. Reactants are transported by diffusion and/or convection to the catalyst layer. Water and waste heat produced at the cathode side also have to be continuously removed from the fuel cell in order to keep the fuel cell performance high (Spiegel 2007).

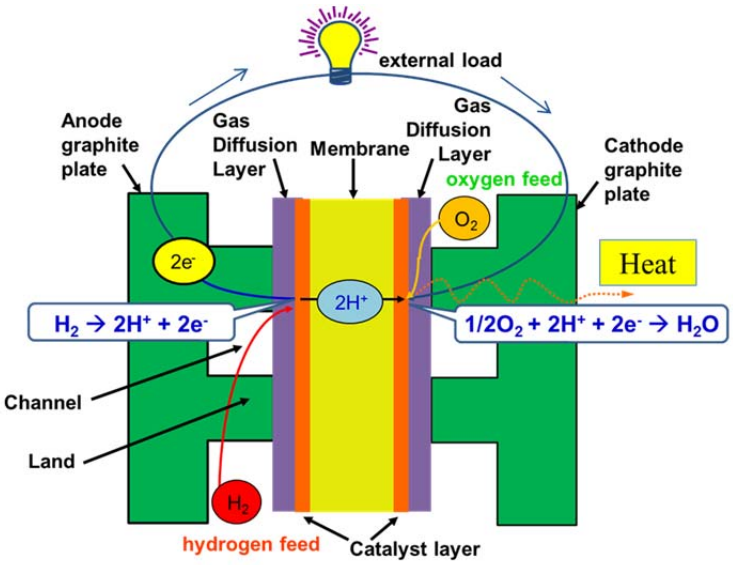

Fig. 1.7 Electrochemical reaction of PEM fuel cell

Anode side:

$$H_2 \rightarrow 2H^+ + 2e^- \qquad (1.1)$$

Cathode side:

$$\frac{1}{2}O_2 + 2H^+ + 2e^- \rightarrow H_2O \quad (1.2)$$

Overall reaction:

$$\frac{1}{2}O_2 + H_2 \rightarrow H_2O + \text{electric energy} + \text{waste heat} \quad (1.3)$$

The performance of a fuel cell is usually evaluated by a curve of its current-voltage characteristics. This result is called as a polarization curve and it describes the variation of voltage output for a given current output. A schematic of the polarization curve is shown in Fig. 1.8. The current density is typically used as a horizontal axis of this chart instead of the current itself since the current density is defined as a current divided by the active area and it enables to compare the performance of fuel cells with different size.

The ideal (thermodynamic) reversible fuel cell voltage can be calculated from the Gibbs free energy (O'Hayre et al 2009):

$$E^0 = -\frac{\Delta \hat{g}^0_{rxn}}{nF} \quad (1.4)$$

where E^0 is the standard state reversible voltage, n is the number of moles of electrons at the reaction, F is Faraday constant and $\Delta \hat{g}^0_{rxn}$ is the Gibbs free energy under the standard state condition. For a PEM fuel cell, the reversible highest voltage is about 1.23V at the standard state condition. In a real situation, the voltage output of a PEM fuel cell is lower than the thermodynamically predicted value due to several losses. Three major losses are the activation loss, the ohmic loss and the concentration loss and they characterize the shape of a polarization curve as shown in Fig. 1.8. The activation loss occurs due to the electrochemical reaction inside and it is significant at the initial part of the polarization

curve. The ohmic loss is caused by the charge transport and it mainly affects the middle part of the polarization curve. For the concentration loss, it becomes apparent at the end part of the polarization curve. In this region, although additional reactants are required in order to increase the current density, the mass transport is not enough for the reaction and finally the concentration of reactants decreases significantly. Thus, the real voltage output of a PEM fuel cell can be presented by subtracting the activation loss, the ohmic loss and the concentration loss from the thermodynamic fuel cell voltage (O'Hayre et al 2009):

$$V = E_{thermo} - \eta_{act} - \eta_{ohmic} - \eta_{conc} \quad (1.5)$$

where V is real output voltage, E_{thermo} is thermodynamic voltage, η_{act} is the activation loss, η_{ohmic} is the ohmic loss and η_{conc} is the concentration loss.

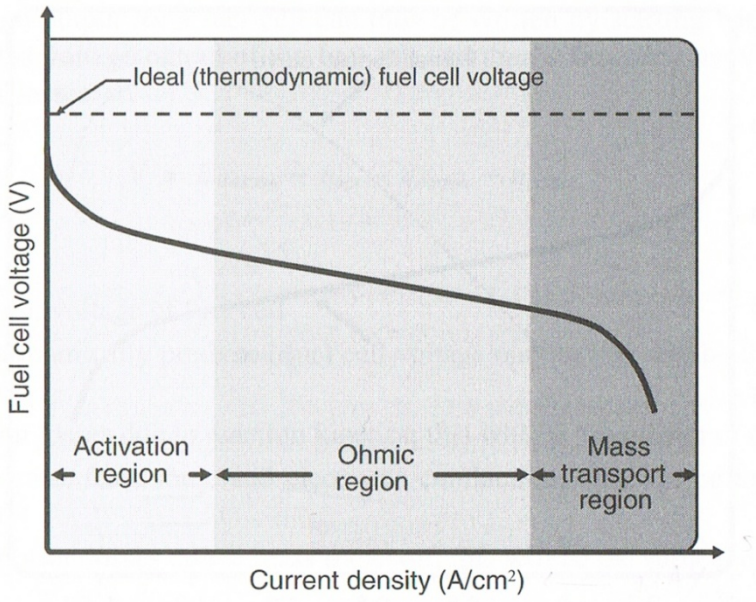

Fig. 1.8 Schematic of fuel cell polarization curve (O'Hayre et al 2009)

1.5 PEM fuel cell components

Fig. 1.9 describes the configuration of a typical single PEM fuel cell. Inside the cell, several parts are sandwiched in parallel by the end plates with several bolts. Among these components, the most important and key components are graphite plates (bipolar plates) and membrane electrode assembly (MEA), which is composed of an ion exchange membrane, GDLs and catalyst layers because they dominate the fuel cell performance.

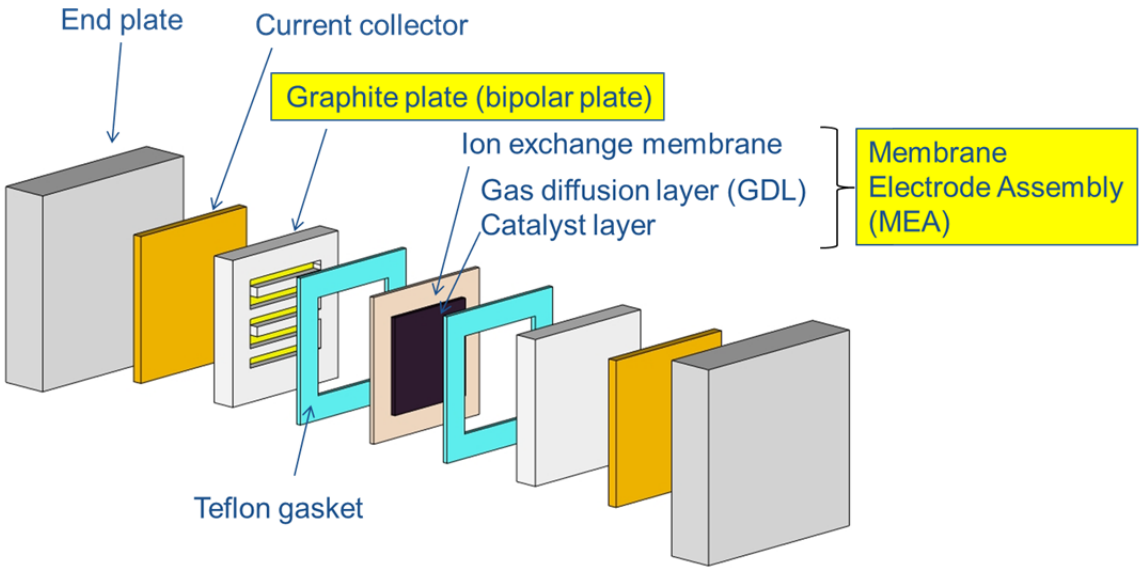

Fig. 1.9 Typical configuration of a single PEM fuel cell

1.5.1 Flow field design

Flow fields are formed at the bipolar plates for the reactants supply and removal of reaction products. Since the reactants go through a flow field, the design of a flow field significantly affects the fuel cell performance and a suitable flow field should provide adequate reactants to the catalyst layer through the GDL. Although various flow field designs have been proposed, most popular configurations are serpentine, parallel and interdigitated flow fields.

For a parallel flow field, the reactant moves each straight channel in parallel and exits through the outlet as presented in Fig. 1.10(a). In this flow field, reactants are mainly supplied to the GDL and the catalyst layer by the diffusion effect. In addition, since there are several parallel channels, the pressure drop from the inlet to the outlet becomes low. However, once water is generated by the electrochemical reaction, effective water removal cannot be realized due to the low pressure difference between the inlet and the outlet. Thus, water may block some of channels and the uneven gas distribution may occur among channels. For a serpentine flow field, since only one flow path exists from the inlet to the outlet as shown in Fig. 1.10(b), generated liquid water is easily removed from the channel by the pressure difference. In addition, when the reactant flows along that channel, a pressure difference occurs between the adjacent channels and it produces an additional convection (cross-flow) from a higher pressure channel to a lower one through the GDL under the land. Because of the diffusion and convection effects, the serpentine flow field can provide more reactants to the catalyst layer than the parallel flow field. However, this design may cause relatively high pressure drop due to the longer flow path compared with the parallel flow field. For an interdigitated flow field, the flow channels are not continuous from the inlet to the outlet as described in Fig. 1.10(c). The inlet is divided into several channels and they finally meet the dead-end and the reactants go through the GDL under the land by forced convection. Although this design can effectively remove water, the forced convection flow through the GDL requires higher pressure drops.

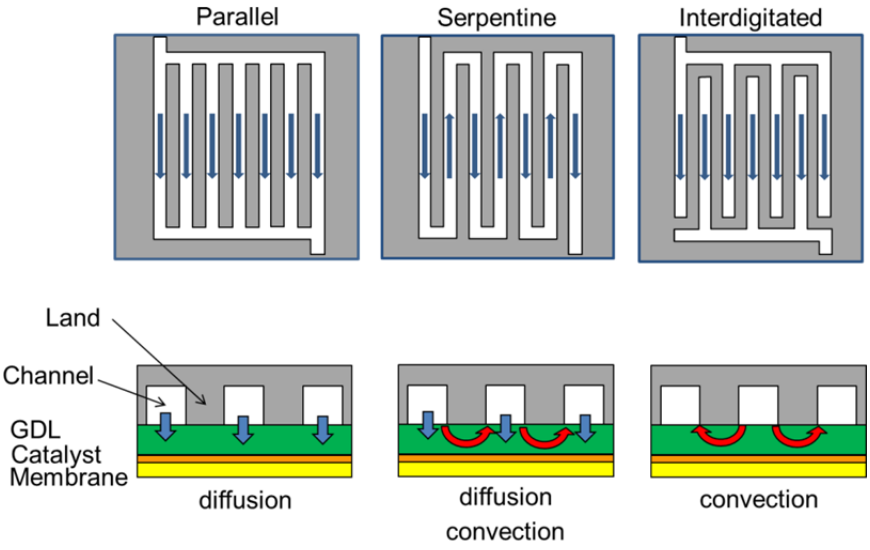

(a) Parallel (b) Serpentine (c) Interdigitated

Fig. 1.10 Typical flow field designs (O'Hayre et al 2009)

1.5.2 Membrane electrode assembly (MEA)

Membrane electrode assembly (MEA) is composed of three layers (membrane electrolyte, the catalyst layer and GDL). The schematic of MEA is shown in Fig. 1.11 and the explanation of each component is presented in the following subsections.

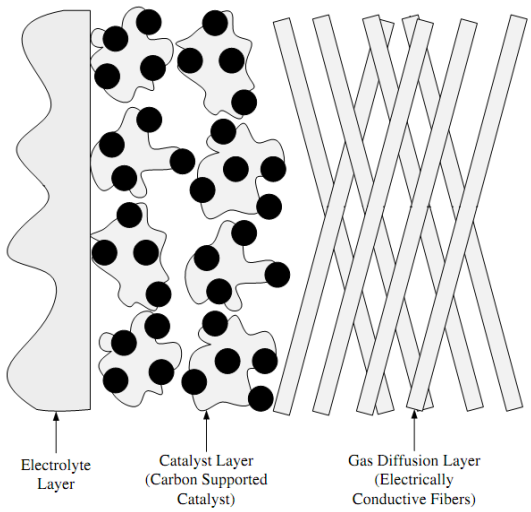

Fig. 1.11 Schematic of MEA (Spiegel 2007)

1.5.3 Membrane electrolyte

The membrane electrolyte significantly affects the fuel cell performance and following characteristics are generally required (Spiegel 2007):

- High ionic conductivity
- Adequate barrier to the reactants
- Chemical and mechanical stability
- Low electronic conductivity

Although many manufactures have produced their original electrolytes, the most well-known electrolyte for PEM fuel cells is Nafion® developed by Dupont. The starting material of this membrane electrolyte is polyethylene and it is modified by substituting fluorine for the hydrogen at first and the resulting polymer is polytetrafluoroethylene or just called as PTFE. At the next step, the sulfonic acid (HSO_3) group is added to this PTFE backbone. Since the end of this group is composed of SO_3^- ion, the resulting membrane has a strong mutual attraction between + and – ions (Larminie and Dicks 2003). At the fuel cell use, Proton can moves from one SO_3 site to another SO_3 site quite easily through the material and this membrane electrolyte becomes the very good proton conductors. The drawback of this membrane is the operating temperature. Although the fuel cell efficiency generally increases with the increase of the operating temperature, the membrane must be hydrated in order to keep the ionic conductivity. In addition, the increase of temperature softens the PTFF backbone and reduces the mechanical strength of the membrane. For these reasons, the membrane electrolyte must be used under the boiling point of water for the PEM fuel cells (Spiegel 2007).

1.5.4 Gas diffusion layer (GDL)

The GDL is located between the catalyst layer and the bipolar plate. It is made of a porous and electrically conductive material such as carbon cloths and carbon papers. Some treatments are applied to the GDL in order to increase electrical contacts and the water transport. The GDL provides not only reactants to the catalyst layer but also electrical contacts between the catalyst layer and the bipolar plate. In addition, the GDL is deformable due to the existence of numerous pores (vacancies) inside as shown in Fig. 1.12 and able to decrease the contact resistances easily by the external compression force. The interface with the catalyst layer is usually coated by a micro porous layer (MPL). The MPL consists of carbon particles with PTFE binder and this layer is hydrophobic in order to avoid the pores from clogging with water. Thus, the MPL helps exhaust the generated water from the GDL into the flow channel.

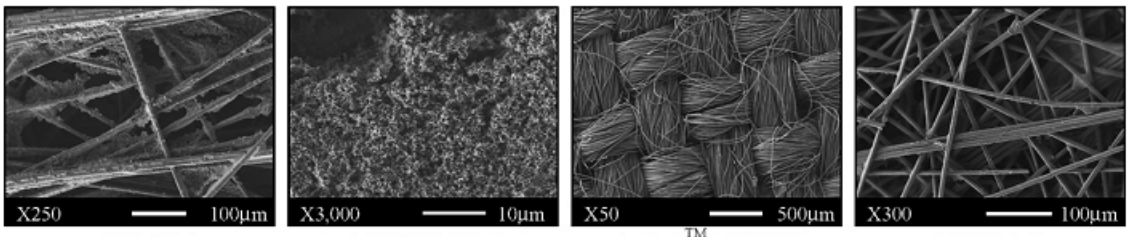

Fig. 1.12 SEM images of GDL microstructure (Spernjak et al 2007)

1.5.5 Catalyst layer

Platinum (Pt) is typically used as the catalyst layer material and it works as the electrode of PEM fuel cells. Although Pt was used at the rate of 28 mg cm^{-2} loading in the early time of PEM fuel cells development, these days, the usage has been reduced to

around 0.2 mg cm^{-2} with the increase of the power density at the same time (Larminie and Dicks 2003). Pt is formed into very small particles and dispersed on the surface of carbon substrate as shown in Fig. 1.13 in order to contact with reactants at the high efficiency. Although the actual catalyst layer is complexly surrounded by a thin ionomer film, the reaction site where the electrochemical reaction takes places is often called as the triple phase boundaries in the literature.

In general, there are two methods in order to develop the Pt particle-carbon substrate structure as the electrode. In one method, the catalyst layer is typically mixed with PTFE in order to ensure the water removal capability and it is directly applied to the membrane electrolyte. In another method, the catalyst layer is applied to the GDL with PTFE binding in order to provide not only the hydrophobicity but also the mechanical strength by the GDL (Larminie and Dicks 2003). With the latter method, the resulting structure is often called as a gas diffusion electrode (GDE).

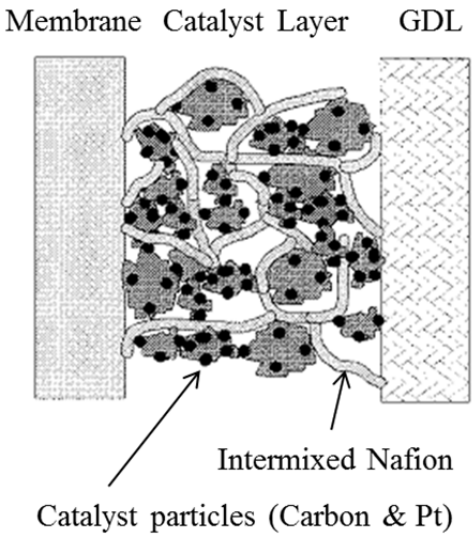

Fig. 1.13 Schematic planar representation of the catalyst layer (the small particles are Pt and dispersed on large carbon substrate) (Passalacqua et al 2001)

1.6 Outline of this thesis

Following the introduction in Chapter 1, related previous studies are reviewed in Chapter 2. The accomplished and unaccomplished works are distinguished and the objective of this study is stated in Chapter 3. The most important parts attained in this research are described from Chapter 4 to Chapter 8. Chapter 4 explains the experimental methodology and the experimental results are discussed in Chapter 5 and 6. The modeling methodology is described in Chapter 7 and the discussion is held in Chapter 8. Finally, a conclusion of this work and the suggestions for further research are stated in Chapter 9.

CHAPTER 2

REVIEW AND RELATED LITERATURE

2.1 Modeling studies

Numerical modeling is a powerful means for the prediction of transport phenomena inside fuel cells. Since the early time of the fuel cell research, the modeling development of PEM fuel cells has attracted large interest among many researchers and considerable efforts have been devoted in order to develop better numerical models with less assumptions and more physical complexities. In this review, PEM fuel cell models are classified and reviewed based on their dimensionality.

2.1.1 Zero-dimensional (0D) model

A polarization curve is a most commonly used reference for the PEM fuel cells performance. Zero-dimensional models mainly focus on the prediction of the polarization curve since that curve is useful for the experimental data analysis of fuel cell stacks, kinetic parameters determination and comparison of electrical performance of different fuel cells.

Kim et al. (Kim et al 1995) developed an empirical equation in order to calculate the voltage at different current densities. This model agreed well with experimental data over a range of temperature, pressure and oxygen flowrates. Lee et al. (Lee et al 1998) modified the equation of Kim et al. in order to account for the diffusion limitations on the cathode side. Squadrito et al. (Squadrito et al 1999) also modified the model of Kim et al. in order to include the mass transport limitation. Amphlett et al. (Amphlett et al 1995)

developed another model and applied it to the experimental data of particular fuel cell stacks. Later, Mann et al. (Mann et al 2000) modified the model of Amphlett et al. and applied it to the different fuel cell geometries.

The advantage of zero-dimensional models is their simple form and the small computational requirement in order to solve the model equations. However, these zero-dimensional models do not explicitly show the fundamental transport phenomena and electrochemical processes, such as species concentrations, temperature and the current density distribution. Therefore, the application of zero-dimensional models is limited.

2.1.2 One-dimensional (1D) model

In contrast to zero-dimensional models, one-dimensional models can handle the fuel cell components with some degrees of complexity. The numerical models developed by Springer et al. (Springer et al 1991, Springer et al 1993) and Bernardi and Verbrugge (Bernardi and Verbrugge 1991, Bernardi and Verbrugge 1992) in early 1990s are often referred to as pioneering modeling works for PEM fuel cells.

Springer et al. (Springer et al 1991, Springer et al 1993) developed a one-dimensional, isothermal and single-phase model with the experimentally derived diffusion and electro-osmotic drag coefficients of water in Nafion. Since this model was an essentially one-dimensional model including the membrane, the catalyst layer and the GDL, governing equations were solved by assuming homogeneous materials with effective transport properties. Water diffusion through the membrane and effects of water content on the membrane conductivity were also included in this model. Although their model was one-dimensional form and did not consider the thickness of the catalyst layer,

their concept of the diffusion membrane model has been widely used by the following researchers.

The simulation model developed by Bernardi and Verbrugge (Bernardi and Verbrugge 1991, Bernardi and Verbrugge 1992) was also one-dimensional, isothermal and single phase model; however, their model included both the anode and cathode catalyst layers and accounted for the transport processes in the catalyst layer. Effective transport properties such as the effective diffusion coefficient with the Bruggeman correlation were also employed. They compared the polarization curve obtained by their model with the one from the experiment and the result showed reasonably good agreement except the high current density region.

The numerical models of Springer et al. and Bernardi and Verbrugge gave valuable information regarding the electrochemical reactions inside the fuel cells that could not be explained by the zero-dimensional models and achieved a great progress in establishing a fundamental framework of the PEM fuel cell modeling. Most of the fundamental equations for the modeling development were proposed in their studies and have been widely used in the later numerical works.

2.1.3 Two-dimensional (2D) model

After Springer et al. and Bernardi and Verbrugge works, although a large number of one-dimensional models were developed, most of them studied the transport phenomena in the through-plane direction. However, the assumption of homogeneous in-plane conditions was not valid, especially at the high current density condition. Furthermore, anisotropic material properties were not treated in these one-dimensional models. One of

the largest drawbacks of one-dimensional models was that they could not simulate the reactants consumption and products generation along the channel direction and the different reactants concentration both under the channel and the land areas of the MEA. Two-dimensional models have been developed in order to overcome these insufficiencies and they can be generally divided into two categories depending on which two dimensions are used: one category considers along the flow channel direction and another treats across the flow channel direction.

2.1.3.1 Along the flow channel model

Fuller and Newman (Fuller and Newman 1993) developed a pseudo two-dimensional model and analyzed the transport phenomena along the channel direction. They also provided the general description of water transport in the membrane. Nguyen and White (Nguyen and White 1993) used algebraic expressions for the concentration distribution in the flow channel. They showed water concentration, temperature, partial pressures and current density distributions along the flow channel direction. Furthermore, they provided the results of voltage losses due to the ionic resistance of membrane. Yi and Nguyen (Yi and Nguyen 1998) investigated the convective water transport across the membrane by a pressure gradient and temperature distribution along the flow channel. From their results, it was revealed that the performance of a PEM fuel cell could be improved by humidifying the anode side. In addition, the positive pressure at the cathode side increased the fuel cell performance due to the additional water supply to the membrane.

Gurau et al. (Gurau et al 1998) developed a true two-dimensional PEM fuel cell model with defining the governing equations in the channels , GDLs, catalyst layers and a

membrane. They found a non-linear oxygen mole fraction distribution along the flow channel direction, which was different from the linear distribution assumption by the previous pseudo two-dimensional models such as Nguyen and White work. Um et al. (Um et al 2000) also proposed a similar model as Gurau et al. and they found the hydrogen dilution effect when the reformate gas was used as the anode feed. Hydrogen dilution leaded to substantial anode mass transport polarization and it caused a much lower cell current density due to the limitation of the diffusive transport of hydrogen to the reaction site. Yi et al. (Yi et al 2004) analyzed a water flow along the channel direction in order to find the dependency of operating and design parameters. The reactant utilization and a pressure drop were evaluated from the point of the system efficiency and water balance. Huang et al (Huang et al 2005) used a two-dimensional water and thermal management model in order to investigate the pressure effect along the channel direction. They showed several results such as current density, voltage loss and partial pressure distributions along the flow channel.

2.1.3.2 Across the flow channel model

Natarajan and Nguyen (Natarajan and Nguyen 2001) developed a transient two-phase model for the cathode side of a PEM fuel cell. They found that the fuel cell performance was significantly affected by the liquid water existence at high current density regions. Operational conditions and design parameters such as temperature, dryness of the reactant, GDL thickness and porosity also influenced the performance due to the variation of the liquid water removal rate. From their result, narrower land width was preferable in order to enhance the fuel cell performance.

Kazim et al. (Kazim et al 2003) proposed a simple single-component model and found that the interdigitated flow field could increase both the limiting current density and the maximum power density. Birgersson et al. (Birgersson et al 2005) developed two-phase model and investigated three cases with different thermal conditions. They also conducted the scale analysis and showed what physical phenomena affected the transport mechanism in a fuel cell. As one of their results, they found the effect of heat conduction was larger than that of heat convection.

Lin and Nguyen (Lin and Nguyen 2006) developed a two-dimensional, two-phase model in order to account for the effects of the land of the bipolar plate and the electronic conductivity of the solid phase. Their results indicated that the condition of the narrower land and the higher in-plane permeability had a better cell performance due to the increase of liquid water and oxygen transport. Although the in-plane electronic conductivity of the GDL had little influence on the performance, a non-uniform distribution of electronic current was found in the GDL and the catalyst layer when the in-plane conductivity was low.

2.1.4 Three-dimensional (3D) model for a parallel flow field

Since two-dimensional models only simulate the condition either along the flow channel direction or across the flow channel direction, they cannot give a full three-dimensional map of the transport phenomena inside a fuel cell. Thus, the development of three-dimensional models is required in order to obtain a better understanding of the actual fuel cell performance.

Zhou and Liu (Zhou and Liu 2001) conducted a three-dimensional simulation for the parallel flow channel and obtained the detailed distribution of species concentrations, current density, overpotential distribution, temperature, water content and reaction rates in a PEM fuel cell. Later, Zhou and Liu (Zhou and Liu 2006) added a new function to their previous model and analyzed the effect of different electrical conductivities of the GDL both in-plane and through-plane directions.

Um and Wang (Um and Wang 2004) also proposed a three-dimensional computational model in order to investigate the interaction between the mass transport and electrochemical kinetics of parallel and interdigitated flow fields. Their results indicated that the forced convection induced by the interdigitated flow field substantially improved the mass transport of oxygen and water removal at the catalyst layer.

Wang and Wang (Wang and Wang 2006) carried out a three-dimensional simulation of a parallel flow field with a non-isothermal two-phase model in order to investigate the liquid water distribution and flooding in a PEM fuel cell. Their result indicated that the vapor phase diffusion enhanced the water removal from the GDL under the channel area; however, it caused the flooding in the GDL under the land area. They also found that the vapor phase diffusion helped remove heat from the catalyst layer to the GDL.

Pourmahmoud et al. (Pourmahmoud et al 2011) developed a non-isothermal model and found that the larger porosity of the GDL increased the mass transport in the fuel cell. They also indicated that the oxygen molar fraction at the catalyst layer was affected by the GDL thickness.

2.1.5 Three-dimensional (3D) model for a serpentine flow field

Three-dimensional models shown in the previous section used the channel to channel symmetry in order to reduce the computational effort. Although such a simplification may be applicable for a simple design such as a parallel flow field, it is not acceptable for a fuel cell with a serpentine flow field. A serpentine flow field has only one flow path from the inlet to the outlet and it can be regarded as a series connection of parallel flow channels. Due to this configuration, the total channel length becomes longer and the local pressure difference between the adjacent channels occurs in a serpentine flow field. Thus, there is an additional cross-flow from a higher pressure channel to a lower one through the GDL under the land.

Dutta et al. (Dutta et al 2001) developed a three-dimensional numerical model in order to predict the flow in a PEM fuel cell with a serpentine flow field. Their results indicated that flow distributions in both anode and cathode channels were significantly affected by the mass consumption on the MEA. They also showed that the effect of the cross-flow was significant and the overall pressure drop became lower than that in a parallel flow field due to the cross-flow. Dohle et al. (Dohle et al 2003) studied two different cases for a serpentine flow field. The first case was that all of the flow moved only in the channel and the second one was that they only went through the GDL. The numerical result indicated that the reactants distribution became inhomogeneous across the flow field due to the existence of the cross-flow.

Nguyen et al. (Nguyen et al 2004) developed a three-dimensional model of a PEM fuel cell with a serpentine flow field. Their model featured an iterative voltage-to-current algorithm that allowed for a more realistic representation of the local activation

overpotential. The simulation results revealed that the current density was higher under the land area when the load was low and with the increase of the load, the current density maxima shifted towards the center of the channel. Sun et al. (Sun et al 2005) studied the current density distribution in a serpentine flow field. Although they used a two-dimensional model, they found that the fuel cell performance was enhanced by the cross-flow. Oosthuizen et al. (Oosthuizen et al 2005) studied the flow and temperature distributions in a serpentine flow field and found that the cross-flow became significant when the porosity of the GDL exceeded approximately 0.65. Moreover, although the cross-flow reduced the pressure drop across the flow channel, it had a small influence on temperature gradients.

Pharoah (Pharoah 2005) evaluated the cross-flow as a function of the GDL permeability. Both isotropic and orthotropic permeabilities were compared and it was found that the in-plane permeability was the dominant parameter affecting the cross-flow in a serpentine flow field. In addition, it was revealed that the cross-flow occurred when the permeability exceeded a threshold value of about 1×10^{-13} m^2. Kanezaki et al. (Kanezaki et al 2006) found that the considerable amount of the cross-flow went through the GDL under the land by the pressure difference between adjacent channels with their two-dimensional model. They also indicated that the cross-flow would be more effective in water removal from the electrode structure at the cathode, in addition to conveying oxygen with higher concentration to the catalyst layer.

Sun et al. (Sun et al 2006) simulated a flow in a serpentine flow field in a PEM fuel cell with a trapezoidal shape of the channel cross-section. They showed that the cross-flow decreased the pressure drop across the flow channel. Park and Li (Park and Li 2007)

simulated wide ranges of flowrate, permeability and thickness of the GDL in order to analyze the effects of those parameters on the resultant cross-flow. Their results revealed that the considerable amount of the cross-flow through the GDL was found and its effect on pressure drop became more significant as the permeability and the thickness of the GDL were increased.

Prasad and Jayanti (Prasad and Jayanti 2008) investigated the relationship between the cross-flow and water vapor distribution in the electrode. Their results indicated that the velocity of cross-flow was quite small under the gas channels and varied considerably under the land. In addition, the cross-flow was low at the U-bend region and was highest at the inlet. The highest concentration of the water vapor, however, was found not near the exit but in the U-bend region. They concluded that the local flooding near the U-bend was attributed to the lack of the cross-flow rather than to the corner effect of the channel. Shi and Wang (Shi and Wang 2008) studied the cross-flow with the effect of the GDL deformation due to the compression during a fuel cell assembly process. Their results showed that the performance of a PEM fuel cell decreased due to the assembly compression especially at the high current density region, since the permeability became lower by the compression. Moreover, the pressure drop from the inlet to the outlet of the flow channel increased due to the GDL intrusion into the channel. They also presented that the oxygen concentration in the channel and the GDL shifted due to the cross-flow effect. The local current density distribution at the catalyst layer had a similar shift.

Wang et al. (Wang et al 2009, Wang et al 2010) developed a three-dimensional two-phase model for PEM fuel cells and investigated the effect of the cross-flow on the performance for both single and triple serpentine flow fields at various channel aspect

ratios. Their results indicated that the cross-flow occurred under all lands for the single serpentine flow field and the difference of the current density was not large between under the flow channels and under the lands. Thus, the effect of changing the aspect ratio was small for this case. On the other hand, the cross-flow existed under several lands and the effect of changing the aspect ratio on the fuel cell performance became significant for the triple serpentine flow field. Park et al. (Park et al 2010) studied the unsteady two-phase flow in order to investigate the liquid water transport under the pressure gradient in the GDL. Their result revealed that liquid water was effectively removed from the GDL by the cross-flow. Tehlar et al. (Tehlar et al 2010) developed a pseudo three-dimensional model in order to study the effects of the pressure difference between the adjacent channels and the GDL compression in a serpentine flow field. It was found that the overall current density was enhanced by the cross-flow and a more uniform current distribution was obtained. In addition, when the land width was increased and the channel width was kept constant, the current density under the land reduced due to the decrease of the cross-flow. Additional Oxygen was also conveyed from the high pressure side to the low pressure side through the GDL with the increase of the pressure difference.

2.2 Experimental studies

Since the reactants go through the flow fields, the pressure drop (or pressure difference) of the reactants inside the flow channels is a good measure in order to investigate the phenomena in a fuel cell. During the decades, a large number of experimental works have been carried out in order to measure the pressure drop between the inlet and the outlet of flow channels.

In addition, many researchers have aggressively measured the permeability of GDLs since the permeability is one of the most important properties of the GDL and it significantly affects the fuel cell performance.

2.2.1 Measurement of pressure drop between flow channels

Water is generated by the oxygen reduction reaction (ORR) at the cathode side and also transported from the anode to the cathode by the electro-osmotic drag. Although there is back diffusion of water from the cathode to the anode due to the concentration difference, water flooding occurs at the cathode side when the water production rate exceeds the water removal rate. This liquid water may cause the increase of the pressure drop in the flow field and the measurement of the pressure drop is regarded as a good way in order to evaluate the water content in a fuel cell.

He et al. (He et al 2003) measured the pressure drop in an interdigitated flow field in order to determine the effects of liquid-water flooding in the GDL. They concluded that the increase of air flowrate or cell temperature enhanced the liquid water removal performance. Barbir et al. (Barbir et al 2005) measured inlet and outlet pressures as a function of flowrate in order to monitor the flooding in a serpentine flow field. They found that when dry air was used without any electrochemical reaction, the relationship between the flowrate and the pressure drop was almost linear. In addition, when humidified air was applied without any reaction, the pressure drop became higher due to the water condensation in the fuel cell. When the fuel cell was operated under the dry air condition with electrochemical reaction, the pressure drop was linearly proportional to the flowrate because all the product water evaporated into the air flow. Furthermore,

when air was fully humidified, evaporation of the generated water was no longer possible and the pressure drop increased exponentially with the increase of the air flowrate. Ma et al. (Ma et al 2006) developed a transparent PEM fuel cell with straight channels in order to study the correlation between the liquid water removal and the pressure drop between the inlet and the outlet of channels. Their results indicated that the pressure drop increased with the increase of liquid water content in the channel. They also showed that a pressure drop decreased sharply due to the discharge of a water blockage. Liu et al. (Liu et al 2007) visualized the flooding both at the anode and the cathode channels of a parallel flow field. The effects of the cell temperature, current density and operating time on the total pressure drop were also studied. As a result, the total pressure drop between the inlet and the outlet increased with the increase of the current density; however, the total pressure drop decreased with the increase of the cell temperature. In addition, the total pressure drop in the cathode flow channel was higher than that in the anode flow channel due to the presence of water.

In these aforementioned studies, although fuel cells were evaluated by the pressure drop, it was not measured inside the fuel cell but at the feeding and exhausting lines of the experimental setups. Kandlikar et al. (Kandlikar et al 2009) developed a new setup in order to directly measure the pressure in a parallel flow field. They drilled tapping holes in the flow channels in order to measure the inside pressure and transformed the pressure drop into the function of the flowrate. Finally, they found the existence of the flow maldistribution in each parallel channel although the cell temperature was limited up to 35°C due to the experimental restriction. Lu et al. (Lu et al 2009) also visualized the flow

maldistribution by using the same experimental setup of Kandlikar et al.; however, the electrochemical reaction of a fuel cell was not considered in their study.

Zhang et al. (Zhang et al 2010) used a similar method as Kandlikar et al. in order to explain the maldistribution of gas–liquid two-phase flow in a parallel flow field. However, there was no electrochemical reaction in their research. Jiao et al. (Jiao et al 2010) investigated characteristics of liquid water removal from the GDL by measuring the pressure drop in a serpentine flow field. They showed that the thickness of the GDL and the reactant flowrate significantly affected on characteristics of liquid water removal. They also found that although severe compression of the GDL brought an excessive pressure drop from the inlet to the outlet of the channel, it was possible to effectively remove water with the increase of the inlet flowrate.

2.2.2 Measurement of GDL permeability

One of the critical properties of a GDL is the gas permeability since it significantly affects the fuel cell performance. A large number of studies have been carried out for the evaluation of the permeability.

Williams et al. (Williams et al 2004a) investigated some critical properties of the GDL, such as the limiting current, electronic resistivity, fraction of hydrophobic pores, gas permeability, pore size distribution and surface morphology. They measured the through-plane permeability of several GDLs and showed that the limiting current increased linearly with the increase of the permeability. Williams et al. (Williams et al 2004b) also used three GDLs with distinctively different permeability in order to evaluate the effect of GDL permeability on the fuel cell performance. Although they used an ex

situ apparatus for the permeability measurement and the polarization curves were obtained by a single serpentine fuel cell separately, they revealed that when the cathode flowrate increased, the limiting current increased due to the convection effect.

Feser et al. (Feser et al 2006) evaluated the in-plane permeability by the pressure drop through the radial GDL samples. They also investigated the compressibility effect of a GDL and found when the GDL was compressed, the in-plane permeability decreased. Gostick et al. (Gostick et al 2006) developed ex situ experimental apparatuses and found that the in-plane permeability was higher than the through-plane permeability for most GDL materials. Moreover, they carried out an analysis of the non-Darcy effect in the GDLs and revealed that when the flowrate was higher, inertial losses became significant and Darcy's law did not accurately describe pressure drops inside the GDL. Gurau et al. (Gurau et al 2007) measured the in-plane permeability and through-plane permeability for several GDLs with different PTFE loading. They applied the Darcy-Forchheimer equation in order to calculate the permeability and showed that PTFE loading affected both in-plane and through-plane permeabilities.

Ismail et al. (Ismail et al 2010a) investigated the through-plane permeability for untreated and PTFE-treated GDLs. They found that there was an optimum value of PTFE loading, at which the through-plane permeability became a maximum. The investigation of the inclusion of the air compressibility when solving the Darcy law was also performed. Ismail et al. (Ismail et al 2010b) also measured the in-plane permeability using a similar experimental setup used by Gostick et al. Their results indicated that the in-plane permeability decreased with the increase of the PTFE loading on a GDL.

Besides, they found when the in-plane permeability was measured, the exclusion of the non-Darcy terms resulted in a significant error at high flowrates.

Hussaini and Wang (Hussaini and Wang 2010) determined experimentally not only the absolute permeability but also the relative permeability in both through-plane and in-plane directions. As a result, they established correlations for the in-plane relative permeability of water and air. However, they used an ex situ apparatus and no electrochemical reaction occurred in their setup. Hence, both air and water were supplied directly to the GDL samples in order to simulate an actual fuel cell condition.

2.2.3 Measurement of the cross-flow

When reactant gases flow along a channel in a serpentine flow field, a pressure difference occurs between the adjacent channels and it produces the cross-flow from the higher pressure channel to the lower pressure channel through the GDL. As previously stated, many modeling works indicated that the cross-flow significantly affected the fuel cell performance and the experimental evaluation of the cross-flow is strongly desired.

Higier and Liu (Higier and Liu 2009) separately measured the current density under the channel and the land areas in a serpentine flow field and evaluated the current density difference between them. They compared the result of a serpentine flow filed with the one of a parallel flow field and found that the current density difference of the serpentine flow field was higher than that of the parallel flow field due to the existence of the cross-flow. Jiao et al. (Jiao et al 2010) observed the cross-flow motion in a transparent serpentine flow field and found that the cross-flow worked effectively in order to remove water under the land area of the serpentine flow field.

Choi et al. (Choi et al 2011) added sub-channels and by-passes to the serpentine flow field in order to promote the cross-flow. They compared the performance of their new flow field with the one of the conventional serpentine flow field and found that the maximum current and power densities of their new flow field were increased. Recently, Bachman et al. (Bachman et al 2012) measured the current density of a parallel flow field which could change the back pressure between the adjacent channels. They found that the cell performance varied with the increase of the pressure difference and concluded that this was due to the effect of the cross-flow although the evaluation of the cross-flow was not carried out in their study.

As shown in these previous studies, although the effect of the cross-flow was pointed out in some experimental studies, the quantitative evaluation of the cross-flow had not been performed by the experiment. Moreover, some studies concluded that it was impossible to know precisely how much cross-flow occurred and went through the GDL due to the difficulty of the in situ measurement of the cross-low (Gostick 2009, Gostick et al 2006).

CHAPTER 3

OBJECTIVE OF STUDY

As can be seen from the literature survey in the previous chapter, a large number of modeling works have been carried out and it is presented that the cross-flow supplies the additional reactants to the GDL under the land area and enhances fuel cell performance. However, there has not been any quantitative evaluation of the cross-flow by the experiment since it is difficult to measure it in an actual fuel cell.

A large number of efforts have been devoted for the measurement of permeability; however, special ex situ fixtures were used in the experiment instead of real fuel cells and only the in-plane permeability or the through-plane permeability could be measured with one setup. On the other hand, the effective permeability, which is a combination of these two permeabilities, should be measured for the real fuel cell evaluation since the reactant goes through the GDL both in-plane and through-plane directions at the same time. Furthermore, although almost all of the previous studies measured the in-plane/through-plane permeability only at the dry condition, the effective permeability should be evaluated not only at the dry condition but also at the humid condition since actual fuel cells are operated with humidity.

Finally, when the performances of different designs such as the serpentine and the interdigitated flow fields are compared, a single fuel cell is usually disassembled and a flow field is replaced to another one and then, the fuel cell is assembled again. However, once a fuel cell is disassembled and re-assembled, its performance changes considerably even if the fuel cell components and the assembling compression are precisely same (Ge

et al 2006). Thus, the seamless measurement from one design to another one without disassembling and re-assembling is required for the precise evaluation of the performance between different flow field designs.

In this work, a unique experimental fixture is developed and the effective permeability and the cross-flow are directly measured in an actual fuel cell. The non-Darcy effect is investigated and effects of the land width and the operational condition are evaluated. A general correlation of the cross-flow at different operational conditions is also investigated. The current density and the power density are measured and the relationship between the fuel cell performance and the pressure difference or stoichiometry is evaluated. A three-dimensional PEM fuel cell model is developed and the flow fields, the oxygen distribution and the local current density distribution around the land area are also studied. Finally, based on these attainments, guidance for the optimal flow field design is proposed.

CHAPTER 4

EXPERIMENTAL METHODOLOGY

4.1 Experimental setup

A test station used for the experiment is G60 Fuel Cell Test System (Hydrogenics). This test station can control the inlet gas flowrate, gas temperature and humidity of both anode and cathode sides. In addition, it can change the fuel cell operating temperature. A schematic of the test station is shown in Fig. 4.1.

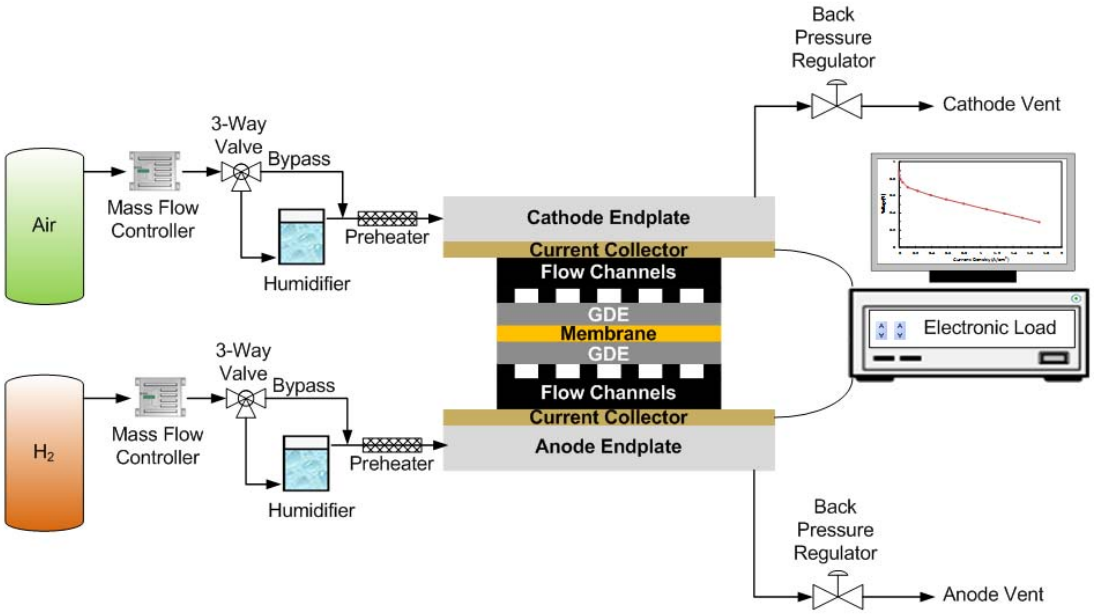

Fig. 4.1 Schematic of the fuel cell test station

A single fuel cell, which consists of the membrane electrode assembly (MEA), two graphite plates, two current collector plates, two Teflon® gaskets and anode and cathode end plates, is used for this study. The flow field used for the anode side is a triple

serpentine flow pattern with a rectangular channel of 1 mm in width 1 mm in depth and 7 paths (14 times of 180 degree terns). The length of a single channel is 7.1 cm and the total active area is 50 cm^2. A flow field of the cathode side is specially designed and composed of two parallel channels and an external flow path as shown in Fig. 4.2.

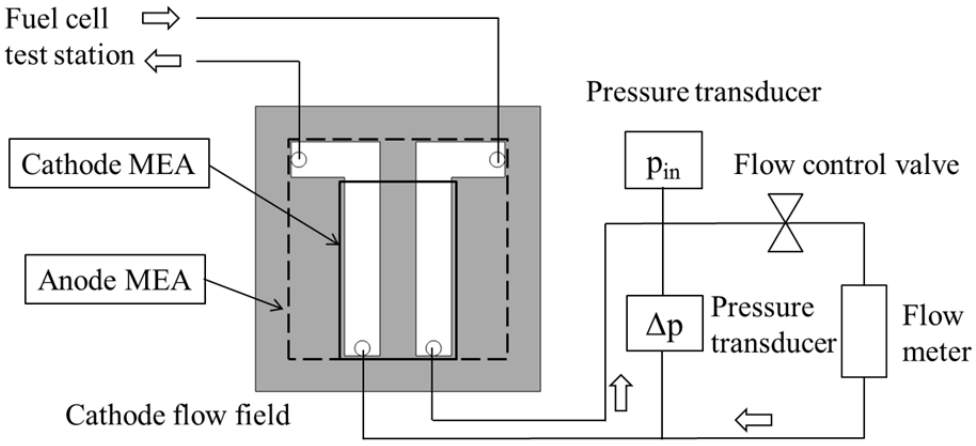

Fig. 4.2 Schematic (not to scale) of the flow field and the external flow section at the cathode side with MEAs of anode and cathode sides

These two channels are externally connected at the measurement section and the cathode flow field works as a single serpentine channel. The channel length, width and depth of the cathode side are 6.0 cm, 1 mm and 1 mm, respectively. Besides, in order to evaluate the effect of the land width, two flow fields with different land widths are manufactured by Fuel Cell Technologies, Inc. and one flow field has a land of 1 mm in width and another has a land of 2 mm in width. In the measurement section of the cathode side, one flow meter (rotameter), two pressure transducers, and one flow control valve are also installed.

The flowrate of air in the external flow path is measured by a rotameter (Omega, FL-3688G). Since the manufacturer provided the performance sheet of this rotameter only at

the standard condition (1 atom, 21°C), the calibration curves are obtained under the experimental conditions before the actual measurement. Fig. 4.3 shows the calibration curve for the dry condition. In this condition, temperature of air is set to the room temperature and the relationship between the scale reading on the rotameter and the flowrate is derived. Fig. 4.4 presents the calibration curve for the humid condition. In the humid condition, air is set to the temperature of 70°C and fully humidified. In addition, since the tolerance of this rotameter is 2% of the full scale, 0.5 L min^{-1} of the flowrate is used as the minimum flowrate for the flowrate measurement in order to ensure the experimental accuracy.

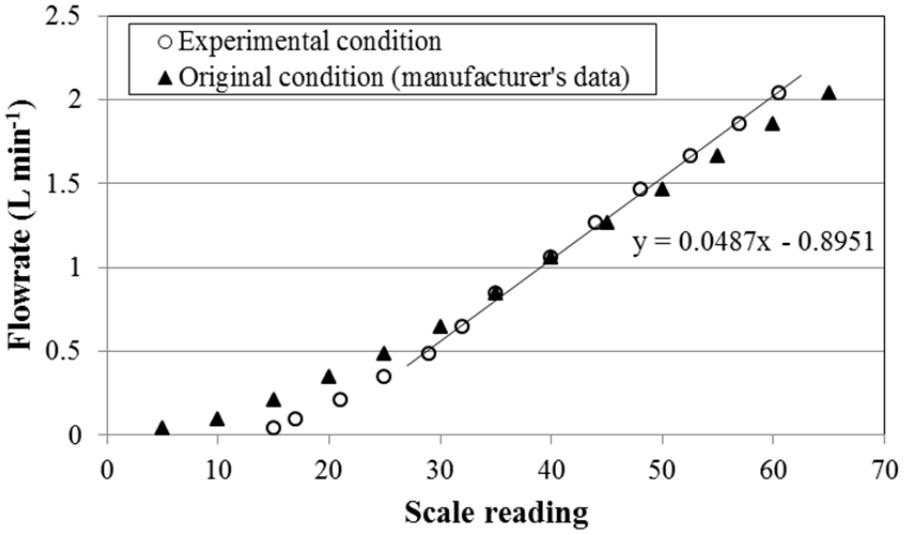

Fig. 4.3 Flow meter calibration for the dry condition

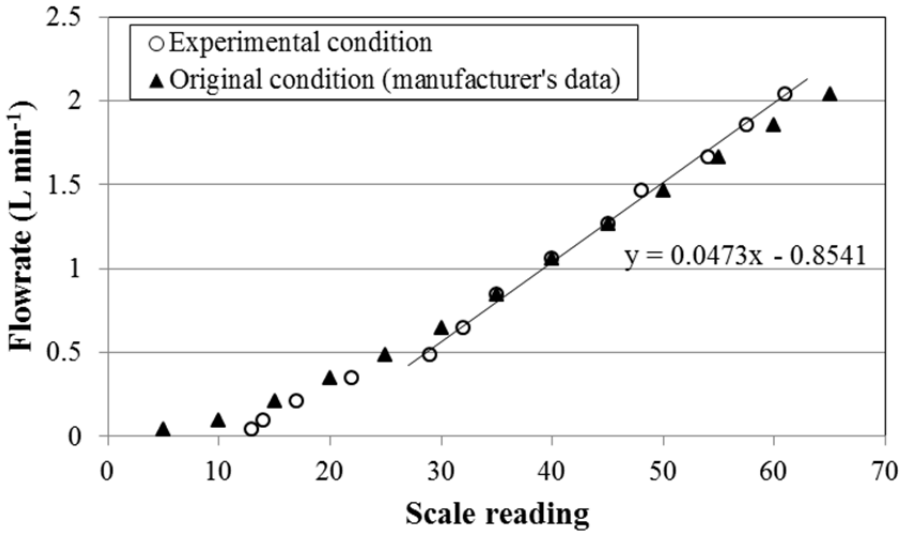

Fig. 4.4 Flow meter calibration for the humid condition

The pressure at the first channel is measured by a pressure transducer (Omega, PX409-050G5V) and the pressure difference between the first and second channels is obtained by the differential pressure transducer (Omega, PX409-015DWU5V). The data measured by these pressure transducers are recorded with the data logger (Omega, OM-CP-QUADVOIT-AC) and transmitted to the computer. The pressure difference between these adjacent channels is controlled by the flow control valve (Nupro Company). When the flow control valve is fully opened, the flow field works as a serpentine flow field and some of the inlet gas go through the external flow path to the next channel and others move across the GDL under the land; when the valve is completely closed, the flow field acts as an interdigitated flow field and all of the inlet gas flow through the GDL under the land; when the valve is partially closed, the flow field can simulate the upstream portion of a serpentine flow field with long channels or some hybrid flow fields. By adjusting the closure of this flow control valve, the fuel cell performance can be seamlessly measured from the serpentine flow field to the interdigitated flow field. In addition, since this

control valve has accurate readings on its handle, the experiment can be repeated under the same condition in order to ensure the accuracy and reliability.

4.2 Material

In-house MEA is used in this experiment. The membrane material is Nafion®112 and E-TEK ELAT® carbon cloth is used for the GDL material. This GDL is catalyzed with 0.4 mg cm^{-2} platinum loading and the gas diffusion electrodes (GDEs) for both anode and cathode sides are fabricated by BCS Fuel Cells. Two GDEs and one piece of the membrane are hot-pressed in our facility and the in-house MEA is finally manufactured. As shown in Fig. 4.2, the size of the GDE differs between anode and cathode sides. A full size GDE is used for the anode side in order to minimize any effects from the anode to the cathode sides. For the cathode side, a GDE covers the areas under the land and two channels in order to measure the current density of these areas and similar method was employed by previous studies (Higier and Liu 2010, Wang and Liu 2008). Finally, in-house MEA, two graphite plates, two current collector plates, two Teflon® gaskets and anode and cathode end plates are assembled by applying torque of 6.2 N m to eight locking bolts.

4.3 General operating procedure

Compressed air is supplied from the gas cylinder to the cathode inlet and compressed hydrogen is provided to the anode inlet of the test station. A leak-check is performed before the experiment and each experiment is conducted at pre-determined operating conditions as shown in Table 4.1. The experimental conditions are as follows unless

otherwise stated. For the dry gas condition, the fuel cell is kept under the room temperature and the gases are not humidified. For the humid case, reactant gases are fully humidified and heated up to 80°C and 70°C for the anode and cathode sides, respectively. Fuel cell temperature is also kept at 70°C in this case. The inlet flowrate, gas temperature, humidity of both anode and cathode sides and the cell temperature are controlled and measured by the test station. The first channel pressure (p_{in}), the pressure difference between the first and the second channels (Δp), and the flowrate inside the channel are measured at the external flow path of the cathode side.

Table 4.1 Experimental conditions

Parameters	Dry condition	Humid condition
Anode temperature (°C)	Room temperature	80
Cathode temperature (°C)	Room temperature	70
Fuel cell temperature (°C)	Room temperature	70
Anode humidity (%)	0 (dry)	100
Cathode humidity (%)	0 (dry)	100

4.4 Data analysis of the effective permeability and inertial coefficient

In an actual fuel cell, air moves the GDL in the through-plane and the in-plane directions at the same time by the convection flow between adjacent channels. Thus, it is reasonable to measure the combined permeability of both through-plane and in-plane directions. This permeability is called as the effective permeability. For the effective permeability measurement, the flow control valve at the cathode external path is completely closed in order to make all of the inlet flow go through the GDL under the land. When the gas velocity is sufficiently low, most of the pressure drop is caused by the

viscous effect and the flow passing through the GDL is governed by Darcy's law:

$$-\nabla p = \frac{\mu}{k} v \tag{4.1}$$

where p is pressure, μ is viscosity, k is permeability and v is velocity. v can be also written as:

$$v = \frac{m'}{\rho} \tag{4.2}$$

where ρ is density and m' is air mass flux through the GDL. Further, from the ideal gas law, ρ can be expressed as:

$$\rho = \frac{pM_w}{RT} \tag{4.3}$$

where M_w is the molecular weight of air, R is the universal gas constant and T is temperature. Putting Eq. (4.2) and Eq. (4.3) into Eq. (4.1) and re-arranging Eq. (4.1), we have:

$$-\frac{\partial p}{\partial x} = \frac{\mu RTm'}{kpM_w} \tag{4.4}$$

By integrating Eq. (4.4) from the inlet pressure ($p=p_{in}$) to the outlet pressure ($p=p_{out}$) across the land width of L, finally one-dimensional Darcy's Law yields (Ismail et al 2010b):

$$p_{in}^2 - p_{out}^2 = \frac{2RTL}{M_w}\frac{\mu}{k}(m') \tag{4.5}$$

The right hand side of Eq. (4.5) accounts for the pressure drop by the viscous effect. When the velocity becomes relatively high, an inertial effect is induced by the acceleration and deceleration inside the porous media of the GDL and another term is added to the Darcy's law (Gostick et al 2006):

$$-\nabla p = \frac{\mu}{k} v + \beta \rho v^2 \tag{4.6}$$

where ρ is density and β is the inertial coefficient. This equation is called as the modified Darcy's law or Forchheimer equation. The first term of the right hand side is called as the Darcy term and the second one is referred as the non-Darcy term which explains the pressure drop by the inertial effect inside the GDL. In the same manner of the derivation of Eq. (4.5), the integration of Eq. (4.6) is given as (Gostick et al 2006, Ismail et al 2010a):

$$p_{in}^2 - p_{out}^2 = \frac{2RTL}{M_w} \frac{\mu}{k} (m') + \frac{2RTL}{M_w} \beta (m')^2 \tag{4.7}$$

In the experiment, the inlet pressure p_{in} is measured by the pressure transducer at the external flow path and the outlet pressure p_{out} is obtained by subtracting the pressure difference Δp from the inlet pressure p_{in}. Temperature T is measured by the thermocouple connected to the fuel cell test station and the viscosity of air is calculated by the Sutherland's empirical formula (Ismail et al 2010a). The universal gas constant R and the molecular weight M_w are chosen to 8.314 J mol^{-1} K^{-1} and 0.02884 kg mol^{-1}, respectively. When the air velocity is low, the permeability can be obtained by fitting Eq. (4.5) to the experimental data and extracting the linear coefficient; when the air velocity is high, the permeability and the inertial coefficient are evaluated by fitting Eq. (4.7) to the data and extracting the linear and quadratic coefficients, respectively. Fig. 4.5 shows the example of the experimental result of $p^2_{in} - p^2_{out}$ as a function of air mass flux for the 1 mm width land under the dry condition. Since a non-linearity can be seen from this result due to the inertial effect inside the porous media of the GDL, the permeability and the inertial coefficient can be determined by fitting Eq. (4.7) instead of Eq.(4.5).

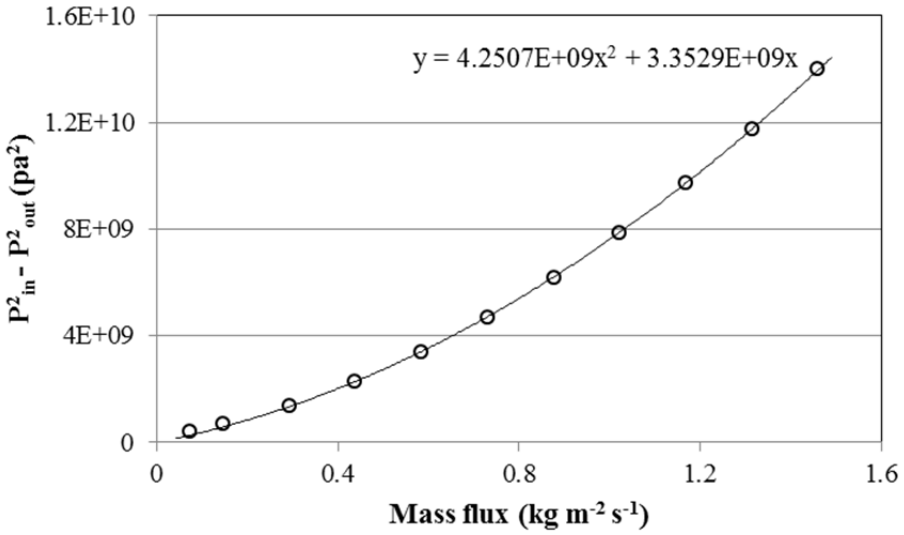

Fig. 4.5 Experimental result of $p^2_{in} - p^2_{out}$ as a function of air mass flux

4.5 Data analysis of cross-flowrate

Air inlet flowrate is set to pre-determined values by the test station in order to measure the cross-flow. The flowrate inside the channel is directly measured by a rotameter at the external flow path of the cathode side. Since this flowrate corresponds to the one in the channel, the flowrate of the cross-flow is obtained by subtracting the channel flowrate from the inlet flowrate as shown in Fig. 4.6. After obtaining the flowrates of the inlet and the cross-flow, the cross-flow is evaluated by the cross-flowrate, which is defined as the ratio of the flowrate of the cross-flow to the one of the cathode inlet (Park and Li 2007):

$$Q^*_{cross} = \frac{Q_{cross}}{Q_{in}} \times 100(\%) \tag{4.8}$$

where Q_{in} is the cathode inlet flowrate and Q_{cross} is the flowrate of the cross-flow. Once the cross-flowrate is obtained, the valve closure of the flow control valve is set to the next pre-determined position in order to increase the pressure difference between the adjacent

channels. The same procedure is repeated until the control valve is fully closed and finally the relationship between the cross-flowrate and the pressure difference is obtained.

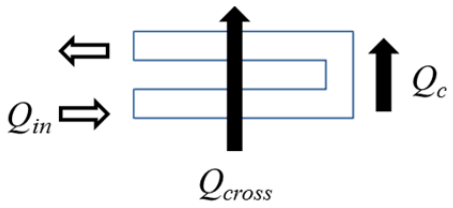

$$Q_{cross} = Q_{in} - Q_c$$

Fig. 4.6 Measurement of flowarete of the cross-flow

4.6 Methodology of current density and power density measurement

Compressed hydrogen and air are fully humidified by the test station and heated up to 80°C and 70°C for the anode and cathode sides, respectively for the current density and the power density measurements. Fuel cell temperature is kept at 70°C during the experiment. The first channel pressure (p_{in}), the pressure difference between the first and the second channels (Δp) and the flowrate inside the channel are measured at the external flow path of the cathode side. Although the inlet flowrate of hydrogen is kept at 1.0 L min^{-1}, the inlet flow rate of air is chosen from either 1.0 L min^{-1} or 2.0 L min^{-1} depending on the objective of each experiment. Four different valve closure conditions, i.e., zero closure, low closure, medium closure and full closure, are defined between the fully opened to the fully closed conditions and polarization curves are measured at each valve closure. During the experiment, the voltage is decreased from the no electric load condition to 0.25V and three times measurements are conducted for each valve closure condition. Finally, these three curves are averaged each other and the resultant polarization curve is obtained. The polarization curve is evaluated in terms of the valve closure which corresponds to the pressure difference between the adjacent channels. In

addition, in order to evaluate the relationship between the fuel cell performance such as current density and power density and the cross-flow, the cross-flowrate defined in Eq. (4.8) is also measured.

CHAPTER 5

IN SITU MEASUREMENT OF EFFFECTIVE PERMEABILITY AND CROSS-FLOW

5.1 Effective permeability and inertial coefficient

Fig. 5.1 shows the experimental result of the square of the pressure difference as a function of air mass flux for the 1 mm width land under the dry condition. A non-linearity can be seen from this result due to the inertial effect inside the GDL; thus, the permeability and the inertial coefficient can be determined by fitting Forchheimer equation shown in Eq. (5.1) to the experimental data.

$$p_{in}^2 - p_{out}^2 = \frac{2RTL}{M_w}\frac{\mu}{k}(m') + \frac{2RTL}{M_w}\beta(m')^2 \qquad (5.1)$$

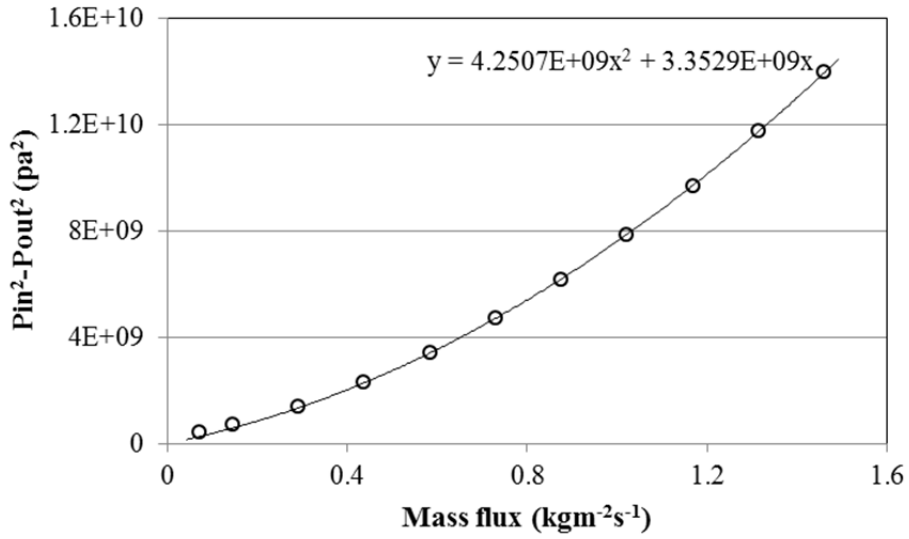

Fig. 5.1 Result of $p^2_{in} - p^2_{out}$ as a function of air mass flux for 1 mm width land under the dry condition

The experiments for different land widths and operational conditions are also carried out in order to investigate these effects on the effective permeability and the inertial coefficient. Fig. 5.2 shows the result of the square of the pressure difference for different land widths and operational conditions. The pressure difference increases with the increase of the mass flux and a non-linearity can be seen, clearly indicating the existence of the inertial effect inside the GDL. Thus, the effective permeability and the inertial coefficient should be determined by fitting Eq. (5.1) for these cases. Fig. 5.2 also shows that the pressure difference under the humid condition is greater than that under the dry condition for both 1 mm and 2 mm width lands. When the fuel cell is fully humidified under the humid condition, excessive water is accumulated inside the pores of the GDL and it interrupts the air transport through the GDL between the adjacent channels. Since this water reduces the effective permeability of the GDL, the pressure difference under the humid condition becomes higher. Besides, the pressure difference for the 2 mm width land is higher than that for the 1 mm width land due to the difference of the inertial effect.

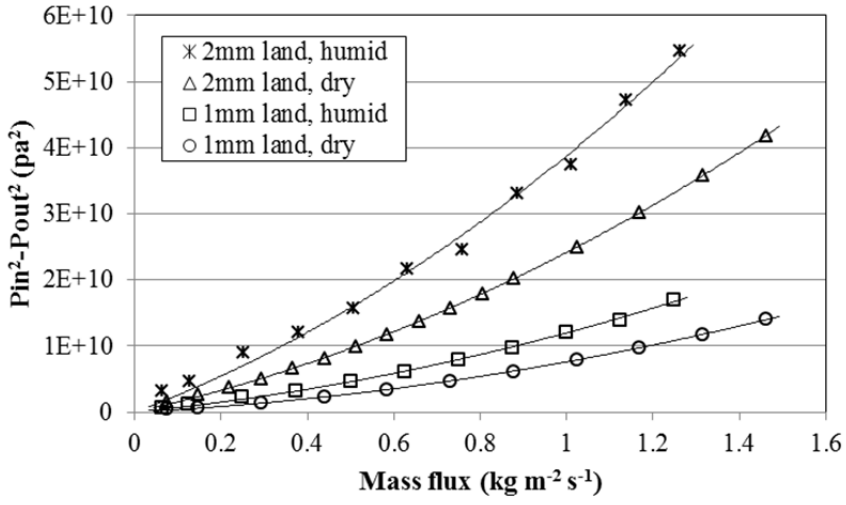

Fig. 5.2 Result of $p^2_{in} - p^2_{out}$ as a function of air mass flux for different conditions

The effective permeability and the inertial coefficient obtained by fitting Eq. (5.1) are summarized in Table 5.1. The effective permeability at the humid condition is lower than that at the dry condition because water clogs some of the pores inside the GDL at the humid condition. When the result of the1 mm width land is compared with the one of the 2 mm width land, it can be seen that the 1 mm width land shows the higher effective permeability than the 2 mm width land for both the dry and the humid conditions. The effective permeability can be expressed as Eq. (5.2) by arranging Eq. (5.1):

$$k = \frac{\frac{2RTL}{M_w}\mu(m')}{p_{in}^2 - p_{out}^2 - \left\{\frac{2RTL}{M_w}\beta(m')^2\right\}} \tag{5.2}$$

where the last term of the denominator is the non-Darcy term which shows the inertial effect. From Eq. (5.2), it is revealed that the effective permeability is associated with the inertial effect and if the inertial effect is large, the effective permeability also becomes high. Thus, the effective permeability of the 1 mm width land becomes higher since the inertial effect of the 1 mm width land is larger than that of the 2 mm width land.

Many studies separately measured the in-plane and through-plane permeabilities (Feser et al 2006, Gostick et al 2006, Gurau et al 2007, Hussaini and Wang 2010, Ismail et al 2010a, Ismail et al 2010b, Mathias et al 2003, Williams et al 2004a). Although their results were scattered because the GDL materials and experimental conditions were different, the typical permeability ranges within the order of 10^{-13} – 10^{-11} m^2 and the effective permeability obtained in this study is included within this range. From these results, it can be said that both the land width and the operational condition are important factors that affect the mass transport in the GDL and the effective permeability.

Table 5.1 Effective permeability and inertial coefficient

Case	Effective permeability k (m^2)	Inertial coefficient β (m^{-1})
1 mm width land (dry)	1.113×10^{-12}	2.075×10^{7}
1 mm width land (humid)	7.268×10^{-13}	1.790×10^{7}
2 mm width land (dry)	4.718×10^{-13}	1.130×10^{7}
2 mm width land (humid)	3.615×10^{-13}	9.766×10^{6}

Since the inertial coefficient indicates how much inertial effect occurs inside the GDL, a new dimensionless number is defined as a ratio of the non-Darcy term to the Darcy term (Ma and Ruth 1993, Ruth and Ma 1992) in order to evaluate the non-Darcy effect:

$$F_o = \frac{non\text{-}Darcy\ term}{Darcy\ term} = \frac{k\beta m'}{\mu} \tag{5.3}$$

where *Fo* is called as the Forchheimer number and it shows the effect of inertia in the GDL on the viscosity. Fig. 5.3 shows the result of Forchheimer number calculation as a function of mass flux. It is revealed that the case for the 1 mm width land under the dry condition always shows the highest Forchheimer number and the case for the 2 mm width land under the humid condition has the lowest number due to the difference of the inertial effect inside the GDL.

When the Forchheimer number is large, the inertial effect becomes significant and the Darcy's law does not account for the transport phenomena accurately. Zeng and Grigg (Zeng and Grigg 2006) proposed a following criterion, called as the non-Darcy effect, which indicates how much error is incurred if the inertial effect is ignored:

$$E = \frac{F_o}{1 + F_o} \times 100(\%) \tag{5.4}$$

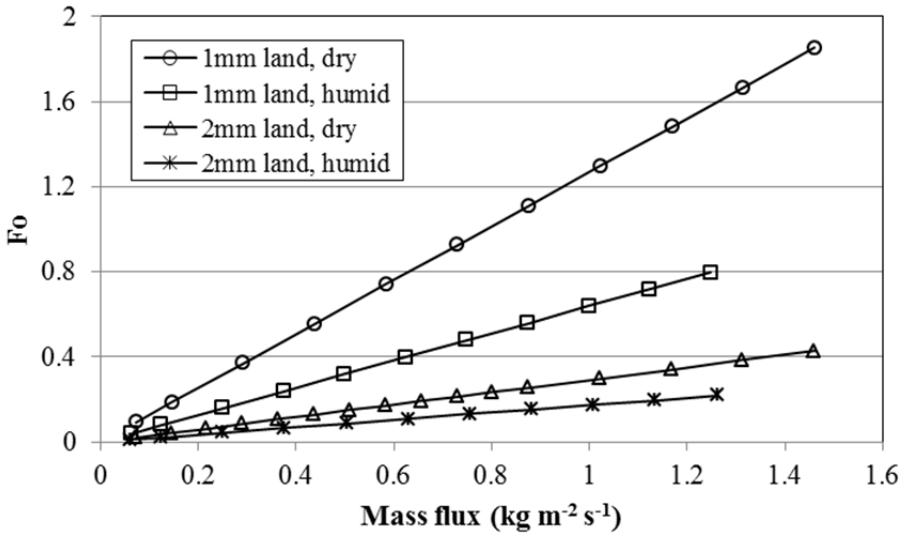

Fig. 5.3 Forchheimer number as a function of air mass flux at different land widths and operational conditions

Using Eq. (5.4), the non-Darcy effect is compared for different land widths and operational conditions and the result is shown Fig. 5.4. The non-Darcy effect for the 1 mm width land is higher than that for the 2 mm width land both under dry and humid conditions. This is because air can go through the GDL easily for the 1 mm width land under the dry condition compared with the 2 mm width land under the humid condition. In addition, it is found that the non-Darcy effect increases with the increase of the mass flux. Hence, the geometric and the operational conditions are important factors in order to accurately evaluate the effective permeability and the inertial coefficient. When the mass flux is lower than about 0.08 kg m^{-2} s^{-1}, the non-Darcy effects become less than 10% and Zeng and Grigg (Zeng and Grigg 2006) suggested a criterion that 10% of the non-Darcy effect might be acceptable error for most cases. Considering this criterion, the non-Darcy effect on the case of the 1 mm width land under the dry condition is easily beyond 10% and this means that the inertial effect in the GDL is significant for this case due to the

short width of land and the absence of liquid water. On the other hand, the non-Darcy effect on the case of the 2 mm width land under the humid condition keeps lower than 10% for the wide range of the mass flux and it can be said that the wide land and liquid water hold the inertial effect inside the GDL.

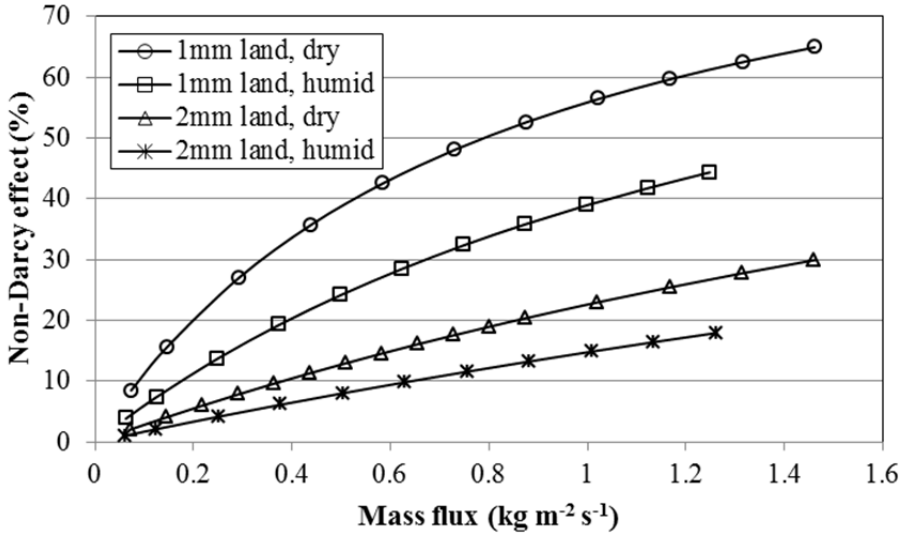

Fig. 5.4 Non-Darcy effect as a function of air mass flux at different land widths and operational conditions

In order to investigate the effects of the operational condition and the width of the land on the non-Darcy effect, the non-Darcy effect in Fig. 5.4 is divided by each other and the ratio of the non-Darcy effect is evaluated. Fig. 5.5 shows the non-Darcy effect ratio at different operational conditions and land widths as a function of the air mass flux. From the result of ratios of the dry condition to the humid one, it is found that the ratios are very close to each other for different land widths. This result may indicate that the effect of water in the GDL on the non-Darcy effect is not changed greatly by the length of the fluid path. The result of non-Darcy effect ratios between the 1 mm and the 2 mm

width lands are also very close to each other for different operational conditions although these ratios gradually decrease as mass flux increases. This result indicates that the effect of the operational conditions on the non-Darcy effect ratio is not large at different land widths and the effect of the non-Darcy effect depends on the quantity of mass flux.

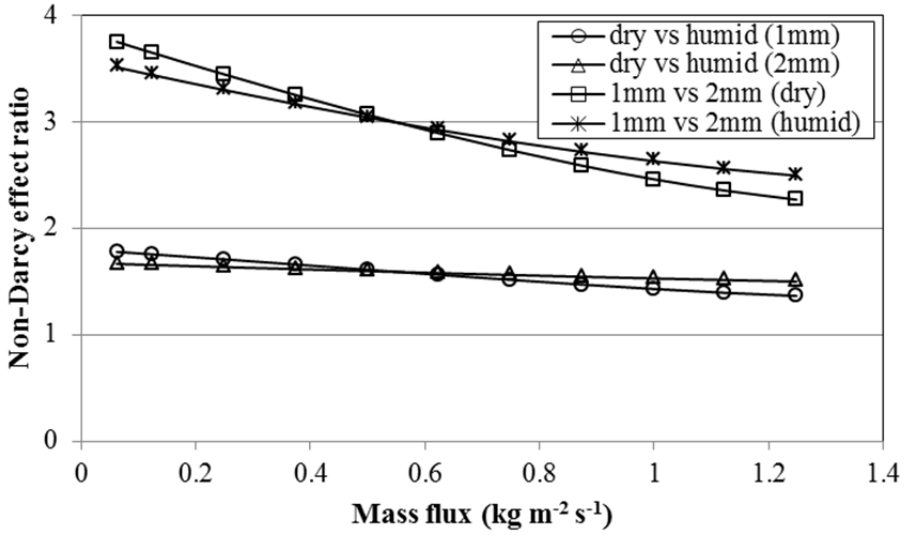

Fig. 5.5 Non-Darcy effect ratio as a function of air mass flux at different land widths and operational conditions

5.2 Cross-flowrate

Fig. 5.6 shows the flowrate in the channel and the flowrate of the cross-flow as a function of valve closure. The channel flowrate decreases with the increase of the valve closure and the flowrate of the cross-flow, on the other hand, increases with the parabolic rule as the valve closure increases. These two flowrates are obviously associated with each other by Eq. (5.5):

$$Q_{cross} = Q_{in} - Q_c \tag{5.5}$$

where Q_{in} is the inlet flowrate, Q_c is the channel flowrate and Q_{cross} is the flowrate of the cross-flow.

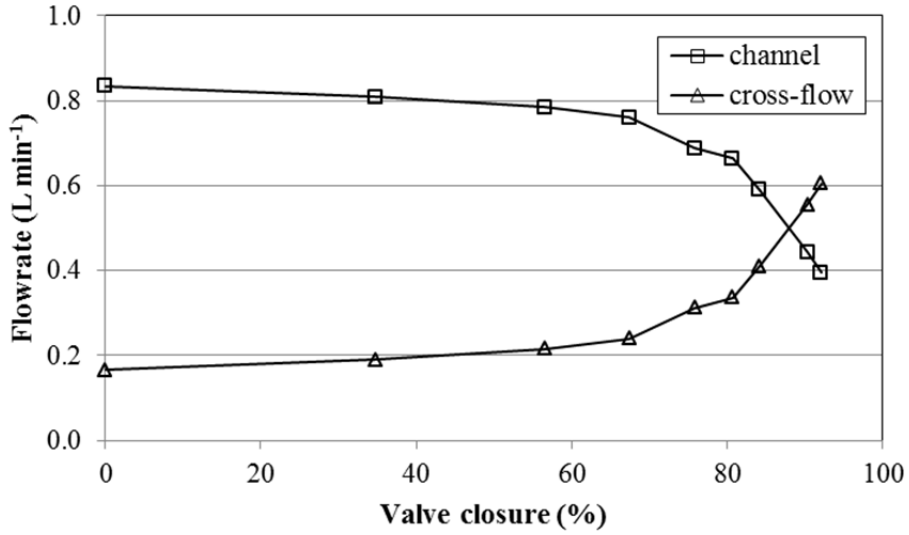

Fig. 5.6 Flowrates of the channel and cross-flow as a function of valve closure (inlet flowrate 1 L min^{-1}, 1 mm width land, dry condition)

Fig. 5.7 presents the relationship between the valve closure and the pressure difference between the adjacent channels. When the valve closure is small, the pressure difference is not so large. However, the pressure difference increases significantly, when the valve closure is beyond approximately 60%. This is because the tip of the flow control valve used in the experiment is a tapered needle shape and the flow channel is not substantially closed until that tip approaches to a certain depth in the channel. From the results of Fig. 5.6 and Fig. 5.7, it is obvious that the valve closure can change both flowrates and the pressure difference and the flow condition of the cross-flow is variable with this valve.

Although Fig. 5.6 already indicates how much cross-flow occurs at specific valve closures, the combination of Fig. 5.6 and Fig. 5.7 can eliminate the effect of the valve closure and the result of the cross-flow can be generalized more.

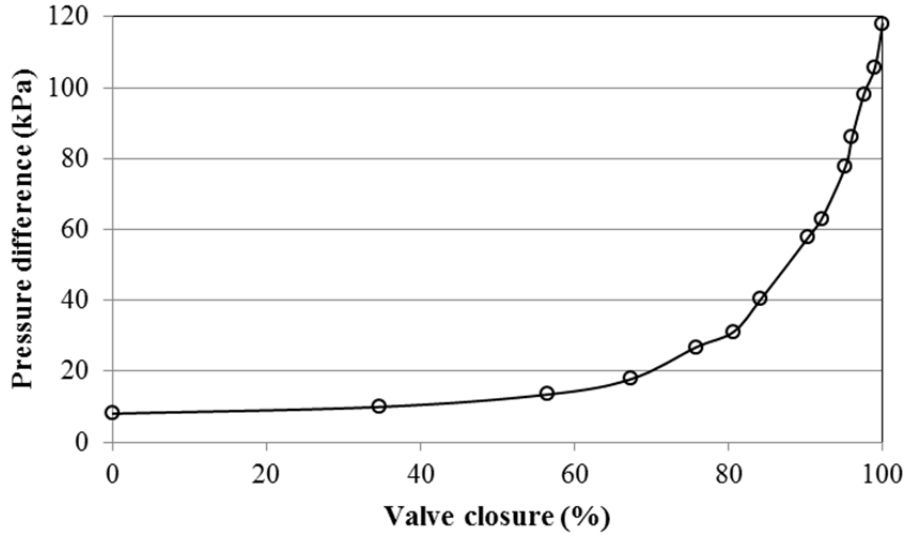

Fig. 5.7 Pressure difference variation as a function of valve closure (inlet flowrate 1 L min^{-1}, 1 mm width land, dry condition)

The flowrate variations of the channel and the cross-flow are presented in Fig. 5.8 as a function of the pressure difference. It is found that the channel flowrate increases linearly and the flowrate of the cross-flow also decreases linearly with the increase of the pressure difference. Since this result excludes the valve closure, it can be said that both the channel flowrate and the flowrate of the cross-flow have a linear relationship for the pressure difference between the adjacent channels.

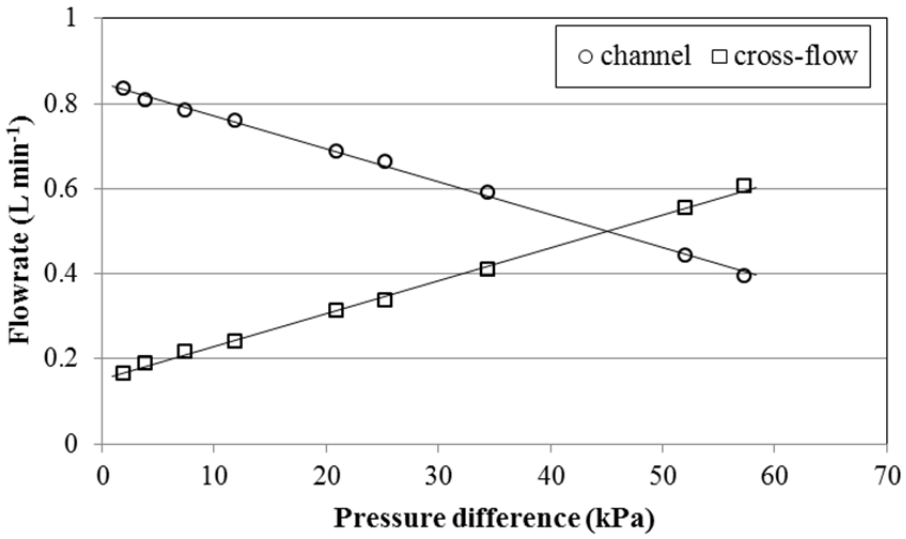

Fig. 5.8 Flowrates of the channel and cross-flow as a function of pressure difference (inlet flowrate 1 L min^{-1}, 1 mm width land, dry condition)

As explained at the experimental methodology in the previous chapter, the cross-flow can be evaluated by the cross-flowrate in Eq. (5.6). Fig. 5.9–Fig. 5.12 show the results of the cross-flowrate as a function of the pressure difference at different inlet flowrates from 0.75 L min^{-1} to 2.0 L min^{-1}, land widths (1 mm, 2 mm) and operational conditions (dry, humid).

$$Q^{*}_{cross} = \frac{Q_{cross}}{Q_{in}} \times 100(\%) \tag{5.6}$$

As shown in these results, the cross-flowrate increases linearly with the increase of the pressure difference for different inlet flowrates and operational conditions because the flowrate of the cross-flow is proportional to the pressure difference as shown in Fig. 5.8. In addition, the pressure difference increases with the increase of the inlet flowrate. It is noted when the cross-flowrates at different inlet flowrates are compared under the same pressure difference conditions, the cross-flowrate decreases with the increase of the inlet

flowrate. This is because the flowrate of the cross-flow does not increase under the same pressure difference and the enhancement of the inlet flowrate results in the decrease of the cross-flowrate.

When results of Fig. 5.9 and Fig. 5.10 are compared in order to evaluate the effect of the operational condition on the cross-flowrate at the land width of 1 mm, it is revealed that the humid condition requires the higher pressure difference than the dry condition in order to obtain the same amount of the cross-flowrate as the dry condition. The comparison of Fig. 5.11 and Fig. 5.12 also presents that the humid condition has a higher pressure difference at the case of the 2 mm width land. These results indicate that excessive water blocks pores in the GDL at the humid condition and this effect becomes more obvious with the increase of the inlet flowrate due to the additional water supply. Thus, it can be said that the cross-flowrate is significantly affected by the operational condition, i.e., humidity.

When Fig. 5.9 is compared with Fig. 5.11 in order to evaluate the effect of the land width at the dry condition, the pressure difference increases considerably with the increase of the land width from 1 mm to 2 mm at the same amount of the cross-flowrate. The same result can be seen by the comparison of Fig. 5.10 with Fig. 5.12. As previously stated, the effective permeability of the 2 mm width land is lower than that of the 1 mm width land. Hence, the pressure difference increases considerably for the 2 mm width land case in order to achieve the same amount of the cross-flowrate as the 1 mm width land case. Therefore, it can be said that the cross-flowrate is also affected by the land width. If the same amount of cross-flowrate is required at different conditions, the pressure difference has to be adjusted at different land width and operational condition.

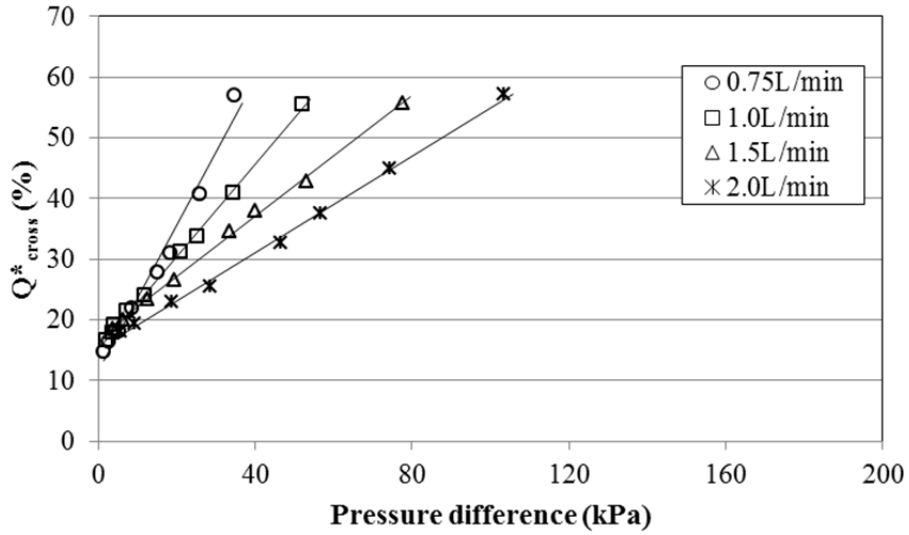

Fig. 5.9 Cross-flowrate at different conditions as a function of pressure difference (1 mm width land, dry condition)

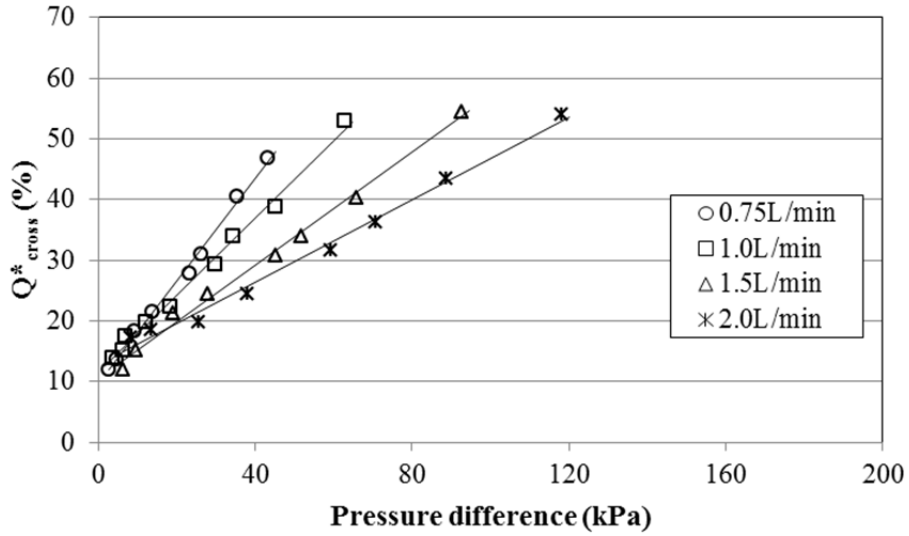

Fig. 5.10 Cross-flowrate at different conditions as a function of pressure difference (1 mm width land, humid condition)

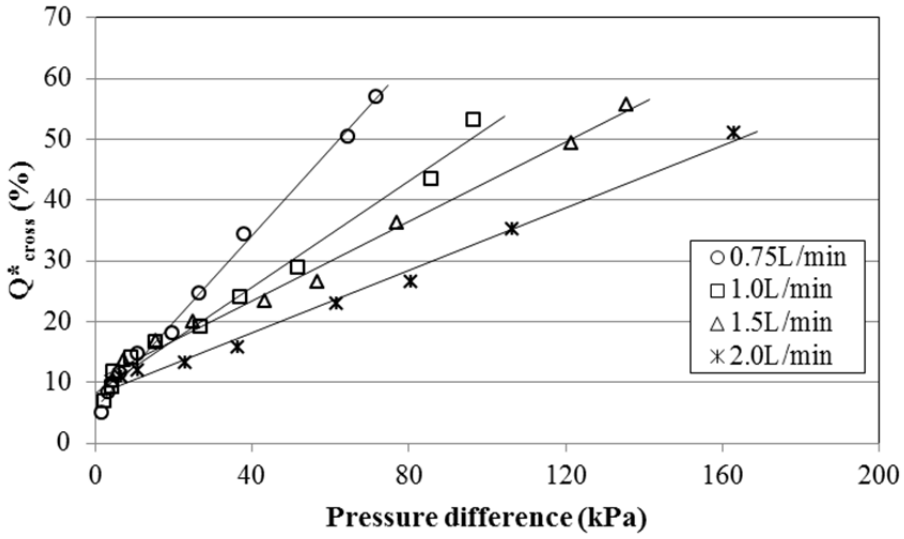

Fig. 5.11 Cross-flowrate at different conditions as a function of pressure difference (2 mm width land, dry condition)

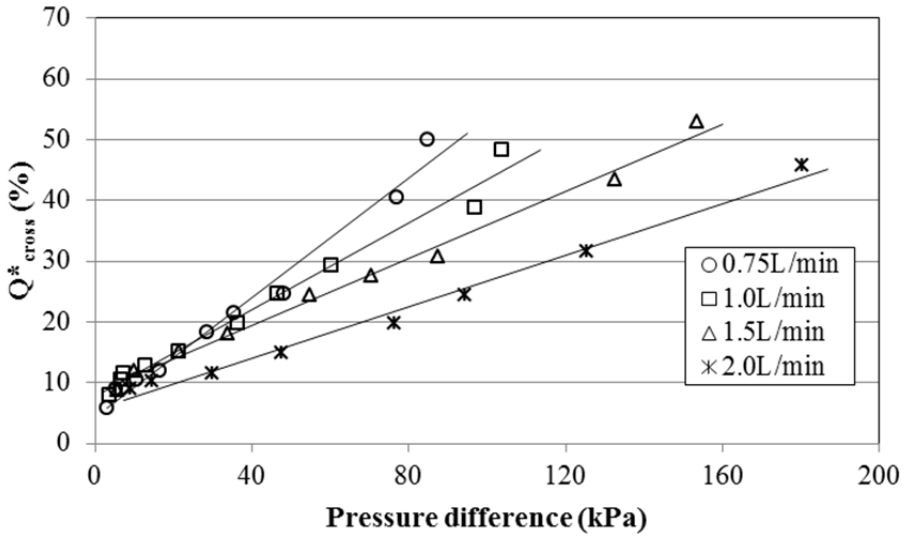

Fig. 5.12 Cross-flowrate at different conditions as a function of pressure difference (2 mm width land, humid condition)

5.3 Dimensional analysis of the cross-flow

The cross-flowrate can be described as a function of the pressure difference between the neighboring channels as explained in the previous section. Although the cross-

flowrate is proportional to the increase of the pressure difference, the gradients of each result at different inlet flowrates, land widths and the operational conditions vary each other. In order to derive a general correlation for the cross-flowrate, the Buckingham Pi theorem (Munson et al 2009) is employed for dimensional analysis. In this theorem, the procedure is described as (Munson et al 2009):

--- If an equation involving k variables is dimensionally homogeneous, it can be reduced to a relationship among k-r independent dimensionless products, where r is the minimum number of reference dimensions required to describe the variables.---

Based on this theorem, firstly, all the variables that are involved in dimensional analysis are listed:

$$Q_{cross} = f\left(k,\ \mu,\ Q_{in},\ L,\ \Delta p\right) \tag{5.7}$$

where Q_{cross} is the flowrate of the cross-flow, k is permeability, μ is dynamic viscosity, Q_{in} is the inlet flowrate, L is the GDL width where air goes through and Δp is the pressure difference between the adjacent channels. Secondary, physical quantities can be described in terms of basic dimensions, i.e., mass, length and time. Thus, six variables in Eq. (5.7) can be reduced to three independent Pi terms with these basic dimensions. Following the method of repeated variables (Munson et al 2009), the cross-flowrate can be finally described as a function of two dimensionless variables:

$$Q^*_{cross} = \emptyset(p^*,\ L^*) \tag{5.8}$$

where Q^*_{cross} is the cross-flowrate, p^* is the dimensionless pressure difference, L^* is the dimensionless land width and

$$Q^*_{cross} = \frac{Q_{cross}}{Q_{in}},\quad p^* = \frac{k^{0.5}L^2}{\mu Q_{in}}\Delta p,\quad L^* = \frac{L}{k^{0.5}} \tag{5.9}$$

The correlation of Eq. (5.8) and Eq. (5.9) is derived by dimensional analysis and in order to evaluate the applicability of this relationship, experimental results presented in Fig. 5.9–Fig. 5.12 are substituted into this equation and the results are shown in Fig. 5.13 and Fig. 5.14 for the 1 mm width land and the 2 mm width land, respectively. The cross-flowrate is proportional to the dimensionless pressure difference and all of the data fall on one line with reasonable scatters at different operational conditions and inlet flowrates. Such a good correlation has demonstrated that a non-dimensional relationship shown in Eq. (5.8) and Eq. (5.9) exists for the cross-flow. In addition, it is interesting to note from Fig. 5.13 and Fig. 5.14 that, when the dimensionless pressure difference equals to zero, the cross-flowrate has a non-zero value. Note the points for the pressure measurement as shown in Fig. 4.2, one can easily understand when the pressure difference is zero, that situation corresponds to the conventional serpentine flow field and this result indicates that there exists under-land cross-flow in a serpentine flow field.

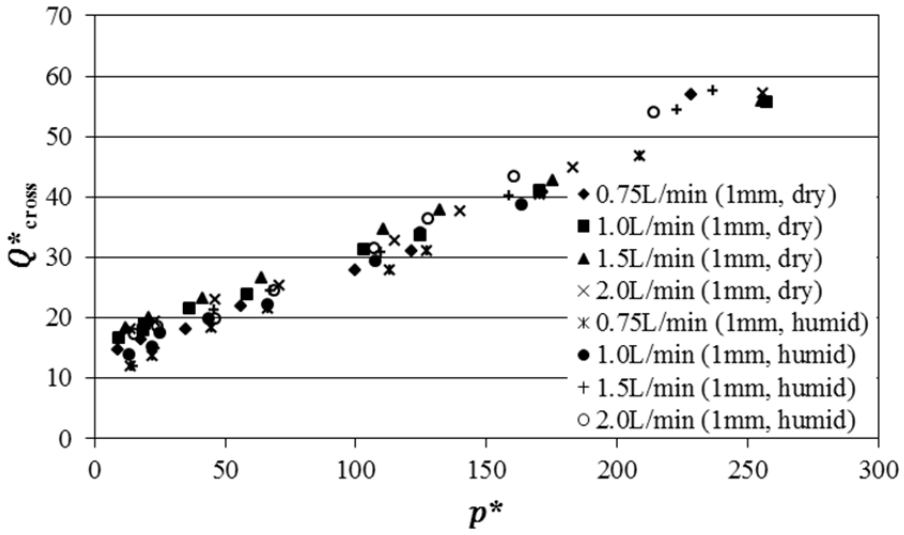

Fig. 5.13 Empirical correlation of the cross-flowrate (1 mm width land)

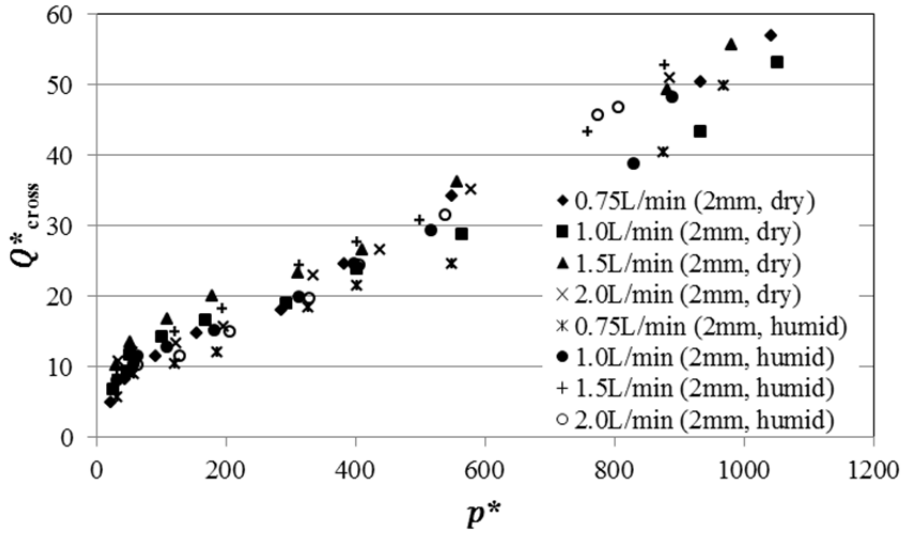

Fig. 5.14 Empirical correlation of the cross-flowrate (2 mm width land)

5.4 Summary

A unique experimental fixture is developed and the effective permeability and the under-land cross-flow are directly measured in the actual fuel cell. Experimental results show that the effective permeability is affected by the inertial effect in the GDL and varies with the land width and the humidification condition. The non-Darcy effect is also evaluated in order to investigate the inertial effect in the GDL and the results show that the inertial effect becomes significant at the large mass flux condition.

The cross-flow is measured with varying the valve closure and then, results are converted into the cross-flowrate as a function of the pressure difference at different operational and humid conditions. It is shown that the cross-flowrate is proportional to the increase of pressure difference between the adjacent channels. By applying dimensional analysis method, the cross-flowarate is expressed as a function of two dimensionless parameters. The derived non-dimensional correlation is applied to the

experimental data and shows the good agreement with them. Thus, it is revealed that there exists a non-dimensional relationship for the cross-flow.

CHAPTER 6

EFFECT OF UNDER-LAND CROSS-FLOW ON PEM FUEL CELL PERFORMANCE

6.1 Current density

The pressure difference between the adjacent channels is measured as a function of the valve closure in order to define specific valve closure points and the result is shown in Fig. 6.1 at different inlet flowrates. The specific points of the valve closure are chosen between the fully opened to the fully closed conditions and marked as the zero, low, medium and full closure conditions in Fig. 6.1. When the valve closure is less than approximately 60%, the pressure difference does not change significantly. However, with the further increase of the valve closure, the pressure difference increases considerably with a non-linear distribution.

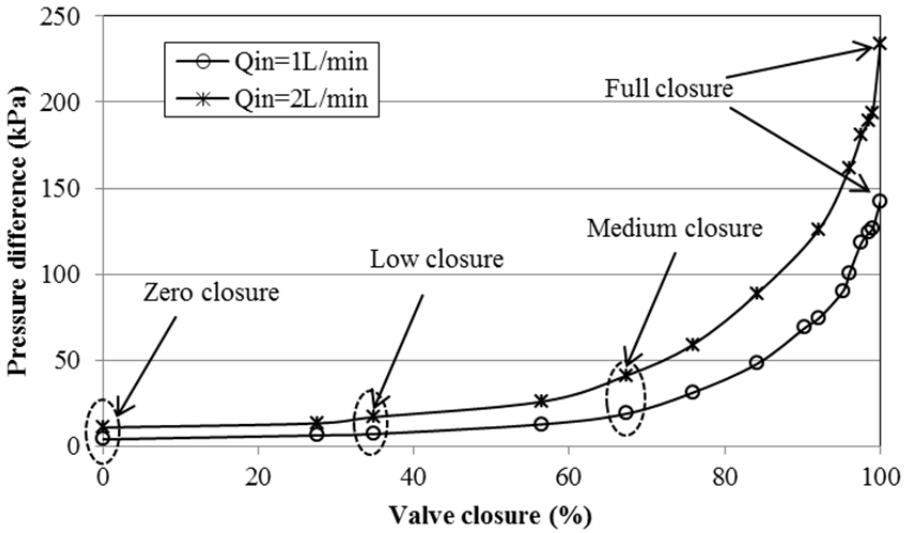

Fig. 6.1 Pressure difference variation as a function of valve closure

Fig. 6.2 shows the polarization curves with varying the valve closure condition at the inlet flowrate of 1.0 L min^{-1}. The overall current density gradually increases with the increase of the valve closure from the zero to the full closure conditions. Usually a fuel cell is operated around the voltage of 0.4–0.6V and there is a significant current density enhancement from the zero to the low closures and from the medium to the full closures in this voltage range. In addition, the current density at the full closure condition shows the significant increase in comparison with other conditions. This is attributed to the fact that the full closure condition has the highest pressure difference between the neighboring channels and the additional reactant is supplied to the GDL under the land area compared with other conditions.

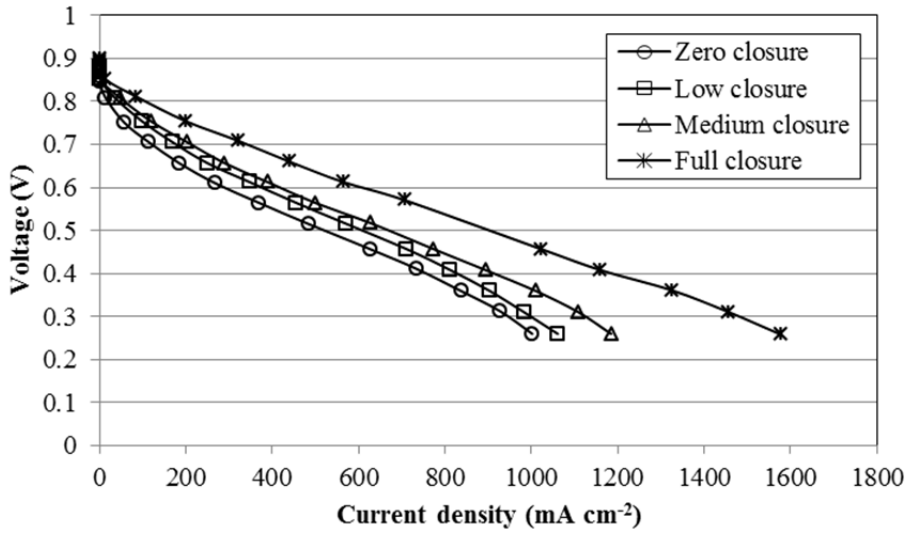

Fig. 6.2 Polarization curves for different valve closure (Q_{in}=1.0 L min^{-1})

Fig. 6.3 presents the polarization curves for the cathode inlet flowrate of 2.0 L min^{-1}. Although the cell performance increases with the increase of the valve closure, the performance increment from the zero to the medium closures is not so obvious compared

with the previous case of the inlet flowrate of 1.0 L min^{-1}. This is because when the inlet flowrate is increased, the additional reactant is supplied to the GDL both under the channel and under the land and the electrochemical reaction becomes more active even at the condition of the zero closure. Nevertheless, the large increase of the performance is still achievable at the high current density region. Generally, the mass transport loss occurs at the higher current density region due to the lack of the reactant, especially at the GDL under the land area. However, with the increase of the valve closure, the pressure difference is enhanced and this pressure difference can supply the additional reactant to that area. Thus, the reaction under the land is promoted and the performance at the high current density region continues to increase. From these results, it can be said that the fuel cell performance can be changed by the valve closure which controls the pressure difference between the neighboring channels.

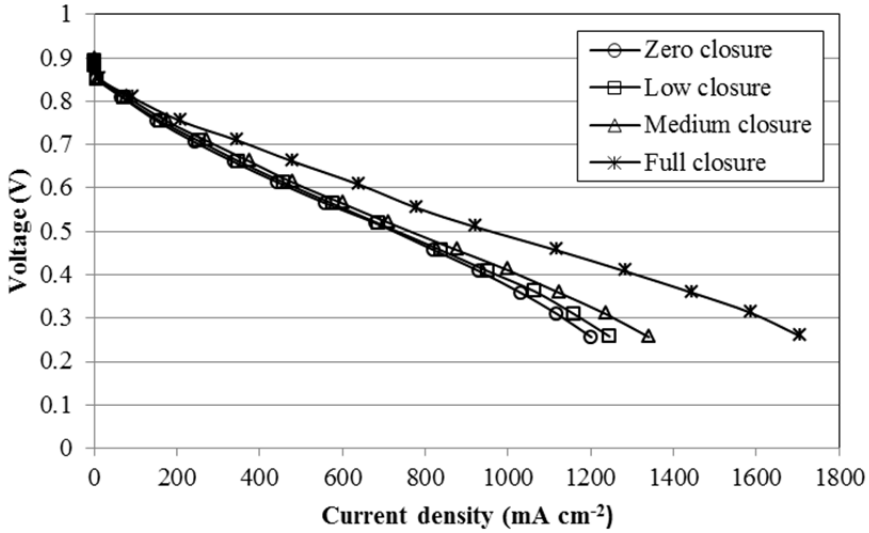

Fig. 6.3 Polarization curves for different valve closure (Q_{in}=2.0 L min^{-1})

Although the fuel cell performance is basically evaluated by the flow field with the 1 mm width land in this chapter, the polarization curves by the flow field with the 2 mm width land are presented in Fig. 6.4 and Fig. 6.5 in order to show the land width effect on the fuel cell performance. As shown in these results, although the fuel cell performance increases with the increase of the valve closure same the cases of the 1 mm width land, overall performances for both the inlet flowrate of 1.0 L min^{-1} and 2.0 L min^{-1} are lower than those for the cases of the 1 mm width land. As mentioned by Tehlar et al. (Tehlar et al 2010), when the land becomes wider, the fuel cell performance becomes lower due to the decrease of the reactant under the land; thus, the result for the 2 mm width land shows the lower performance.

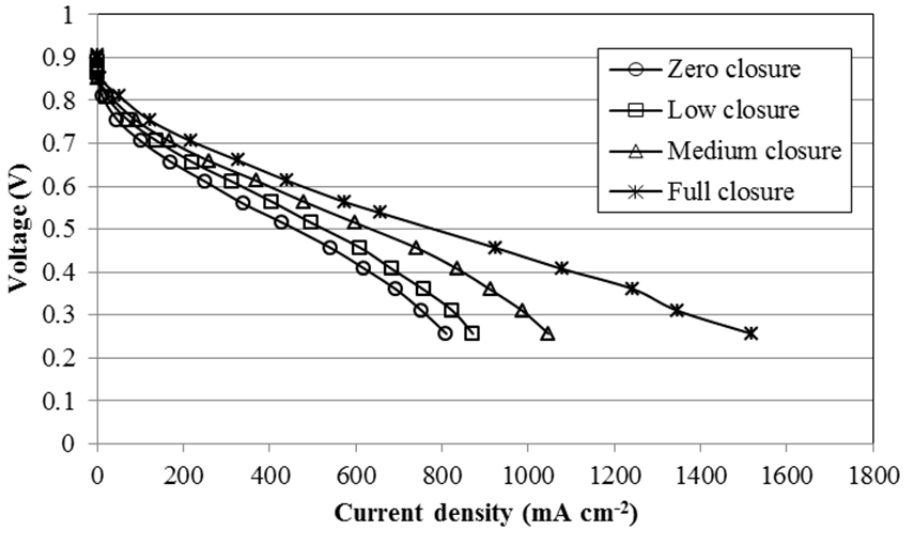

Fig. 6.4 Polarization curves for different valve closure (Q_{in}=1.0 L min^{-1}, 2 mm width land)

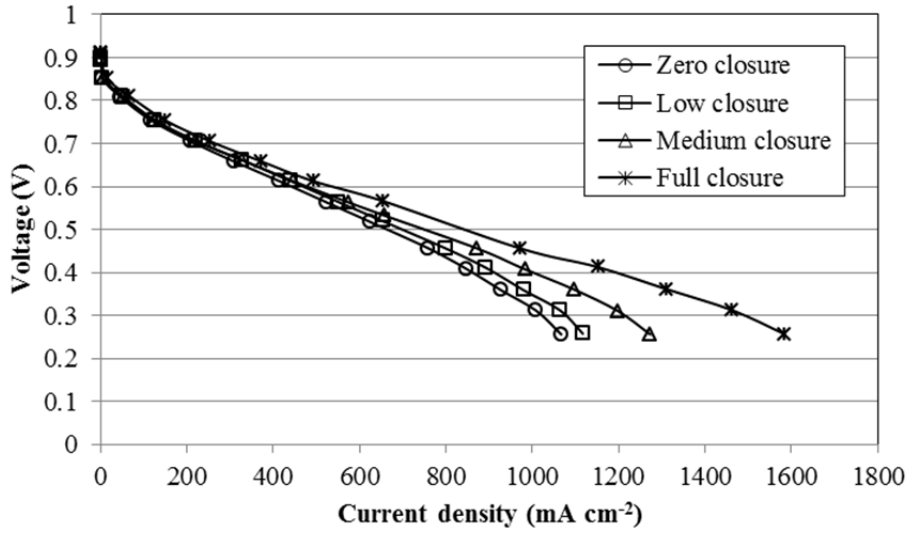

Fig. 6.5 Polarization curves for different valve closure (Q_{in}=2.0 L min^{-1}, 2 mm width land)

Fig. 6.6 provides the result of the cross-flowrate at the inlet flowrate of 1.0 L min^{-1} and 2.0 L min^{-1}. The pressure difference is controlled by the valve closure and Fig. 6.6 shows that the cross-flowrate increases with the increase of the pressure difference. Thus, it can be said that the pressure difference increases the under-land cross-flow and the enhanced cross-flow contributes to increase the fuel cell performance. Besides, it is revealed that some amount of the inlet flow becomes the cross-flow at the zero closure condition and existence of the cross-flow even if the pressure difference is not so large. Since the measurable flowrate of the flow meter used in this experiment is limited, the cross-flowrate cannot be measured at the valve closure range shown in Fig. 6.1; however, this result indicates that the performance enhancement from the zero to the full closure conditions shown by the polarization curves in Fig. 6.2 and Fig. 6.3 is attributed to the under-land cross-flow effect.

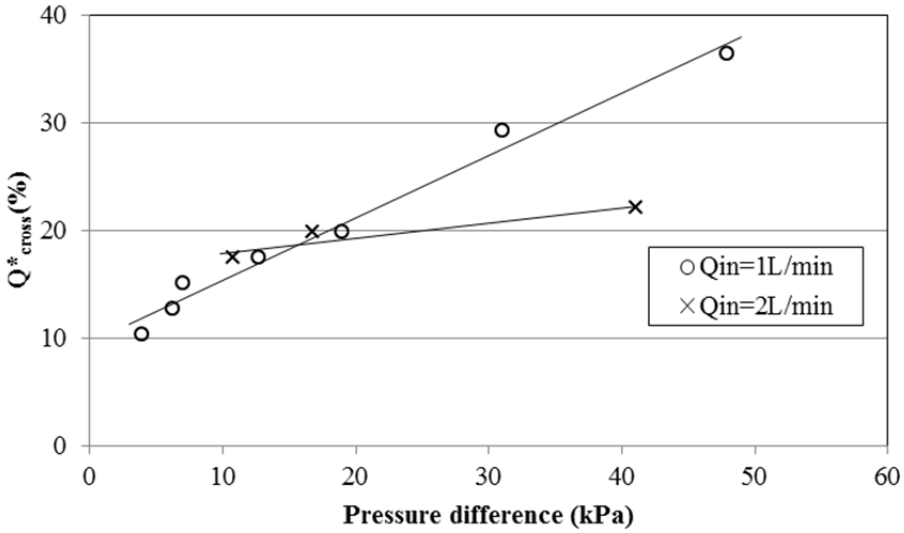

Fig. 6.6 Cross-flowrate measurement as a function of the pressure difference

Since Fig. 6.1 indicates that the valve closure is expressed as a pressure difference, the polarization curve can be converted into the relationship between the current density and the pressure difference at each voltage. Fig. 6.7 shows the current density variation as a function of pressure difference at the inlet flowrate of 1.0 L min^{-1}. The pressure difference increases from the zero to the full closures and the lowest point (leftmost) of the pressure difference corresponds to the zero closure condition and the highest one (rightmost) is for the full closure condition. It is obvious that the current density increases with the decrease of the output voltage. In addition, with the increase of the pressure difference, the current density also increases due to the enhancement of the cross-flow. Furthermore, although the current density at the full closure condition shows the highest performance, the pressure difference is also the highest at that condition. It is remarkable that the significant increment of the current density is obtained from the zero to the low closure conditions with a small increase of the pressure difference. Thus, it can be said

that the small increase of the pressure difference from the zero to the low closure conditions is more efficient in order to increase the current density than the large increment of the pressure difference from the zero to the full closure conditions.

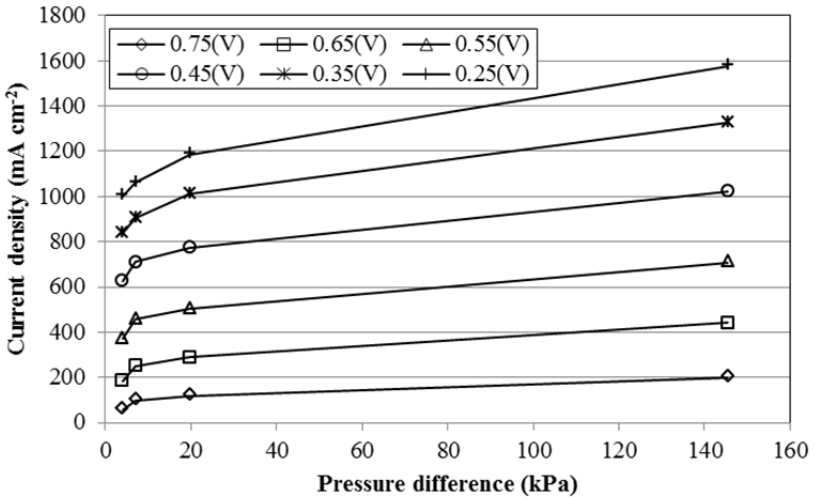

Fig. 6.7 Current density variation as a function of pressure difference at different voltages (Q_{in}=1.0 L min^{-1})

Fig. 6.8 presents the result of the current density variation as a function of the cross-flowrate at the inlet flowrate of 1.0 L min^{-1}. Again, the lowest point (leftmost) of the cross-flowrate corresponds to the zero closure condition and the highest one (rightmost) is equivalent to the full closure condition. The current density increases with the increase of the cross-flowrate at each output voltage and this result indicates the effectiveness of the cross-flow on the fuel cell performance improvement. In addition, about 70% of the maximum current density is attained by 20% of the cross-flowrate. Thus, it can be said that the fuel cell performance increases significantly and efficiently until some amount of the cross-flowrate and then, the increment gradually decreases although the total current density continues to increase.

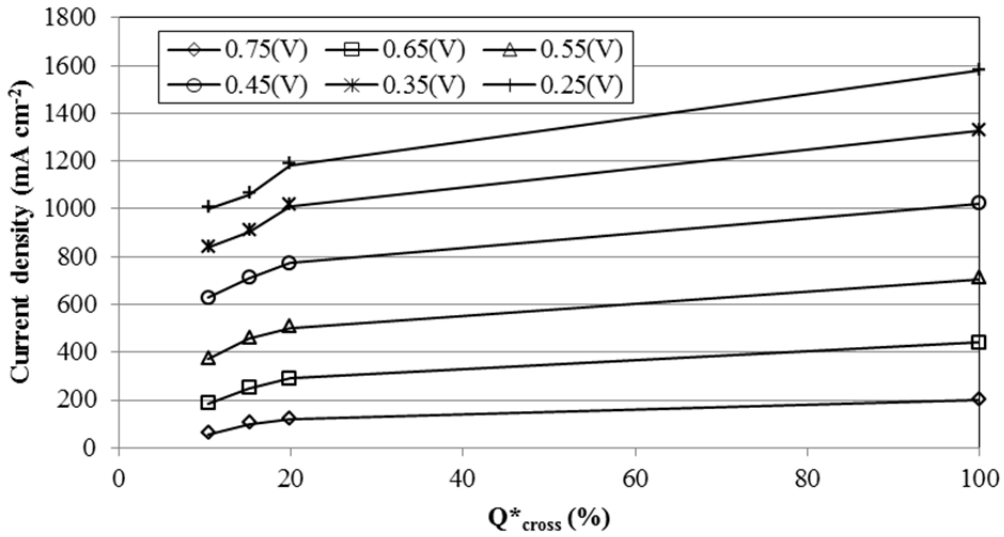

Fig. 6.8 Current density variation as a function of cross-flowrate at different voltages (Q_{in}=1.0 L min^{-1})

Fig. 6.9 gives the current density variation as a function of pressure difference at the inlet flowrate of 2.0 L min^{-1}. The current density increases with the increase of the pressure difference same as the results of the inlet flowrate of 1.0 L min^{-1}. It is noted that although the current density increases from the zero to the low closure conditions at low voltages, the increment is not obvious at high voltages. This result indicates that since much air is provided to the GDL under the land area and the channel area at this flowrate, the performance enhancement by the pressure difference is not significant at the high voltage. Nevertheless, it is shown that the increase of the pressure difference is still effective at the low voltage. Fig. 6.10 presents the result of the current density variation as a function of the cross-flowrate at the inlet flowrate of 2.0 L min^{-1}. The current density does not increase so much from the zero to the medium closure conditions at the high voltage since much air is already supplied to the GDL at this condition. However, the

current density increases with the increase of the cross-flowrate at the low voltage due to the enhancement of the under-land reaction by the cross-flow.

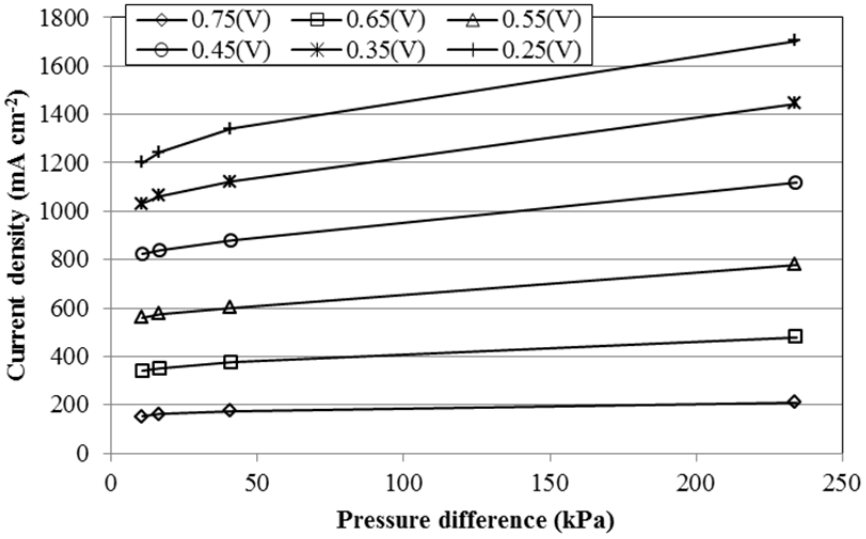

Fig. 6.9 Current density variation as a function of pressure difference at different voltages (Q_{in}=2.0 L min^{-1})

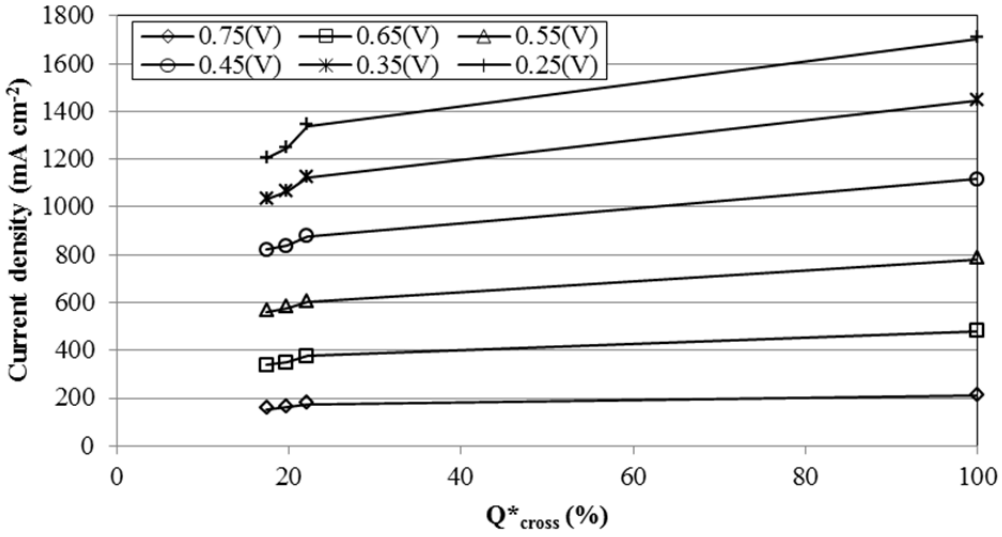

Fig. 6.10 Current density variation as a function of cross-flowrate at different voltages (Q_{in}=2.0 L min^{-1})

6.2 Power density

Fig. 6.11 provides the result of the power density for different valve closure conditions at the inlet flowrate of 1.0 L min^{-1}. The difference among each power density increases with the increase of the current density although that difference is not obvious at the current densities smaller than approximately 200 mA cm^{-2}. In addition, with the increase of the valve closure, the difference of the power density also increases due to the enhancement of the current density by the cross-flow.

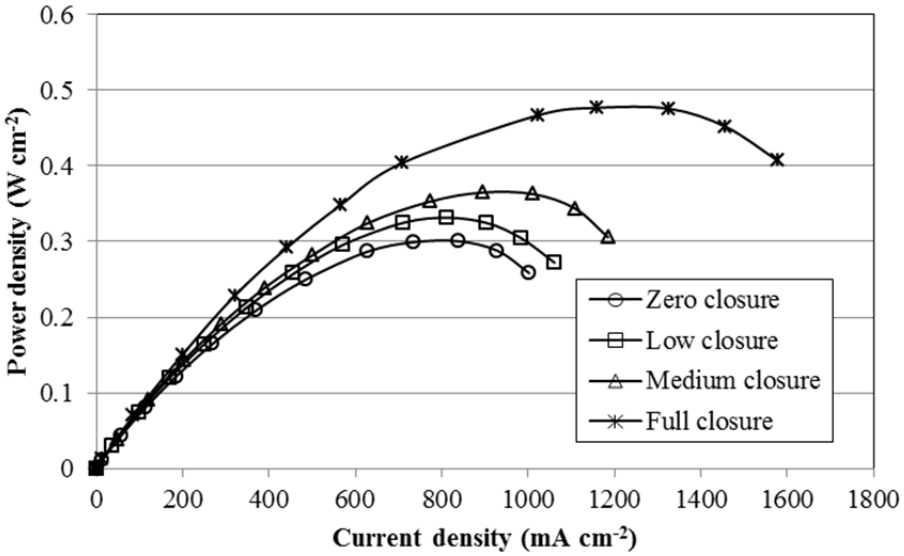

Fig. 6.11 Power density variation for different valve closure (Q_{in}=1.0 L min^{-1})

Although the fuel cell performance increases with the increase of the valve closure which can be expressed by the pressure difference, the additional pumping power for the reactant supply is required in order to keep the constant flowrate at the increased pressure difference condition. Thus, the effect of the pumping power should be considered in

order to precisely evaluate the performance enhancement by the cross-flow. For the evaluation of the pumping power effect, the net power density (Bachman et al 2012), which can be calculated by subtracting the pumping power from the power density, is introduced. The pumping power (P_{pump}) is calculated by Eq. (6.1):

$$P_{pump} = \frac{Q_{in} P_{in}}{\eta} \text{ (W)} \tag{6.1}$$

where inlet flowrate (Q_{in}) and inlet pressure (P_{in}) are measured by the test station and the pumping efficiency (η) is assumed to 85%. Fig. 6.12 shows the pumping power variation as a function of the inlet flowrate. This result indicates that the pumping power increases almost linearly with the increase of the inlet flowrate. In addition, the pumping power for the full closure condition is significantly high compared with other valve closure cases. These pumping power differences are basically originated from the characteristics of the experimental setup used in the current study. The zero, the low and the medium closure conditions are considered as the variations of a serpentine flow field and the full closure condition is regarded as a kind of an interdigitated flow field. Although the flow channel used in this experiment is a single flow path and its length is not so long, a regular serpentine flow field has a flow path with multiple U-turns and the total channel length becomes very long and requires the higher pumping power compared with the current experiment. On the other hand, the effect of the configuration difference is small between the current experimental setup and a regular interdigitated flow field because the channel length does not change significantly for them. Since the nature of the flow fields is different among these four closure conditions, the net power density is compared for the serpentine flow field conditions (zero, low and medium closures) in the further analysis and the effect of the cross-flow is evaluated for these three conditions.

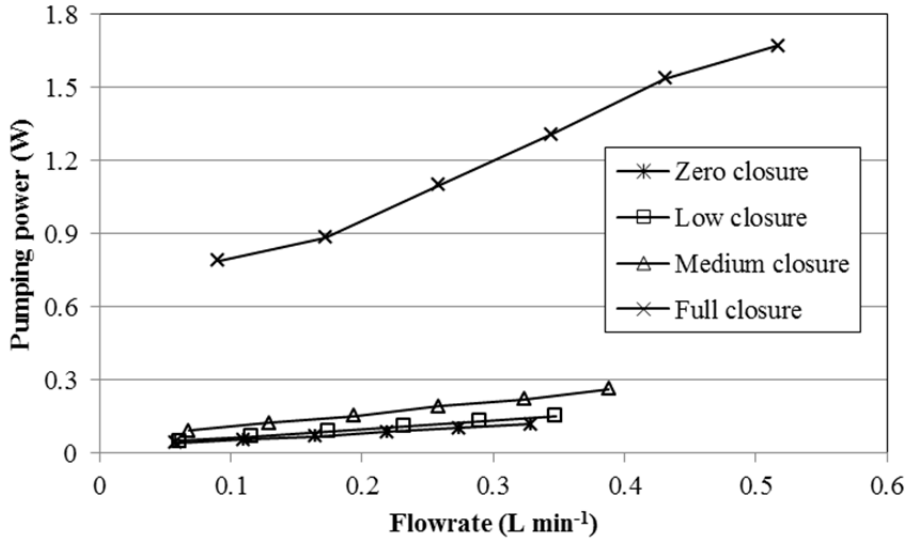

Fig. 6.12 Pumping power estimation as a function of inlet flowrate

Fig. 6.13 shows the net power density variation at the different stoichiometry for different valve closures. The net power density gradually increases from the zero to the medium closure conditions when the current density is larger than approximately 800 mA cm^{-2}. However, except that current density range, the low closure condition shows the highest performance and the net power density at the medium closure condition becomes the lowest among them. In addition, it is revealed that the net power density of the medium closure condition decreases significantly at the low current density region when the stoichiometry changes from λ=2 to λ=4. This is attributed to the fact that the fuel cell does not generate large output power at the low current density although the medium closure condition requires the higher pumping power compared with the zero and the low closure conditions. Thus, the effect of the excessive pumping power becomes obvious with the increase of the stoichiometry.

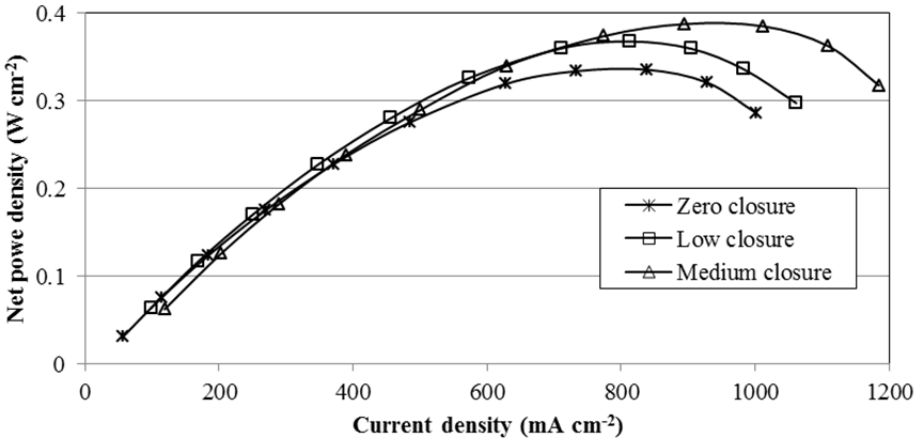

(a)

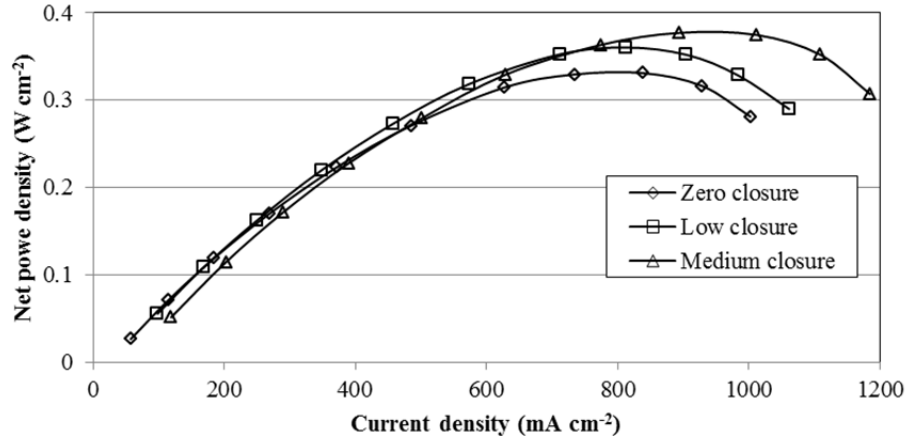

(b)

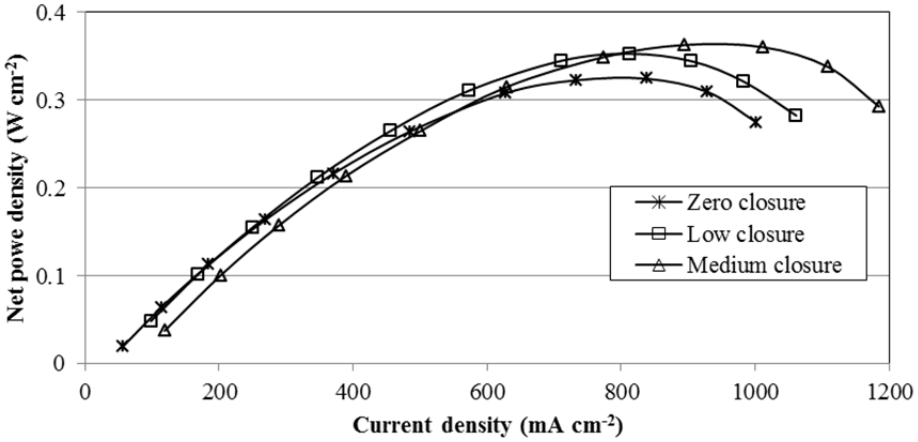

(c)

Fig. 6.13 Net power density at different stoichiometry λ (a) λ=2, (b) λ=3, (c) λ=4

From the result of Fig. 6.13, it can be said that the larger valve closure does not always show the higher performance and the pumping power also significantly affects the net power density. Furthermore, it cannot be decided either the low closure or the medium closure has a better performance because their performances depend on the current density range. Since fuel cells are generally operated around the voltage of 0.5V, the net power density is evaluated around that voltage and the performance enhancement by the cross-flow is investigated. Another criterion, the net power density ratio, which is defined as the ratio of the net power density of the low/medium closure to the zero closure is introduced for the evaluation of the net power density. The resultant net power density ratios are shown in Fig. 6.14 and Fig. 6.15 as a function of the pressure difference and the cross-flowrate, respectively. As shown in Fig. 6.14, the net power density ratio increases with the increase of the pressure difference due to the reaction enhancement by the cross-flow. In addition, it is revealed that the net power density ratio is the highest at 0.6V and the lowest at 0.4V because the peak output power is obtained around 0.4V for this experiment and the increment of the output power becomes small near the peak voltage. Furthermore, it is remarkable that the significant increase of the net power density ratio is found from the zero closure condition (leftmost point) to the low closure condition (middle point) compared with the increment from the low closure condition to the medium closure condition (rightmost point) although this performance enhancement gradually decreases with the decrease of the voltage. Thus, it can be said that the small increase of the pressure difference is more efficient than the large increment in order to enhance the fuel cell performance. Fig. 6.14(c) shows the net power density ratio at the

stoichiometry of 4. Although the performance still increases from the zero closure to the low closure conditions, the increment from the low closure to the medium closure becomes very small at the output voltage of 0.6V. This result may suggest that enough air is already supplied to the GDL both under the channel area and the land area in this condition and a further increase of the cross-flow by the pressure difference does not contribute to enhance the net power density. Thus, it can be said that the performance increment by the cross-flow is more effective at the low closure condition under the middle range of the output voltage and the moderate stoichiometry condition. Fig. 6.15 also indicates the enhancement of the fuel cell performance by the increment of the cross-flowrate. The net power density ratio increases significantly from the zero closure to the low closure conditions and this increment is more obvious especially at the voltage of 0.6V and 0.5V under the stoichiometry of 2 and 3. On the other hand, the increment of the net power density ratio from the low closure to the medium closure at the stoichiometry of 4 becomes very small at 0.6V and 0.5V due to the enough air existence. Thus, from the point of cross-flow evaluation, it can be said that the fuel cell performance can be efficiently enhanced by the additional small increase of the pressure difference which induces the some cross-flow enhancement.

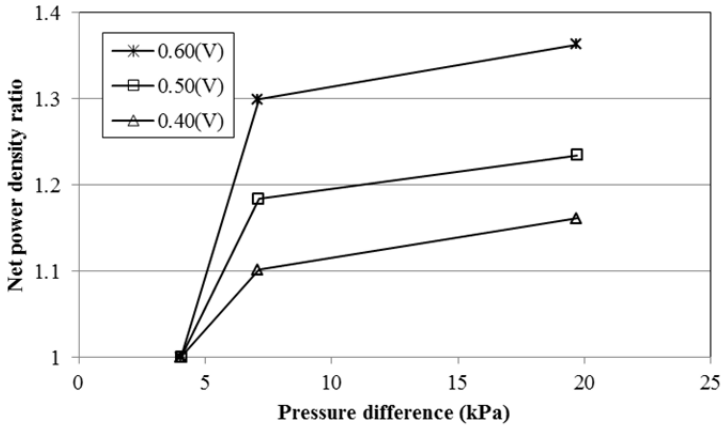

(a)

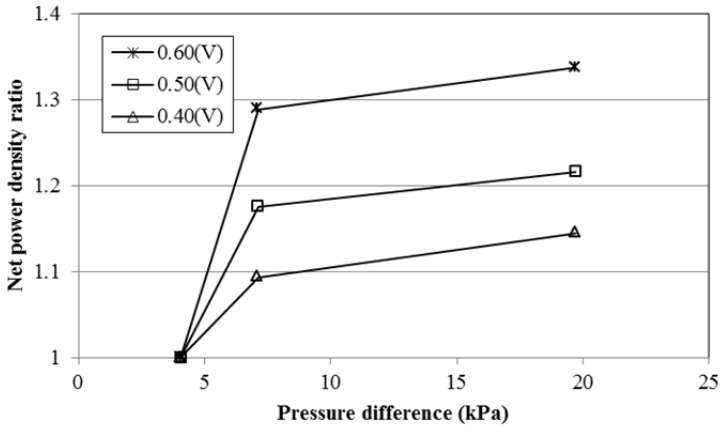

(b)

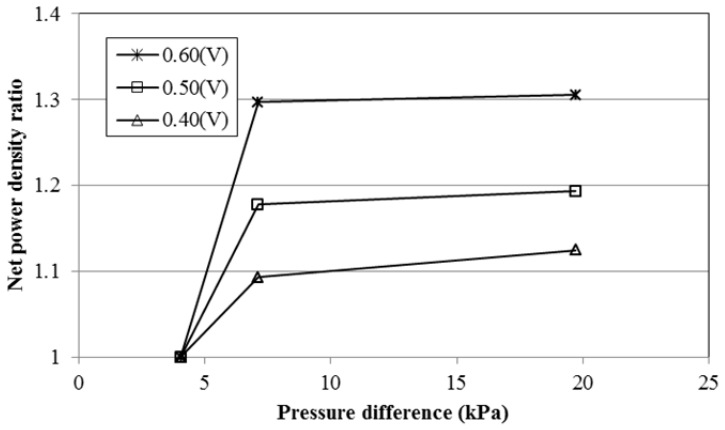

(c)

Fig. 6.14 Net power density ratio as a function of pressure difference
(a) λ=2, (b) λ=3, (c) λ=4

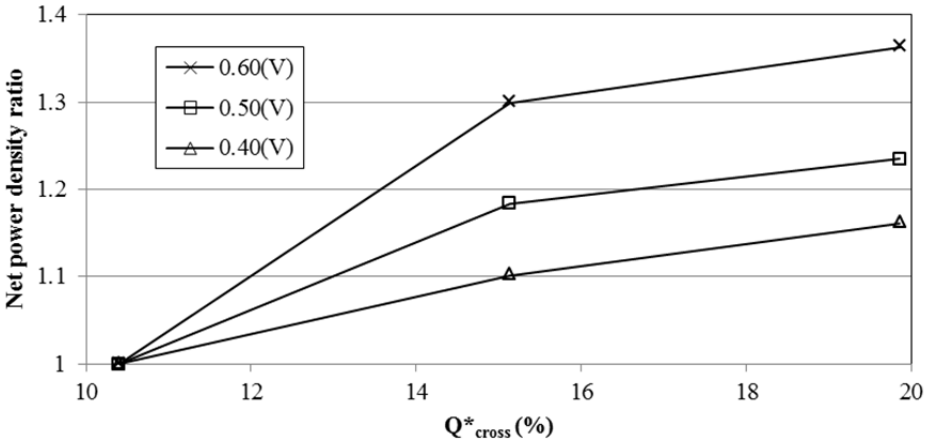

(a)

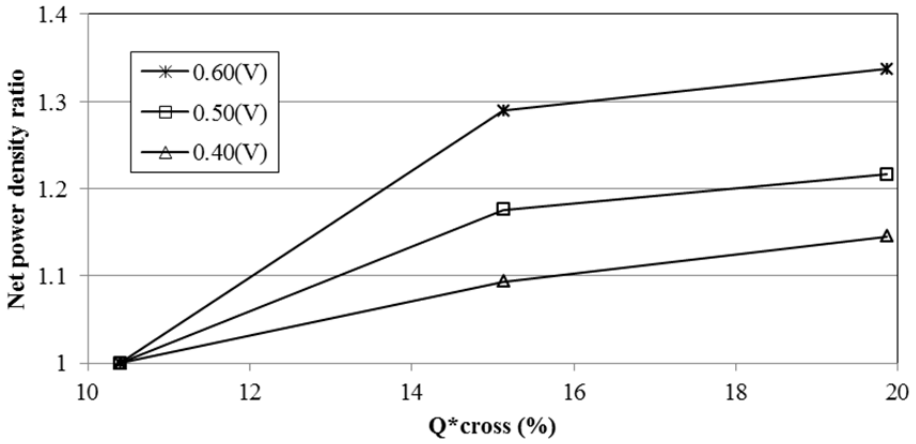

(b)

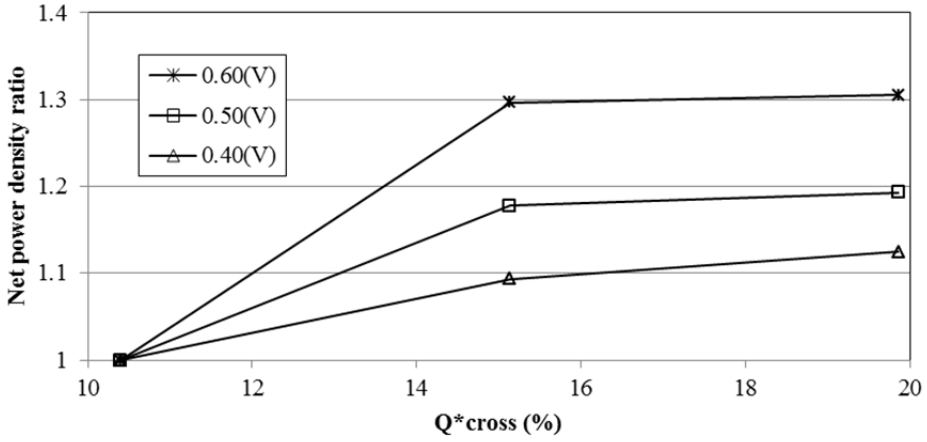

(c)

Fig. 6.15 Net power density ratio as a function of cross-flowrate
(a) λ=2, (b) λ=3, (c) λ=4

6.3 Summary

The current density and the power density are evaluated with varying the pressure difference between the adjacent channels at the cathode flow field. The experimental results show that the current density gradually increases with the increase of the valve closure. The experimental result indicates that the small increase of the pressure difference from the zero closure to the low closure conditions is more efficient in order to enhance the current density than the large increment from the zero to the full closure conditions. It is also shown that the power density increases with the increase of the valve closure due to the enhancement of the current density by the cross-flow. The net power density ratio shows that the fuel cell performance increases significantly from the zero to the low closure conditions. This result indicates that the cross-flow efficiently increases the fuel cell performance with the additional small increment of the pressure difference and the excessive stoichiometry, on the contrary, decreases the fuel cell efficiency.

CHAPTER 7

MODELING METHODOLOGY

7.1 Modeling geometry

An in-house three-dimensional PEM fuel cell model is developed with Fortran language in order to investigate the flow field, the oxygen distribution and the local current density distribution around the land area. Since the hydrogen oxidation reaction (HOR) at the anode side is faster than the oxygen reduction reaction (ORR) at the cathode side, the overall fuel cell performance is generally dominated by the cathode side reaction (O'Hayre et al 2009); thus, only the cathode side is modeled in this work.

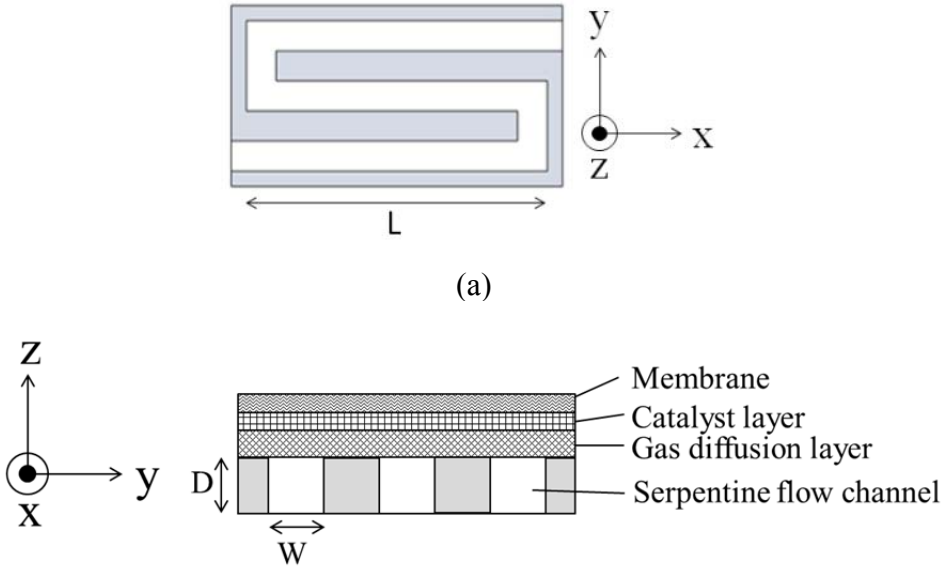

Fig. 7.1 Modeling geometry (a) Serpentine flow field (b) Cross sectional view

The modeling geometry is composed of a gas diffusion layer, a catalyst layer, a membrane and a flow channel as shown in Fig. 7.1. The channel width (W) and depth (D) are 1 mm and 1 mm, respectively and the land width is set to 1 mm. In addition, two different channel lengths (L) of 0.01 m and 0.06 m are compared at the simulation in order to evaluate the channel length effect.

7.2 Governing equations

The simulation procedure is based on the SIMPLE algorithm developed by Patankar (Patankar 1980) and firstly, three momentum equations corresponding to x-, y- and z-coordinates are solved by coupling the continuity equation. After obtaining the velocity field, a species transport equation and two potential equations are coupled and solved. In addition, layers of MEA i.e., a GDL, a catalyst layer and a membrane are assumed to be continuous at the interface between any two layers; thus, no specific boundary conditions are required there and this treatment makes the simulation model simple. Governing equations are similar to those used by Zhou and Liu (Zhou and Liu 2006) and as follows:

Continuity equation:

$$\nabla \cdot \rho \boldsymbol{V} = \begin{cases} 0 & \text{Channel, GDL, membrane} \\ S_k & \text{Catalyst layer} \end{cases} \tag{7.1}$$

where S_k is a source term and defined in the species transport equation.

Momentum equation:

$$\boldsymbol{V} \cdot (\nabla \boldsymbol{V}) = -\nabla p + \begin{cases} \mu \Delta \boldsymbol{V} & \text{Channel} \\ r^{(2)} \mu \Delta \boldsymbol{V} - \varepsilon \dfrac{\mu}{k_p} \boldsymbol{V} & \text{GDL, Catalyst layer, membrane} \end{cases} \tag{7.2}$$

where $r^{(2)}$ is a porous media correction factor derived by Dagan (Dagan 1979).

Species transport equation:

$$\rho \cdot (\nabla X_k) = \varepsilon \rho D_{eff} \Delta X_k + \begin{cases} 0 & \text{Channel and GDL} \\ \varepsilon \rho S_k & \text{Catalyst layer} \end{cases} \tag{7.3}$$

where $S_k = j/4Fc$ and j is calculated from the following Butler-Volmer equation:

$$j = a i_0^{ref} \left(\frac{X_{O_2}}{X_{O_{2,ref}}} \right) \left[exp\left(\frac{\alpha_a F}{RT} \eta \right) - exp\left(-\frac{\alpha_c F}{RT} \eta \right) \right] \tag{7.4}$$

Membrane phase potential equation:

$$\nabla \cdot (\sigma_m \nabla \Phi_m) = \begin{cases} j & \text{Catalyst layer} \\ 0 & \text{Membrane} \end{cases} \tag{7.5}$$

Solid phase potential equation:

$$\nabla \cdot (\sigma_s \nabla \Phi_s) = \begin{cases} -j & \text{Catalyst layer} \\ 0 & \text{GDL and Land} \end{cases} \tag{7.6}$$

The overpotential within the catalyst layer at the cathode side is calculated by the following relationship (Zhou and Liu 2006):

$$\eta = \Phi_s - \Phi_m - E_0 \tag{7.7}$$

where E_o is open circuit potential. Modeling assumptions used in this model are as follows:

- The flow is laminar everywhere.
- Steady state and single phase case are considered.
- The gas is incompressible and ideal.

7.3 Modeling parameters and boundary conditions

The Reynolds number of 148 is applied for the channel inlet condition. At the outlet, pressure outlet boundary method (Dutta et al 2001, Hu and Fan 2007) is applied. Since

the dependent variables of the momentum and species transport equations are assumed to be continuous at the interface between different layers such as GDL/catalyst layer and catalyst layer/membrane, specific boundary conditions are not put at these interfaces. For the interface between the fluid domain and the solid domain, flux of species is set to zero and no-slip condition is applied. The boundary condition for the membrane phase potential equation is zero flux along the boundaries except the boundary where the membrane contacts with the anode catalyst layer. At this boundary, potential is set to zero. The boundary condition for the solid phase potential is also set to zero flux along boundaries except the interface with the graphite plate. At this surface, the solid potential is assumed to be equal to the cell voltage due to the significantly high electric conductivity of the graphite plate. The major parameters used for the modeling are shown in Table 7.1.

Table 7.1 Major modeling parameters

Gas channel length L	1.0×10^{-2} m or 6.0×10^{-2} m
Gas channel depth D	1.0×10^{-3} m
Gas channel width W	1.0×10^{-3} m
Gas diffuser thickness	2.0×10^{-4} m
Catalyst layer thickness	1.0×10^{-5} m
Membrane thickness	3.0×10^{-5} m
Gas diffuser porosity ε	0.5
Catalyst layer porosity ε	0.3
Catalyst layer permeability k	1.76×10^{-13} m^2
Membrane permeability k	1.58×10^{-18} m^2
Ionic conductivity σ	4.2 S m^{-1}
Electrical conductivity σ	145.0 S m^{-1}
Reference exchange current	1.0×10^{3} A m^{-3}

density times area ai_o^{ref}	
Anodic transfer coefficient α_a	0.0
Cathodic transfer coefficient α_c	1.0
Air inlet pressure	1.0 atm
Air inlet velocity	3.0 m s^{-1}
Air inlet temperature	70^{o}C
Electrical conductivity of land	20,000 S m^{-1}

7.4 Model validation

The grid independence study is conducted for the model validation work. Three non-uniformly distributed grid configurations with (I) 21×17×30, (II) 21×32×40, and (III) 41×42×40 elements in the x-, y- and z-directions are chosen and the pressure distribution along the first and second channels is evaluated. The influence of the number of elements is shown in Fig. 7.2 and the variation is 11.73% for grid (I) and (III), and 1.6% for grid (II) and (III). Thus, grid (II) is chosen as a tradeoff between the accuracy and the execution time of computation. In addition, the performance of the simulation code is evaluated by comparing the numerical result with the in-house experimental data. The major experimental conditions are as follows: flowrates of hydrogen and air are 1.67×10^{-5} m^3 s^{-1}, respectively and cell temperature is 70^{o}C. The comparison of the polarization curve is shown in Fig. 7.3 and the result agrees well. Fig. 7.4 shows the comparison of the experimental and numerically predicted cross-flowrates as a function of the inlet flowrate. The simulation result shows the good prediction of the cross-flowrate.

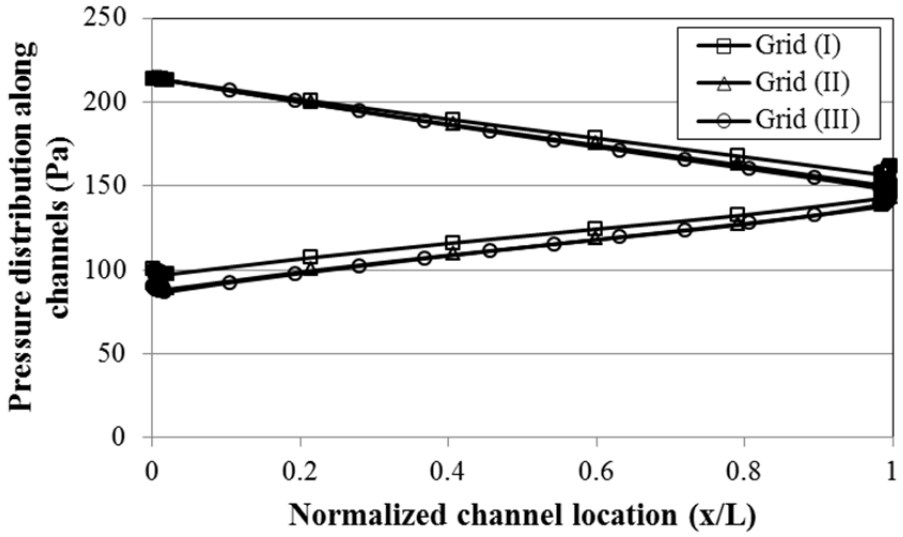

Fig. 7.2 The influence of the number of elements by the comparison of the pressure distribution (I) 21×17×30, (II) 21×32×40, and (III) 41×42×40

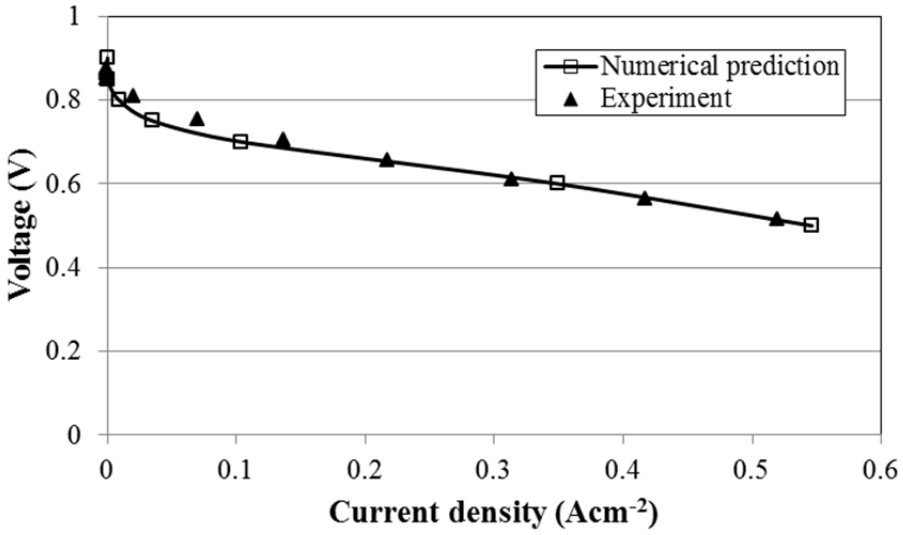

Fig. 7.3 Comparison of experimental and predicted polarization curves

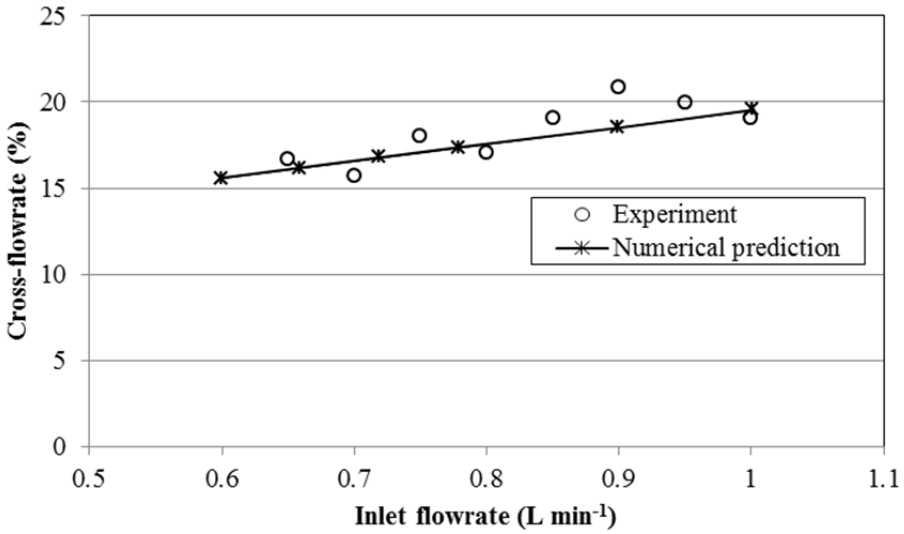

Fig. 7.4 Comparison of experimental and predicted cross-flowrates

CHAPTER 8

MODELING RESULTS OF FLOW FIELD, OXYGEN DISTRIBUTION AND CURRENT DENSITY

8.1 Overall flow field

Fig. 8.1(a) shows a flow field at the middle height of the channel. At the first U-bend region, a small recirculation flow is observed near the corner. In addition, there is a low velocity area near the land (region A) because of the shear force from the land surface. Fig. 8.1(b) presents a cross sectional view of the flow field at the first U-bend. The flow in the first channel collides against the wall of the U-bend and then, the flow direction is bent at 90 degrees. As a result, the upward and downward secondary flows are induced.

A cross sectional view of the flow distribution across the channel direction at the middle of the channel is given in Fig. 8.2(a). As can be seen in this figure, relatively large secondary flows occur at the second and third channels. These secondary flows are induced by the change of the flow direction at the two corners of the U-bend, i.e., 180 degrees turn. In addition, with the increase of the channel length (L) from 0.01 m to 0.06 m, the flow distribution varies as shown in Fig. 8.2(b). Since secondary flows observed at the case of L = 0.01 m are dissipated both at the second and third channels in this case, it can be said that the effect of the U-bend section on the flow distribution depends on the flow channel length.

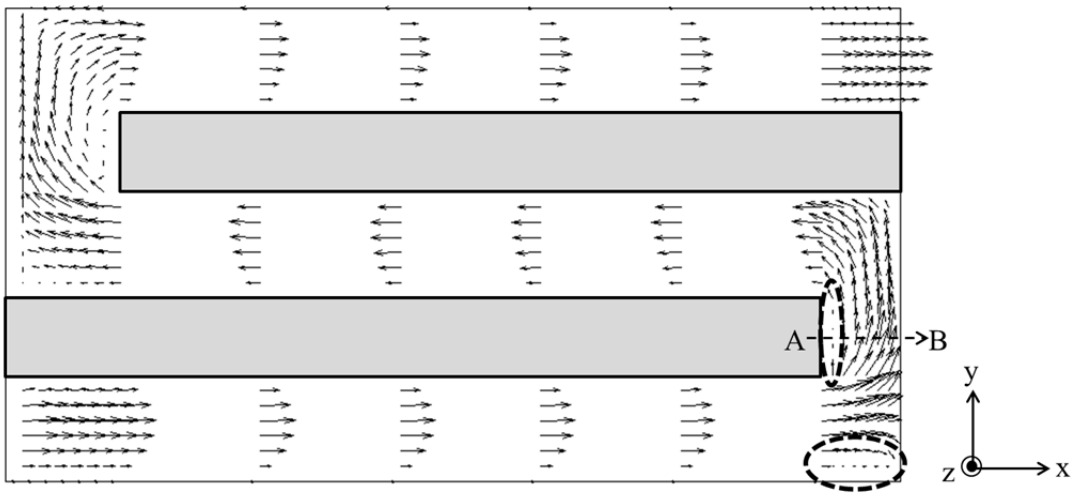

(a)

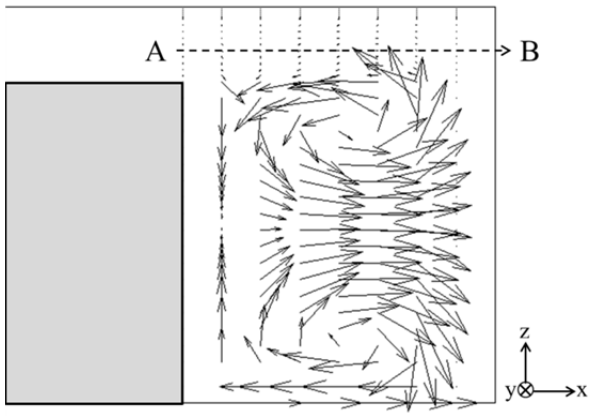

(b)

Fig. 8.1 Flow field (L=0.01 m) (a) along the channel direction (b) Cross sectional view at the first U-bend

Fig. 8.3 shows a magnified view of the flow field in the GDL under the first land at the case of L=0.06 m. Since the GDL is a porous medium and a pressure difference exists between adjacent channels in the serpentine flow field, a cross-flow occurs from the first channel to the second one. Although the catalyst layer, which is neighboring to the GDL, is also treated as a porous medium, the permeability of the catalyst layer is relatively small compared with the GDL and the flow motion is limited. As a result, the cross-flow inside the catalyst layer becomes very small.

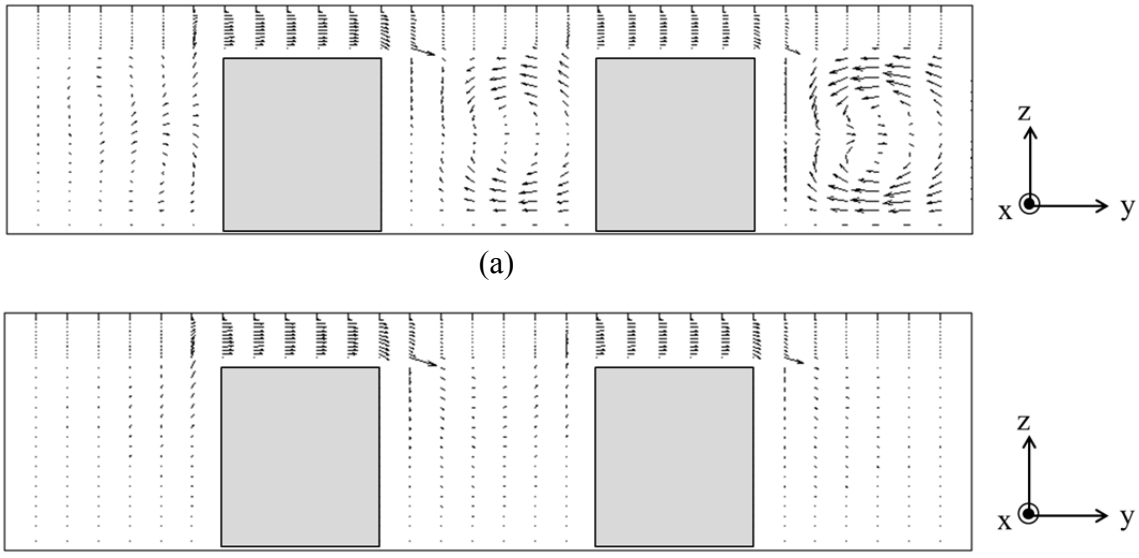

(a)

(b)

Fig. 8.2 Cross sectional flow distribution at the middle of channels

(a) L=0.01 m (b) L=0.06 m

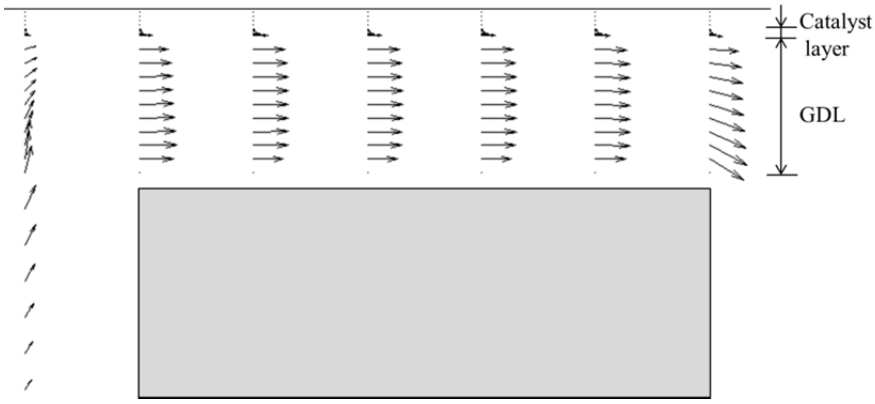

Fig. 8.3 Magnified view of cross-flow across the first land (L=0.06 m)

8.2 The under-land cross-flow

Fig. 8.4 shows the cross-flow in the GDL under the middle of the first land as a function of the normalized channel location. The cross-flow is chosen from different points in the GDL, i.e., near the land, near the catalyst layer and at the middle of the GDL

and normalized by the inlet flow velocity. The cross-flow at the middle of the GDL is the highest and the one near the land is the lowest due to the shear force from the land surface. In addition, the cross-flow near the inlet (x/L = 0) is the highest and it gradually decreases along the channel direction because the pressure difference between the first and second channels is gradually decreases along the channel as shown in Fig. 8.5 and the cross-flow is induced by this pressure difference.

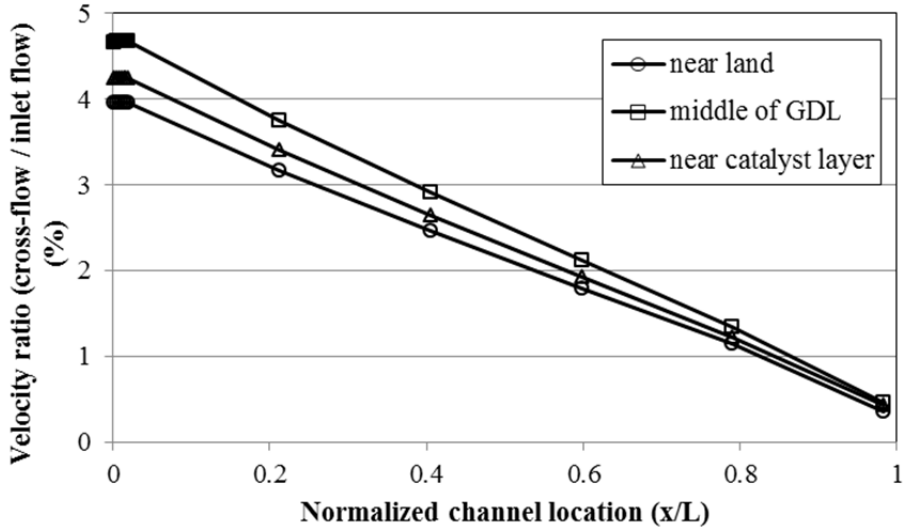

Fig. 8.4 Normalized cross-flow along the channel direction (L=0.06 m)

The normalized cross-flow distribution in the GDL across the channel direction is presented in Fig. 8.6. The horizontal axis indicates the direction across the channel and 1.0 of y/W corresponds to the interface between the first channel and the first land and 2.0 of y/W is the interface between the first land and the second channel. Although the cross-flow under the first channel is very small, it increases significantly under the first land and decreases again under the second channel area and this result obviously shows

that the cross-flow exists mainly under the land in the GDL. Furthermore, Fig. 8.6 indicates that the cross-flow is almost uniform under the land region and gradually decreases along the channel direction.

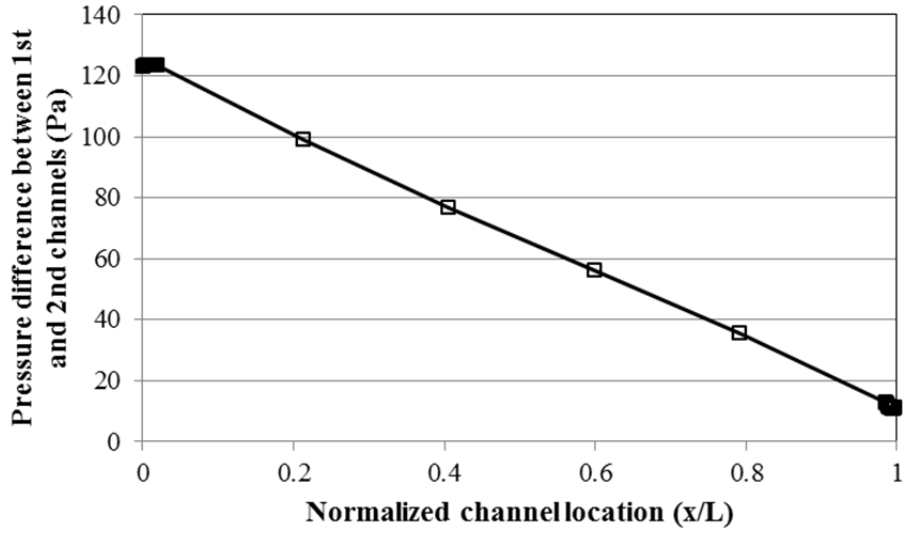

Fig. 8.5 Pressure difference between first and second channels (L=0.06 m)

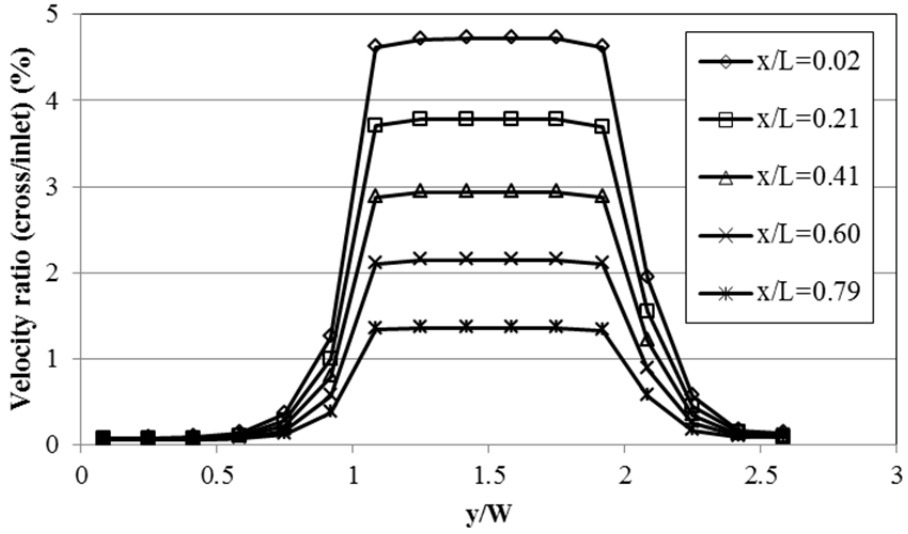

Fig. 8.6 Normalized cross-flow across the channel direction (L=0.06 m)

Fig. 8.7 presents the normalized cross-flow as a function of the normalized GDL location from near the land to near the catalyst layer. The distribution of the cross-flow is almost uniform in the GDL except near the land ($z/\delta = 0.0$) and near the catalyst layer ($z/\delta = 1.0$) where the shear force is induced by the land surface or the catalyst layer surface. This result also shows that the cross-flow gradually decreases along the channel direction due to the decrease of the pressure difference.

Fig. 8.8 shows the fraction of the cross-flow under the first land along the normalized channel direction. As seen in this result, the fraction of the cross-flow increases with the parabolic rule. In addition, although the total of the cross-flow reaches to 100% at the end of the land, almost a half of the cross-flow occurs by the first 30% region of the land due to the larger pressure difference.

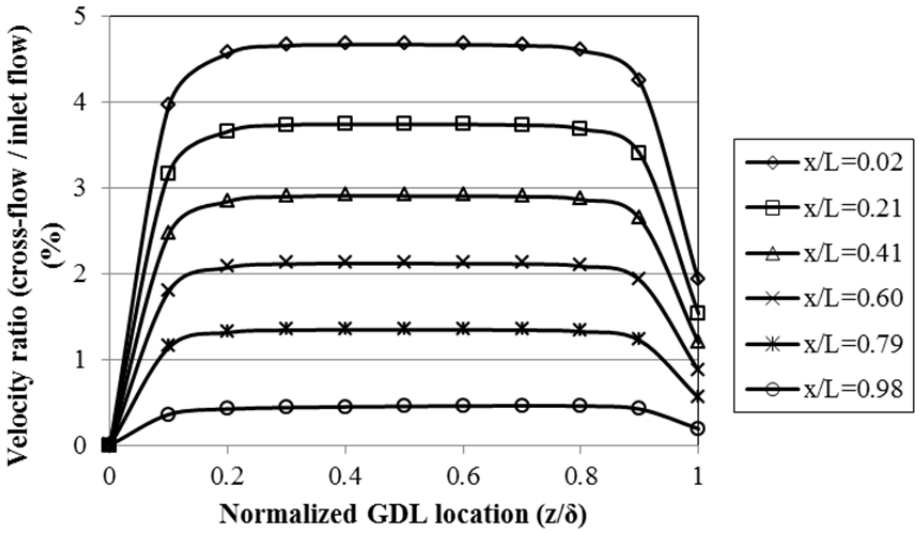

Fig. 8.7 Normalized cross-flow in the GDL (L=0.06 m)

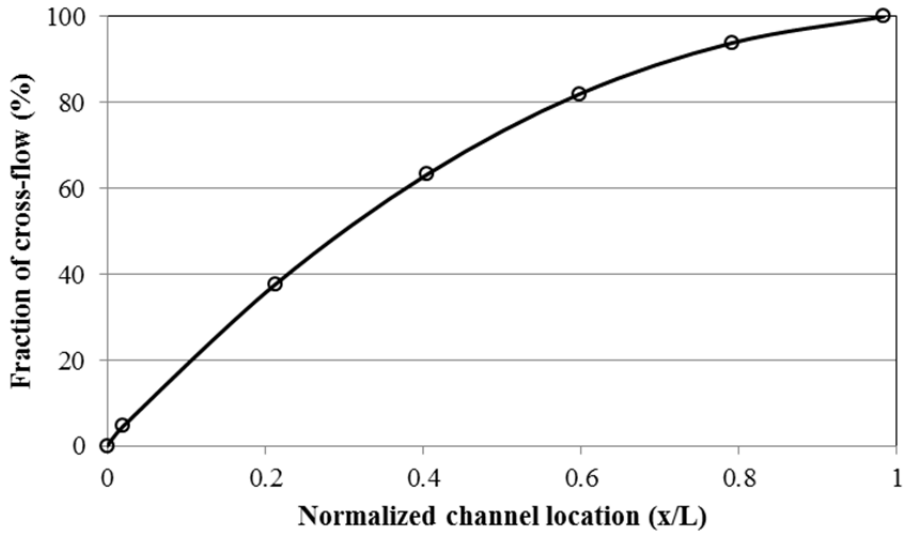

Fig. 8.8 Fraction of cross-flow under the first land (along the channel direction) (L=0.06 m)

8.3 Permeability and Reynolds number effects

Since the cross-flow is affected by the permeability of the GDL, the cross-flowrate (Park and Li 2007) should be evaluated in order to see the effect of the permeability on the cross-flow:

$$Q^{*}_{cross} = \frac{Q_{cross}}{Q_{in}} \times 100(\%) \tag{8.1}$$

where Q_{cross} is the flowrate of the cross-flow and Q_{in} is the inlet flowrate. The computed cross-florate is given in Fig. 8.9. It is clearly shown that the cross-flowrate increases with the increase of the permeability. However, once the permeability is larger than the order of 10^{-9} m^2, the cross-flowrate reaches to a certain value and the increment of the cross-flowrate becomes very small. This is because the pressure difference between the neighboring channels, which causes the cross-flow, becomes small with the increase of the permeability and the effects of the pressure difference and the permeability finally balance with each other. When the inlet velocity increases from Re = 148 to Re = 400,

the cross-flowrate also enhances although its increment is not so large. Moreover, as the channel length (L) extends from 0.01 m to 0.06 m at the same inlet Reynolds number, the cross-flowrate increases significantly with the increase of the permeability. This is because the cross-flow is caused by the pressure difference and the pressure difference increases significantly with the increase of the channel length. Some experimental studies measured the GDL permeability (Feser et al 2006, Gostick et al 2006, Ismail et al 2010b, Mathias et al 2003) and the typical permeability is within the range of the order of 10^{-13} to 10^{-11} m^2. Thus, it can be said that a few percent of the inlet flow becomes a cross-flow for the case of L = 0.01 m and around 10-20 percent of the inlet flow is expected to be a cross-flow at L = 0.06 m and Re=148.

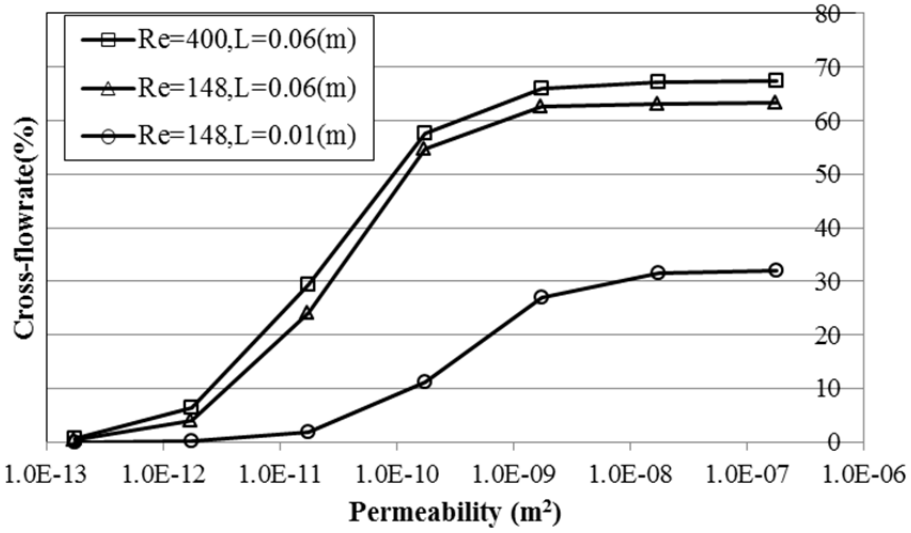

Fig. 8.9 Cross-flowrate with different GDL permeability

8.4 Oxygen mass fraction distribution

The oxygen mass fraction for the case of L = 0.01 m at the cell voltage of 0.5V is given in Fig. 8.10(a). As air moves in channels, its oxygen concentration gradually

decreases due to the consumption by the electrochemical reaction. Fig. 8.10(b) shows the cross sectional view of the oxygen distribution at the middle of channels (red oval in Fig. 8.10(a)). It is clearly shown that oxygen moves from the higher pressure side to the lower side through the GDL under the land by the cross-flow. In addition, the oxygen distribution at the second channel is different from the one at the first channel. In the second channel, two higher concentration regions are observed near the center of the channel. This distribution might be attributed to the secondary flow effect at the first U-bend. For the third channel, although secondary flows also exist, these effects are not so significant compared with the second channel and the oxygen distribution variation as seen at the second channel is not observed there. Fig. 8.11(a) shows the oxygen distribution for the case of L = 0.06 m at the cell voltage of 0.5V. With the electrochemical reaction, oxygen decreases along the channels as well as Fig. 8.10. At the third channel, the oxygen concentration becomes much lower compared with the case of L = 0.01 m due to the longer flow channel effect. The oxygen distribution across the middle of channels is given in Fig. 8.11(b). Oxygen moves from the higher pressure side to the lower pressure side through the GDL same as the previous case; however, the second channel does not have the oxygen distribution that is observed in the previous case because the secondary flow effect is dissipated for this longer channel case.

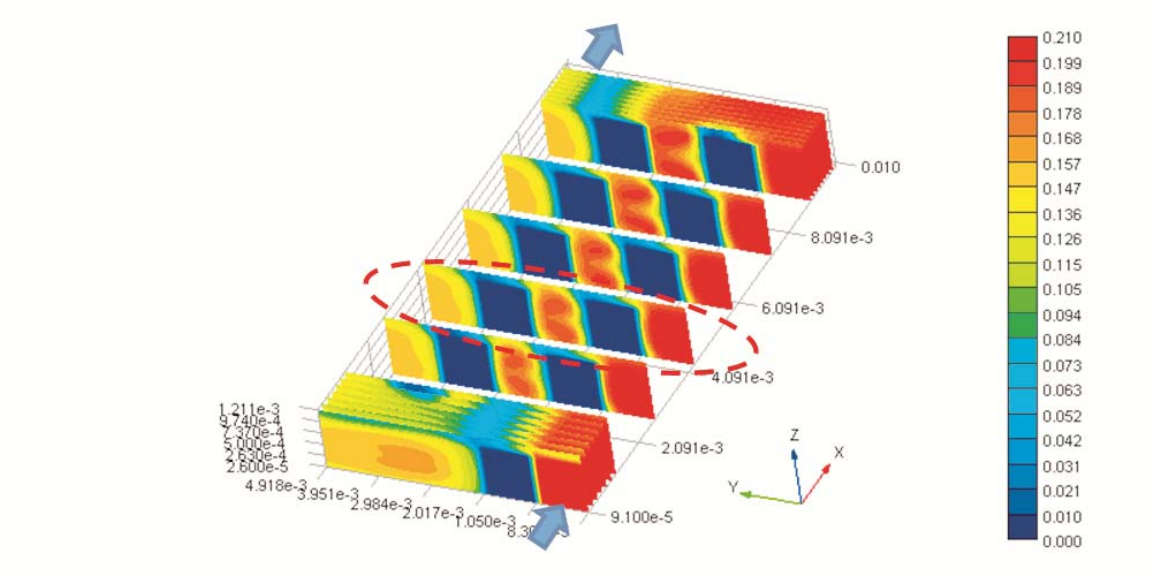

(a)

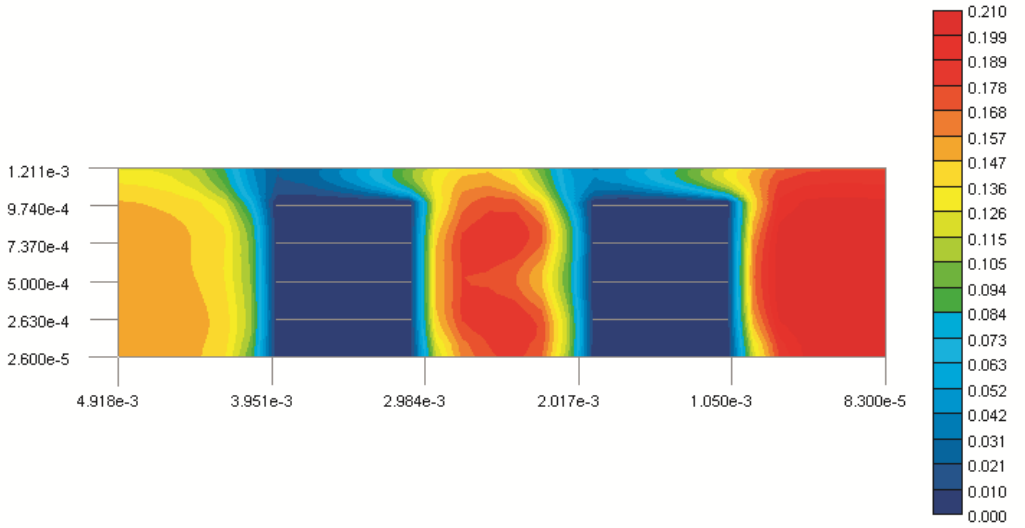

(b)

Fig. 8.10 Oxygen mass fraction at the cell voltage of 0.5V (L=0.01 m) (a) along the channel direction (b) across the channel direction (red oval in (a))

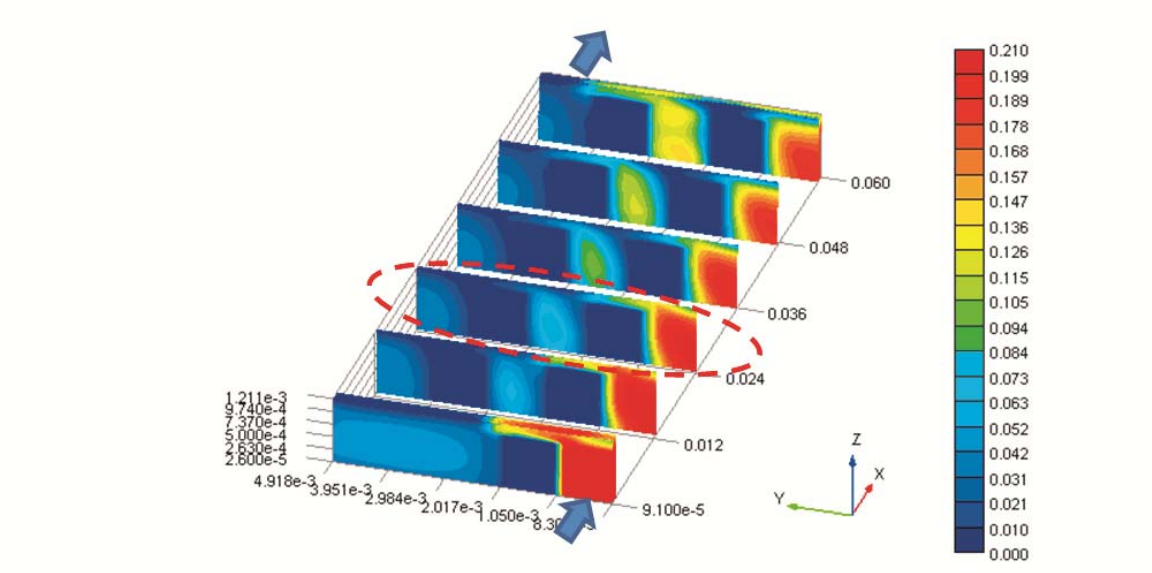

(a)

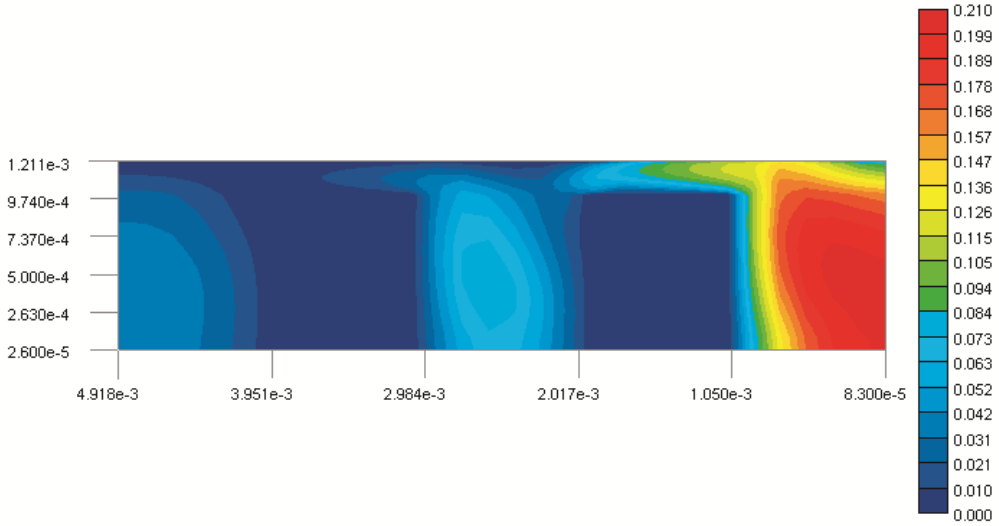

(b)

Fig. 8.11 Oxygen mass fraction at the cell voltage of 0.5V (L=0.06 m) (a) along the channel direction (b) across the channel direction (red oval in (a))

Fig. 8.12 presents the oxygen distribution along the channel direction in the GDL under the first land. The concentration at the middle of the GDL is the highest and the concentration near the land is the lowest. In addition, the concentration gradually decreases along the channel direction because the cross-flow is the highest at the middle

of the GDL and it gradually decreases along the channel. Fig. 8.13 shows the oxygen distribution across the channel direction in the GDL under the first land. The concentration near the first channel is the highest and the concentration near the second channel is the lowest because oxygen is transported from the first channel to the second channel directions by the cross-flow.

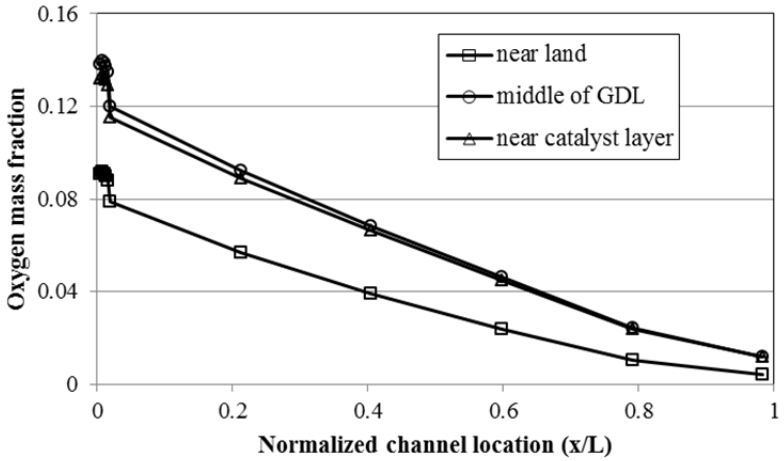

Fig. 8.12 Oxygen mass fraction along the channel direction in the GDL under the land (L=0.06 m)

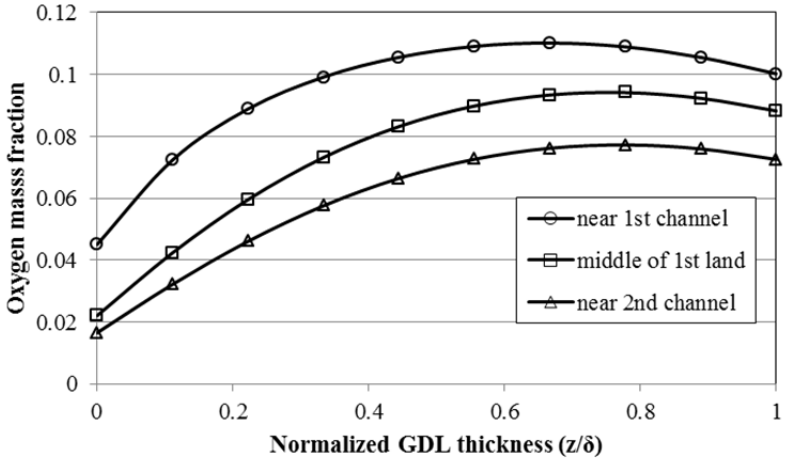

Fig. 8.13 Oxygen mass fraction across the channel direction in the GDL under the land (L=0.06 m)

8.5 Local current density

In order to evaluate the cross-flow effect on the fuel cell performance, areas of the first land, first and second channels are divided into several parts and the local current density at each area is investigated for the case of L = 0.06 m. As shown in Fig. 8.14, the first channel is divided into three parts (C1, C2, C3) and the second channel is also divided into three parts (C4, C5, C6). In addition, the first land is divided into three sections (L1, L2, L3).

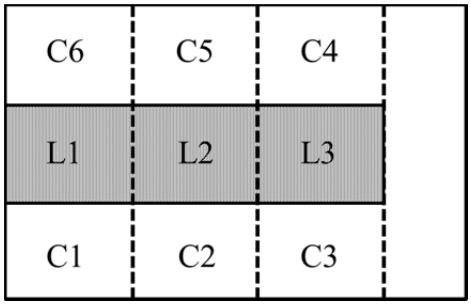

Fig. 8.14 Definition of divided areas of the first land, first and second channels

Fig. 8.15 shows the polarization curves at each area under the first and second channels. The local current density gradually decreases along the channel due to the oxygen consumption by the electrochemical reaction and the highest value is obtained at the channel inlet (C1) and the lowest one is gained at the end of the second channel (C6). For C5 and C6, the local current density decreases sharply at the low voltage compared with other cases since most of oxygen is already used in the upstream areas. In addition, the ratio of the maximum current density between C1 and C6 is more than four; thus, it can be said that the local current density distribution under the channel varies significantly along the channel direction.

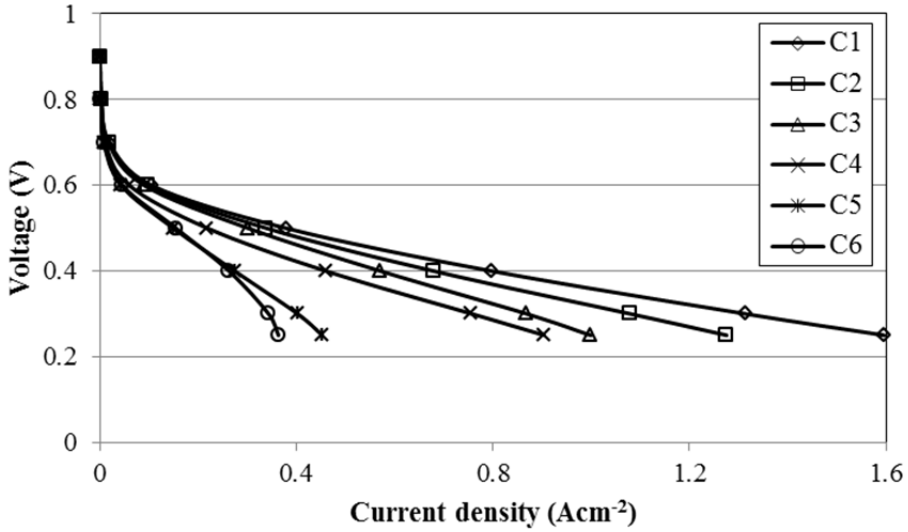

Fig. 8.15 Polarization curves at different channel locations

The local current density under the channels at different voltages is shown in Fig. 8.16. The local current density variation along the channel is small when the voltage is high because of the enough oxygen existence. However, as the voltage becomes low, the difference of the local current density among each area increases and C1 becomes the highest and C6 becomes the lowest and this trend is more obvious as the voltage becomes much smaller. For C4, the local current density at low voltages is a little higher than the expected values and this might be attributed to the secondary flow effect from the U-bend.

Fig. 8.17 presents the polarization curves at each area under the first land. The local current density near the inlet side (L1) is the highest and the one near the end of the land (L3) is the lowest since the oxygen under the land decreases along the channel direction as previously shown in Fig. 8.12.

The local current density under the land is shown in Fig. 8.18. Although the difference of the local current density is small among L1, L2 and L3 at high voltages, as

the voltage decreases, the difference increases significantly between the upstream and the downstream because oxygen distribution under the land is considerably affected by the cross-flow and L1 has the larger cross-flow effect than L3.

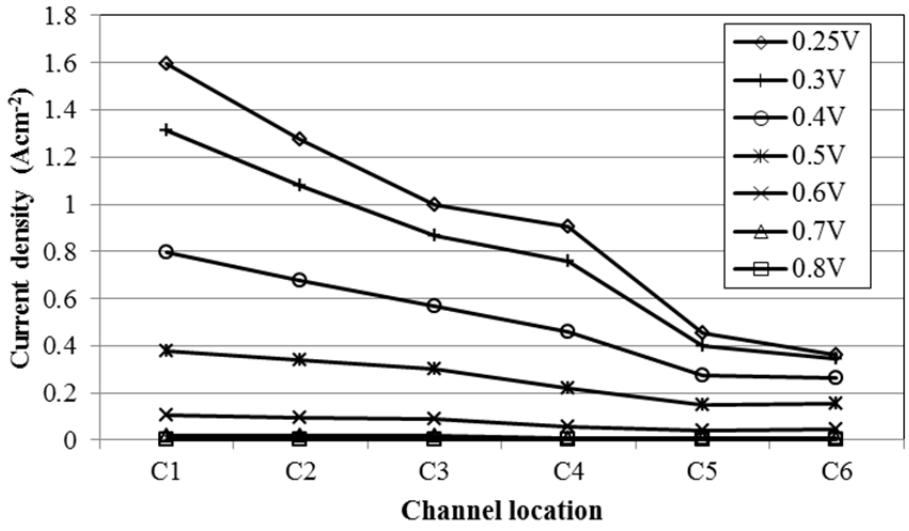

Fig. 8.16 Local current density at different voltages

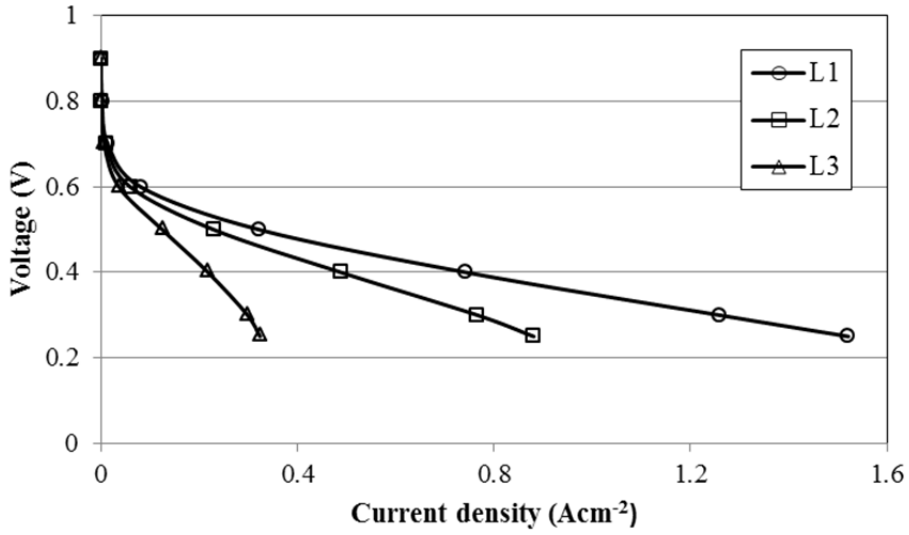

Fig. 8.17 Polarization curves at different land locations

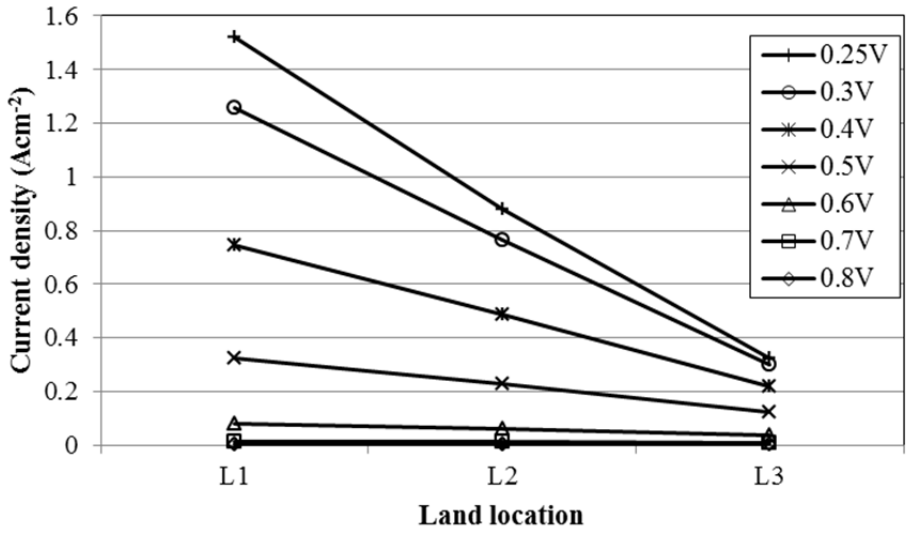

Fig. 8.18 Local current density under the land

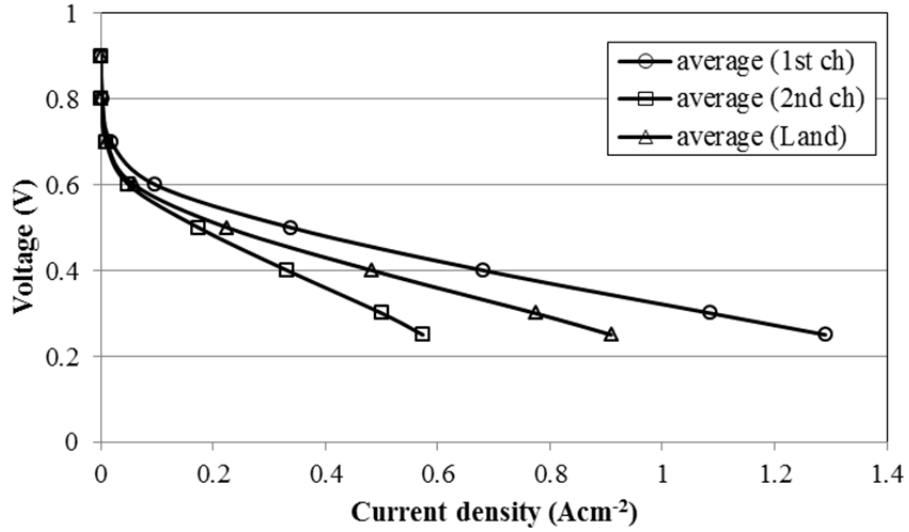

Fig. 8.19 Average polarization curves under the channels and the first land

Fig. 8.19 shows the average polarization curves among under the land, the first and second channels. The current density under the first channel is the highest and the current density under the second channel is the lowest. The current density under the first land is

between them; thus, it can be said that the cell performance gradually decreases across the channel direction due to the cross-flow effect.

8.6 Summary

A three-dimensional PEM fuel cell model is developed and the flow field, the oxygen distribution and the local current density distribution around the land are investigated.

The modeling result shows that the cross-flow gradually decreases along the channel direction. The result across the channel direction also indicates that the cross-flow exists mainly under the land. The cross-flow distribution along the channel direction is investigated and it is shown that almost a half of the cross-flow occurs by the first 30% region of the land due to the larger pressure difference. The effect of the cross-flow on the oxygen distribution is studied and it is shown that the oxygen concentration in the channel is affected by the secondary flow which is induced by the U-bend if the channel length is short.

The local current density around the land is investigated and it is revealed that the cross-flow has a significant effect on the local current density distribution under the land area. It is also shown that the current density under the land area decreases along the channel and the difference between the upstream and the downstream increases with the increase of the cell voltage.

CHAPTER 9

CONCLUSION AND SUGGESTIONS FOR FURTHER RESEARCH

9.1 Conclusion

In this work, experimental and modeling studies are conducted in order to investigate the under-land cross-flow in a PEM fuel cell.

In the experimental study, a unique experimental fixture is developed for *in situ* measurement of the effective permeability of the GDL and the under-land cross-flow in an actual fuel cell. The cross-flow is measured with varying the valve closure and then, the cross-flowrate is obtained as a function of the pressure difference at different operational conditions. In addition, the cross-flowrate is expressed as a function of two dimensionless parameters by dimensional analysis. Finally, the current density and the net power density are investigated in order to evaluate the effects of the pressure difference and the pumping power on the fuel cell performance.

Based on these experimental works, following conclusions are obtained.

- The effective permeability varies with the land width due to the inertial effect inside the GDL. The non-Darcy effect increases with the decrease of the land width and with the increase of mass flux.
- The cross-flowrate increases with the increase of the pressure difference between the adjacent channels. The non-dimensional correlation for the cross-flowrate agrees well with experimental data for different operational conditions and different inlet flowrates.

- The current density increases with the increase of the valve closure and this performance enhancement is attributed to the effect of the cross-flow. In addition, small increases of the pressure difference are more efficient than large pressure increments.
- The net power density ratio shows that the fuel cell performance increases efficiently from the zero to low closure conditions. Furthermore, the cross-flow increases the fuel cell performance with the additional small increment of the pressure difference and the excessive stoichiometry decreases the fuel cell efficiency.

For the modeling study, a three-dimensional PEM fuel cell model is developed and the flow field, the oxygen distribution and the local current density distribution around the land area are investigated.

Based on these modeling works, following conclusions are acquired.

- The cross-flow gradually decreases along the channel direction and it exists mainly under the land area.
- The oxygen concentration in the channel is affected by the secondary flow which is induced by the U-bend if the channel length is short.
- The cross-flow has a significant effect on the local current density distribution under the land area and the current density under the land area decreases along the channel and the difference between the upstream and downstream increases with the decrease of the cell voltage.

The present work has shown a method for the in situ measurement of the effective permeability, the under-land cross-flow and the cross-flow effect on the fuel cell performance in an actual fuel cell. Based on these attainments, an optimal flow field design should have an additional small pressure difference between the adjacent channels and the moderate value of stoichiometry in order not to increase the pumping power.

9.2 Suggestion for further research

Possible suggestions for the further research include:

- Implementation of two-phase flow model to the current simulation code is preferable in order for the better understanding of the mass transport in the fuel cell.
- Measurement of the current density both under the land and the channel separately in order to determine the cross-flow effect on these areas.
- Measurement of the current density under the land by breaking down the land MEA into several areas in order to investigate the current density variation under the land area with the effect of the cross-flow.
- Measurement of the effective permeability, the cross-flowrate and the current density with controlling the assembling torque by the method which was previously proposed by Ge et al. (Ge et al 2006), since the cell assembling torque affects the fuel cell performance.

- Design of optimized flow fields which effectively use the cross-flow effect by locally changing the channel width in order to enhance the pressure difference between the neighboring channels, e.g. Fig. 9.1.
- Design of optimized flow fields which effectively use the cross-flow effect with the moderate value of stoichiometry, e.g. Fig. 9.2

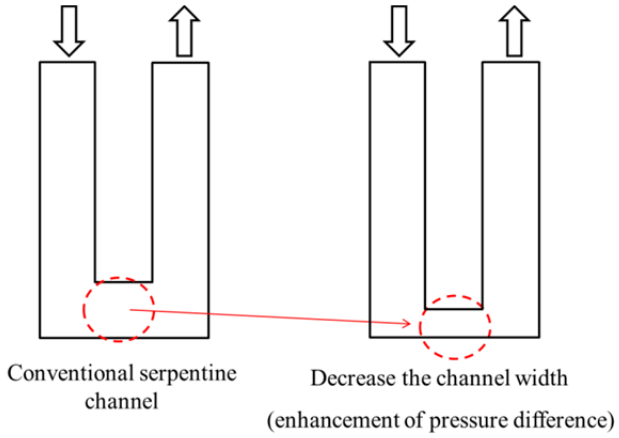

Fig. 9.1 Serpentine flow field design with the enhanced pressure difference

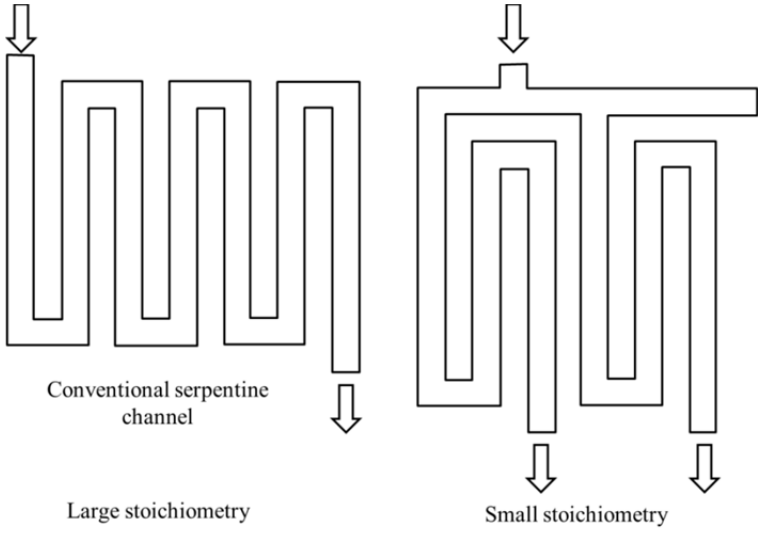

Fig. 9.2 Serpentine flow field design with moderate stoichiometry

REFERENCES

Amphlett JC, Baumert RM, Mann RF, Peppley BA, Roberge PR, Harris TJ (1995). Performance modeling of the Ballard-Mark-IV solid polymer electrolyte fuel cell 1. Mechanistic model development. *J. Electrochem. Soc.* **142:** 1-8.

Bachman J, Santamaria A, Tang H-Y, Park JW (2012). Investigation of polymer electrolyte membrane fuel cell parallel flow field with induced cross flow. *J. Power Sources* **198:** 143-148.

Barbir F, Gorgun H, Wang X (2005). Relationship between pressure drop and cell resistance as a diagnostic tool for PEM fuel cells. *J. Power Sources* **141:** 96-101.

Bernardi DM, Verbrugge MW (1991). Mathematical model of a gas diffusion electrode bonded to a polymer electrolyte. *AIChE J.* **37:** 1151-1163.

Bernardi DM, Verbrugge MW (1992). A mathematical model of the solid-polymer-electrolyte fuel cell. *J. Electrochem. Soc.* **139:** 2477-2491.

Birgersson E, Noponen M, Vynnycky M (2005). Analysis of a two-phase non-isothermal model for a PEFC. *J. Electrochem. Soc.* **152:** A1021-1034.

Choi K-S, Kim H-M, Moon S-M (2011). An experimental study on the enhancement of the water balance, electrochemical reaction and power density of the polymer electrolyte fuel cell by under-rib convection. *Electrochem. Commun.* **13:** 1387-1390.

Dagan G (1979). The generalization of darcy's law for nonuniform flows. *Water Resour. Res.* **15:** 1-7.

Dohle H, Jung R, Kimiaie N, Mergel J, Müller M (2003). Interaction between the diffusion layer and the flow field of polymer electrolyte fuel cells—experiments and simulation studies. *J. Power Sources* **124:** 371-384.

Dutta S, Shimpalee S, Van Zee JW (2001). Numerical prediction of mass-exchange between cathode and anode channels in a PEM fuel cell. *Int. J. Heat Mass Trans.* **44:** 2029-2042.

Feser JP, Prasad AK, Advani SG (2006). Experimental characterization of in-plane permeability of gas diffusion layers. *J. Power Sources* **162:** 1226-1231.

Fuller TF, Newman J (1993). Water and thermal management in solid-polymer-electrolyte fuel cells. *J. Electrochem. Soc.* **140:** 1218-1225.

Ge J, Higier A, Liu H (2006). Effect of gas diffusion layer compression on PEM fuel cell performance. *J. Power Sources* **159:** 922-927.

Gostick J (2009). Multiphase mass transfer and capillary properties of gas diffusion layers for polymer electrolyte membrane fuel cells. Ph.D dissertation thesis, University of Waterloo.

Gostick JT, Fowler MW, Pritzker MD, Ioannidis MA, Behra LM (2006). In-plane and through-plane gas permeability of carbon fiber electrode backing layers. *J. Power Sources* **162:** 228-238.

Gurau V, Liu H, Kakac S (1998). Two-dimensional model for proton exchange membrane fuel cells. *AIChE J.* **44:** 2410-2422.

Gurau V, Bluemle MJ, De Castro ES, Tsou Y-M, Zawodzinski TAJ, Mann JAJ (2007). Characterization of transport properties in gas diffusion layers for proton exchange membrane fuel cells. *J. Power Sources* **165:** 793-802.

He W, Lin G, Nguyen TV (2003). Diagnostic tool to detect electrode flooding in proton-exchange-membrane fuel cells. *AIChE J.* **49:** 3221-3228.

Higier A, Liu H (2009). Direct measurement of current density under the land and channel in a PEM fuel cell with serpentine flow fields. *J. Power Sources* **193:** 639-648.

Higier A, Liu H (2010). Optimization of PEM fuel cell flow field via local current density measurement. *Int. J. Hydrogen Energ.* **35:** 2144-2150.

Hu G, Fan J (2007). Transient computation fluid dynamics modeling of a single proton exchange membrane fuel cell with serpentine channel. *J. Power Sources* **165:** 171-184.

Huang W, Zhou B, Sobiesiak A (2005). Along-channel mathematical modelling for proton exchange membrane fuel cells. *Int. J. Energ. Res.* **29:** 1051-1071.

Hussaini IS, Wang CY (2010). Measurement of relative permeability of fuel cell diffusion media. *J. Power Sources* **195:** 3830-3840.

Ismail MS, Damjanovic T, Hughes K, Ingham DB, Ma L, Pourkashanian M *et al* (2010a). Through-plane permeability for untreated and PTFE-treated gas diffusion layers in proton exchange membrane fuel cells. *J. Fuel Cell Sci. Technol.* **7:** 051016.

Ismail MS, Damjanovic T, Ingham DB, Ma L, Pourkashanian M (2010b). Effect of polytetrafluoroethylene-treatment and microporous layer-coating on the in-plane permeability of gas diffusion layers used in proton exchange membrane fuel cells. *J. Power Sources* **195:** 6619-6628.

Jiao K, Park J, Li X (2010). Experimental investigations on liquid water removal from the gas diffusion layer by reactant flow in a PEM fuel cell. *Appl. Energ.* **87:** 2770-2777.

Kandlikar SG, Lu Z, Domigan WE, White AD, Benedict MW (2009). Measurement of flow maldistribution in parallel channels and its application to ex-situ and in-situ experiments in PEMFC water management studies. *Int. J. Heat Mass Trans.* **52:** 1741-1752.

Kanezaki T, Li X, Baschuk JJ (2006). Cross-leakage flow between adjacent flow channels in PEM fuel cells. *J. Power Sources* **162:** 415-425.

Kazim A, Forges P, Liu H (2003). Effects of cathode operating conditions on performance of a PEM fuel cell with interdigitated flow fields. *Int. J. Energ. Res.* **27:** 401-414.

Kim J, Lee SM, Srinivasan S, Chamberlain CE (1995). Modeling of proton exchange fuel cell performance with an empirical equation. *J Electrochem Soc* **142:** 2670-2674.

Larminie J, Dicks A (2003). *Fuel cell systems explained*. John Wiley & Sons: NJ.

Lee JH, Lalk TR, Appleby AJ (1998). Modeling electrochemical performance in large scale proton exchange membrane fuel cell stacks. *J. Power Sources* **70:** 258-268.

Lin G, Nguyen TV (2006). A two-dimensional two-phase model of a PEM fuel cell. *J. Electrochem. Soc.* **153:** A372-382.

Liu X, Guo H, Ye F, Ma C (2007). Water flooding and pressure drop characteristics in flow channels of proton exchange membrane fuel cells. *Electrochim. Acta* **52:** 3607-3614.

Lu Z, Kandlikar SG, Rath C, Grimm M, Domigan W, White AD *et al* (2009). Water management studies in PEM fuel cells, Part II: Ex situ investigation of flow maldistribution, pressure drop and two-phase flow pattern in gas channels. *Int. J. Hydrogen Energ.* **34:** 3445-3456.

Ma H, Ruth DW (1993). The microscopic analysis of high Forchheimer number flow in porous media. *Transport Porous Med.* **13:** 139-160.

Ma HP, Zhang HM, Hu J, Cai YH, Yi BL (2006). Diagnostic tool to detect liquid water removal in the cathode channels of proton exchange membrane fuel cells. *J. Power Sources* **162:** 469-473.

Mann RF, Amphlett JC, Hooper MAI, Jensen HM, Peppley BA, Roberge PR (2000). Development and application of a generalized electrochemical model for a PEM fuel cell. *J. Power Sources* **86:** 173-180.

Mathias M, Roth J, Fleming J, Lehnert W (2003). *Diffusion media materials and characterization*, vol. 3. John Wiley & Sons: New York.

Munson BR, Young DF, Okiishi TH, Huebsch WW (2009). *Fundamentals of fluid mechanics*. John Wiley & Sons, Inc.: New Jersey.

Natarajan D, Nguyen VT (2001). A two-dimensional, two-phase, multicomponent, transient model for the cathode of a proton exchange membrane fuel cell using conventional gas distributors. *J. Electrochem. Soc.* **148:** A1324-1335.

Nguyen PT, Berning T, Djilali N (2004). Computational model of a PEM fuel cell with serpentine gas flow channels. *J. Power Sources* **130:** 149-157.

Nguyen TV, White RE (1993). A water and heat management model for proton-exchange-membrane fuel-cells. *J. Electrochem. Soc.* **140:** 2178-2186.

O'Hayre R, Cha S-W, Colella W, Prinz FB (2009). *Fuel cell fundamentals*, Second edn. John Wiley & Sons: New York.

Oosthuizen P, Sun L, McAuley K (2005). The effect of channel-to-channel gas crossover on the pressure and temperature distribution in PEM fuel cell flow plates. *Appl. Therm. Eng.* **25:** 1083-1096.

Park J, Li X (2007). An experimental and numerical investigation on the cross flow through gas diffusion layer in a PEM fuel cell with a serpentine flow channel. *J. Power Sources* **163:** 853-863.

Park JW, Jiao K, Li X (2010). Numerical investigations on liquid water removal from the porous gas diffusion layer by reactant flow. *Appl. Energ.* **87:** 2180-2186.

Passalacqua E, Lufrano F, Squadrito G, Patti A, Giorgi L (2001). Nafion content in the catalyst layer of polymer electrolyte fuel cells: Effects on structure and performance. *Electrochim. Acta* **46:** 799-805.

Patankar SV (1980). *Numerical heat transfer and fluid flow*. MacGraw-hill: New York.

Pharoah JG (2005). On the permeability of gas diffusion media used in PEM fuel cells. *J. Power Sources* **144:** 77-82.

Pourmahmoud N, Rezazadeh S, Mirzaee I, Heidarpoor V (2011). Three-dimensional numerical analysis of proton exchange membrane fuel cell. *J. Mech. Sci. Technol.* **25:** 2665-2673.

Prasad KBS, Jayanti S (2008). Effect of channel-to-channel cross-flow on local flooding in serpentine flow-fields. *J. Power Sources* **180:** 227-231.

Ruth D, Ma H (1992). On the derivation of the Forchheimer equation by means of the averaging theorem. *Transport Porous Med.* **7:** 255-264.

Shi Z, Wang X (2008). A numerical study of flow crossover between adjacent flow channels in a proton exchange membrane fuel cell with serpentine flow field. *J. Power Sources* **185:** 985-992.

Spernjak D, Prasad AK, Advani SG (2007). Experimental investigation of liquid water formation and transport in a transparent single-serpentine PEM fuel cell. *J. Power Sources* **170:** 334-344.

Spiegel C (2007). *Designing and building fuel cells*. McGraw-Hill: New York.

Springer TE, Zawodzinski TA, Gottesfeld S (1991). Polymer electrolyte fuel cell model. *J. Electrochem. Soc.* **138:** 2334-2342.

Springer TE, Wilson MS, Gottesfeld S (1993). Modeling and experimental diagnostics in polymer electrolyte fuel cells. *J. Electrochem. Soc.* **140:** 3513-3526.

Squadrito G, Maggio G, Passalacqua E, Lufrano F, Patti A (1999). An empirical equation for polymer electrolyte fuel cell behaviour. *J. Appl. Electrochem.* **29:** 1449-1455.

Sun L, Oosthuizen P, McAuley K (2006). A numerical study of channel-to-channel flow cross-over through the gas diffusion layer in a PEM-fuel-cell flow system using a serpentine channel with a trapezoidal cross-sectional shape. *Int. J. Therm. Sci.* **45:** 1021-1026.

Sun W, Peppley BA, Karan K (2005). Modeling the influence of GDL and flow-field plate parameters on the reaction distribution in the PEMFC cathode catalyst layer. *J. Power Sources* **144:** 42-53.

Tehlar D, Flückiger R, Wokaun A, Büchi FN (2010). Investigation of channel-to-channel cross convection in serpentine flow fields. *Fuel Cells* **10:** 1040-1049.

U.S. Department of Energy (2011). 2011 annual progress report, DOE hydrogen and fuel cells program.

U.S. Energy Information Administration (2011). Annual energy outlook 2011: Washington D.C.

U.S. Energy Information Administration (2012). Annual energy outlook 2012 early release overview: Washington D.C.

Um S, Wang CY, Chen KS (2000). Computational fluid mechanics of proton exchange membrane fuel cells. *J. Electrochem. Soc.* **147:** 4485-4493.

Um S, Wang CY (2004). Three-dimensional analysis of transport and electrochemical reactions in polymer electrolyte fuel cells. *J. Power Sources* **125:** 40-51.

Wang L, Liu H (2008). Separate measurement of current density under the channel and the shoulder in PEM fuel cells. *J. Power Sources* **180:** 365-372.

Wang X-D, Duan Y-Y, Yan W-M, Lee D-J, Su A, Chi P-H (2009). Channel aspect ratio effect for serpentine proton exchange membrane fuel cell: Role of sub-rib convection. *J. Power Sources* **193:** 684-690.

Wang X-D, Zhang X-X, Liu T, Duan Y-Y, Yan W-M, Lee D-J (2010). Channel geometry effect for proton exchange membrane fuel cell with serpentine flow field using a three-dimensional two-phase model. *J. Fuel Cell Sci. Technol.* **7:** 051019.

Wang Y, Wang C-Y (2006). A nonisothermal, two-phase model for polymer electrolyte fuel cells. *J. Electrochem. Soc.* **153:** A1193-1200.

Williams MV, Begg E, Bonville L, Kunz HR, Fenton JM (2004a). Characterization of gas diffusion layers for PEMFC. *J. Electrochem. Soc.* **151:** A1173-1180.

Williams MV, Kunz HR, Fenton JM (2004b). Influence of convection through gas-diffusion layers on limiting current in PEM FCs using a serpentine flow field. *J. Electrochem. Soc.* **151:** A1617-1627.

Yi JS, Nguyen TV (1998). An along the channel model for proton exchange membrane fuel cells. *J. Electrochem. Soc.* **145:** 1149-1159.

Yi JS, Yang JD, King C (2004). Water management along the flow channels of PEM fuel cells. *AIChE J.* **50:** 2594-2603.

Zeng Z, Grigg R (2006). A criterion for non-Darcy flow in porous media. *Transport Porous Med.* **63:** 57-69.

Zhang L, Bi HT, Wilkinson DP, Stumper J, Wang H (2010). Gas flow rate distributions in parallel minichannels for polymer electrolyte membrane fuel cells: Experiments and theoretical analysis. *J. Power Sources* **195:** 3231-3239.

Zhou T, Liu H (2001). A general three-dimensional model for proton exchange membrane fuel cells. *Int. J. Transport Phenom.* **3:** 177-198.

Zhou T, Liu H (2006). Effects of the electrical resistances of the GDL in a PEM fuel cell. *J. Power Sources* **161:** 444-453.